Near-Field Optical Forces: Photonics, Plasmonics and the Casimir Effect

Dissertation Advisor: Federico Capasso David Nathaniel Woolf

Near-Field Optical Forces: Photonics, Plasmonics and the Casimir Effect

Abstract

The coupling of macroscopic objects via the optical near-field can generate strong attractive and repulsive forces. Here, I explore the static and dynamic optomechanical interactions that take place in a geometry consisting of a silicon nanomembrane patterned with a square-lattice photonic crystal suspended above a silicon-on-insulator substrate. This geometry supports a hybridized optical mode formed by the coupling of eigenmodes of the membrane and the silicon substrate layer. This system is capable of generating nanometer-scale deflections at low optical powers for membrane-substrate gaps of less than 200 nm due to the presence of an optical cavity created by the photonic crystal that enhances both the optical force and a force that arises from photo-thermal-mechanical properties of the system. Feedback between Brownian motion of the membrane and the optical and photo-thermal forces lead to dynamic interactions that perturb the mechanical frequency and linewidth in a process known as "back-action." The static and dynamic properties of this system are responsible for optical bistability, mechanical cooling and regenerative oscillations under different initial conditions. Furthermore, solid objects separated by a small distance experience the Casimir force, which

results from quantum fluctuations of the electromagnetic field (i.e. virtual photons).The Casimir force supplies a strong nonlinear perturbation to membrane motion when the membrane-substrate separation is less than 150 nm. Taken together, the unique properties of this system makes it an intriguing candidate for transduction, accelerometry, and sensing applications.

Second, near field optical forces were explored in two geometries involving surface plasmons. The first looked at the forces generated between two plasmonic waveguides at visible frequencies where flat metallic surfaces support tightly confined interface waves and at mid-infrared frequencies, where surface corrugations allow the propagation of surface waves known as "spoof" surface plasmons. The second involves the generation of a repulsive force on a low refractive index particle in a high refractive index fluid above a metal surface. This second geometry opens up a potential new avenue for frictionless waveguiding and the study of chemical and biological binding processes where it is desirable to have surfaces in the proximity of one another but not in contact.

Contents

List of Figures

Acknowledgements

I would like to thank all friends, family, acquaintances, mentors, mentees, collaborators, books, films, records, cups of tea, couches and beds that helped me through the past seven and a half years. Namely, I'd like to start by sending thanks to three professors from my undergraduate university: my research advisor, Atul Parikh, who gave me my first taste in an optics lab, James Shackelford, who put me in front of students who supposedly knew less than I, and Richard Freeman who first hooked me on optics and encouraged me to be involved in my program and my community. To George Stimson, my high school physics teacher, who taught me how to always be curious.

To the Capasso group members – Jeremy, Jenny and Jon among them – who welcomed me into the group and taught me everything I needed to know about plasmonics, with particular thanks to Jeremy for his mentorship and his help in how to balance being in a band and doing research at the same time. To the current members of the Capasso group, particularly Mikhail and Romain, for always being around and always having the answers. To the students who allowed me to advise them: Hamsa, Sarah and Tomas, from whom I likely learned more than they learned from me. To the members of the Loncar group, who accepted me into their already crowded lab. To Wallace, in particular, with whom I have worked closely for the past three years and whose collaboration has taught me so much. To Alejandro, for our many and constant discussions and for never letting me by when my understanding fell short. To everyone at CNS and NNIN who trusted me to work on their machines. To Chris for her endless patience and skill in bureaucratic navigation. To my committee members: Ken Crozier, Joost Vlassak and Bob Westervelt. To Alexey Belyanin and Steven Johnson for many many helpful discussions on the theory of optical and Casimir forces. To Marko Loncar for all of the

encouragement, mentorship, and friendship he as given me, without which this all would have been nearly impossible. And to Federico Capasso, who has fostered my growth for the past six and a half years, cultivating my skills as an investigator and scientist, and allowing me to flourish in his dynamic research group.

To Eric, Ruwan, Nick and the rest of the Jeopardy crew for the past six years of email trivia and for continuing to trash talk the Harvard guy for never being able to hold a lead in December. To Will, Ryan, Dave, Adam, Rob and Erin for getting me through the earlier years and for always being around for a drink when necessary. To Chris, Shannon, Zack, Andy, Eerik, Brian and Emily. And especially to Jeanette and Carolyn, for epic hangs.

To my parents and grandparents and sisters for their constant love and support. And to Alyssa, for keeping me grounded, for keeping me sane, and for keeping me.

For my dad, the physicist and the father.

And for Alyssa, my favorite.

"A poet once said, "The whole universe is in a glass of wine." We will probably never know in what sense he meant that, for poets do not write to be understood. But it is true that if we look at a glass of wine closely enough we see the entire universe."

Richard Feynman

"...there ain't no journey what don't change you some."

David Mitchell, *Cloud Atlas*

Chapter 1

Introduction

1.1 Near Field Optical Forces

1.1.1 Overview

The work presented in this thesis covers experiments and theory tied together by the involvement of near-field photonic forces and their importance in the growing field of nanoscale optomechanical systems. In this chapter, I will first provide an introduction to the concept of optical forces, followed by an overview of the projects in which I was involved. These projects can be divided into three major areas: silicon optomechanics, surface plasmon waveguide forces, and the Casimir effect.

1.1.2 A Historical Perspective of Optical Forces

Researchers have long held interest in converting electromagnetic energy into mechanical motion. Kepler was the first to hypothesize that solar radiation is responsible for the deflection of comet tails away from the sun. By 1903, Lebedew [1] and Nichols and

Hull [2] had proved Maxwell's hypothesis that light impinging on a thin metallic disk in a vacuum would induce measurable motion. Over the course of the next century, applications for harnessing the energy of light were seen in systems ranging from the "Solar Sail" [3] to optical traps and tweezers [4, 5]. In the last decade, the interest in near field optical interactions increased, as on-chip optical circuitry has presented viable alternatives to slower electronic systems[6].

The initial single-beam trapping experiment by Ashkin et al. [4] was the the first to demonstrate the power of the optical field gradient on macroscopic objects. In the experiment, Ashkin demonstrated that a tightly focused laser beam could trap a spherical dielectric particle in both normal and tangential directions. This concept is illustrated using ray optics in Figure 1.1 and 1.2, where a lens is placed along the z-axis just above the graphic such that it is able to tightly focus a collimated laser beam a short distance beneath it. The width of the beam is represented by rays 1 and 2 and the point where the rays intersect represents the focal point of the beam. If we place a dielectric particle (with refractive index higher n_p than that of the surrounding medium n_0) near the beam's focus, we can use the trace of the rays to find how the beam is perturbed by the particle.

In Fig. 1.1(a), the particle is placed just below the beam's focal point. The two rays refract as they pass into and out of the particle, resulting in new trajectories for the rays. Ignoring reflections (which are minimal if the index contrast between the particle and surrounding medium is small), the momentum $\overrightarrow{p}$ carried by the optical field along rays 1 and 2 will have a magnitude of Nh/λ in the directions of the rays, where N is the number of photons following the ray's path. The changes in momentum of the two rays, $\Delta\overrightarrow{p}_1$ and $\Delta\overrightarrow{p}_2$ (thin red arrows), are represented in momentum diagrams just below the main figure. We can see from the sum of $\Delta\overrightarrow{p}_1$ and $\Delta\overrightarrow{p}_2$ that the light field

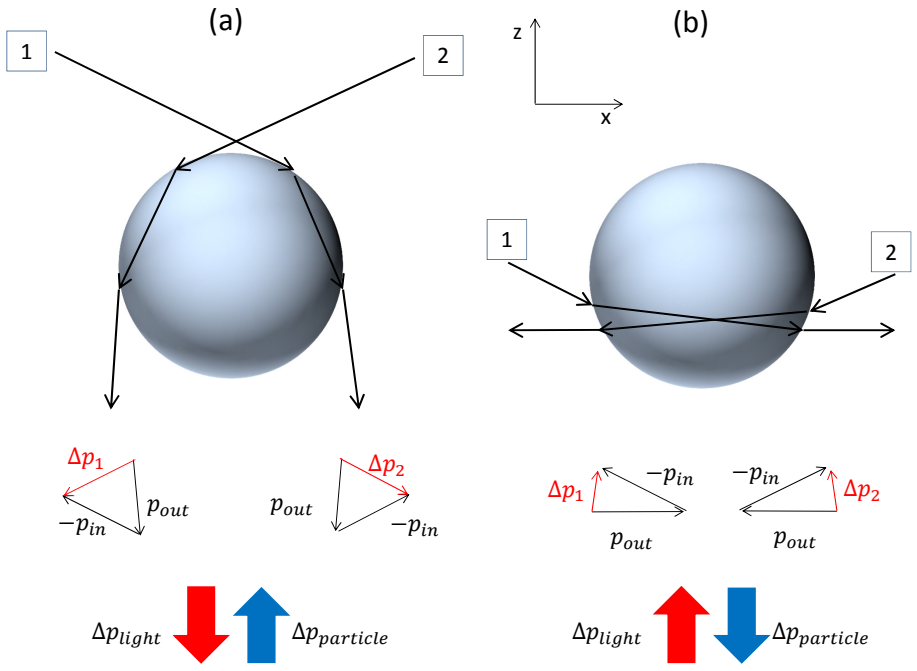

FIGURE 1.1: Ray optics diagrams tracing two rays (labeled 1 and 2) of a focused beam, demonstrating trapping in the vertical direction. In this diagram, the index of refraction of the particle is larger than that of the surrounding medium. The crossing of the two rays represents the focal point of the beam. The net changes in momentum $\Delta p_{1,2}$ (thin red arrows) of each ray are represented in ray diagrams below the main figure. (a): When a particle is placed just below the focus of the beam, the rays, with incident unit-vector momenta p_{in}, bend inward, increasing the vertical component of the unit vector of each ray and decreasing the horizontal component of the outbound momentum vector p_{out}. Due to symmetry, the horizontal components of the two rays cancel, and the net change in momentum of the light field is downward (thick red arrow). Due to momentum conservation, this results in an upward force on the particle (thick blue arrow). (b). When the particle is placed above the focus of the beam, the rays bend outward, resulting in a net downward force on the particle.

has gained downward momentum (Δp_{light}, thick red arrow), corresponding to a transfer of momentum to the particle in the upward direction (thick blue arrow). Similarly, in Fig. 1.1(b), where the particle is placed just above the beam's focal point, momentum is transfered from the light field to the particle resulting in a downward displacement. In both cases, the light field acts to push the particle *toward* the focal point of the objective, corresponding to a stable equilibrium for the particle and a trap in the z-direction.

We can evaluate the horizontal momentum transfer in a similar way. Fig. 1.2 shows the beam's focal point centered on the right hand side of the particle. The paths of rays 1

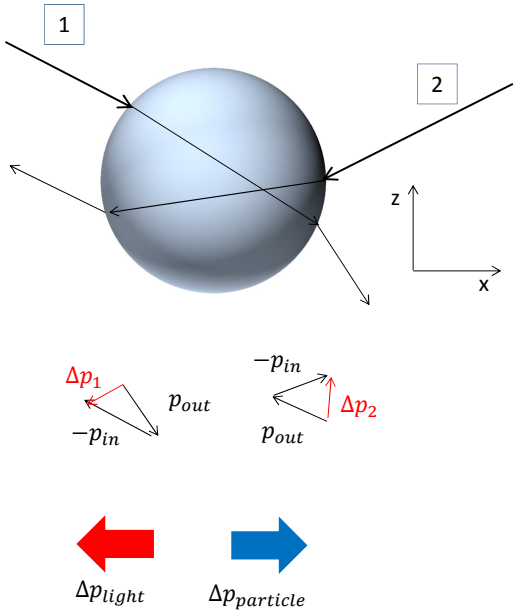

FIGURE 1.2: Ray optics picture of trapping in the horizontal direction. The sum of the momentum changes Δp_1 and Δp_2 of two two rays when the focus of the beam is on the right hand side of the particle result in a transfer of momentum to the particle in the +x direction, moving the particle toward the focus of the beam. Because of symmetry in the x-y plane, the particle will always be attracted to the focus of the beam.

and 2 no longer have mirror symmetry across the z-axis, as they did in Fig. 1.1. Instead, it is precisely this asymmetry that results in a lateral momentum transfer. Looking at the momentum diagrams for the two rays, it becomes clear that the light field has a net momentum gain in the $-x$-direction, resulting in a momentum gain of the sphere in the $+x$-direction, again pushing the particle toward the beam's focal point. Because the picture presented here has rotational symmetry around the z-axis, the lateral forces generate a particle trap in the x-y plane as well.

One does not have to look at optical forces simply through the lens of ray optics, however. It is equally equivalent to think of this system from a materials perspective. Dielectric materials exposed to an external electric field can be thought of as an ensemble of tightly packed electric dipoles, where each dipole is created by the displacement of an atom's negatively charged electron cloud from its positively charged nucleus by the incident field[7]. The "ease" with which this displacement occurs is given by the material's

susceptibility ξ_e, such that the internal field generated by these dipoles can be written as $\mathbf{P} = \epsilon_0 \xi_p \mathbf{E}$, where ϵ_0 is the permittivity of free space and we can write the particle's dielectric function as $\epsilon_p = 1 + \xi_p$.

From here we can begin to understand how and why a macroscopic object responds to an external electric field. Consider once again the case of spherical particle in a non-uniform electric field. Even as the overall particle remains charge-neutral, part of the particle is exposed to a stronger electric field than another part, resulting in neighboring dipoles that no longer cancel each other out. Instead, a charge gradient is created across the particle. Recalling that a charged object in an electric field experiences the Lorentz force $\mathbf{F} = q\mathbf{E}$, we can see that this macroscopic, charge-neutral sphere will also experience a force due to the *gradient* in the electric field. This force can be written as

$$F = \alpha \nabla E^2, \tag{1.1}$$

where α is the polarizability of the particle, which itself can be expressed in terms of its dielectric function, ϵ_p and that of the surrounding medium, ϵ_m as

$$\alpha = 3\epsilon_0 V_0 \frac{\epsilon_p - \epsilon_m}{\epsilon_p + 2\epsilon_m}, \tag{1.2}$$

where V_0 is the particle volume[8]. Note that Eq. 1.1 and the ray-optics picture generate the same result: a particle which experiences a force from a gradient electric field, and reaches a stable equilibrium in the region of highest field intensity. Within this frame, we can begin to evaluate the forces in more complex systems, such as one of relevance to the bulk of this thesis: parallel dielectric waveguides.

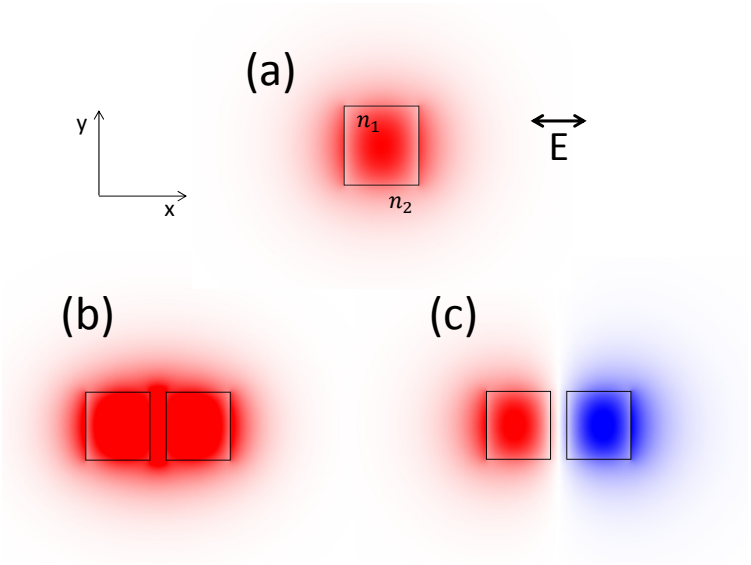

FIGURE 1.3: Field profiles of a mode in a single waveguide (a) and of the bonding (b) and antibonding (c) states of coupled dielectric waveguides. The bonding mode features a field maximum in the center of the waveguides while the antibonding mode features a field node.

1.1.3 The Forces Between Parallel Dielectric Waveguides

Dielectric optical waveguides operate due to the principle of total internal reflection: if a high-refractive index dielectric medium ($n_1 = \sqrt{\epsilon_1}$) is surrounded by a low-dielectric medium (n_2), light will remain in the high-index medium as long as the angle of the wave with respect to the interface normal is larger than the critical angle $\theta_c = \sin^{-1}(n_2/n_1)$. At the interface, however, electromagnetic boundary conditions require that the electric field component tangential to the interface is conserved across the boundary, resulting in an evanescent field in the surrounding low-index medium. An example of this is pictured in Fig. 1.3(a), which shows the cross-section of a 0.8 μm $\times$ 0.8 μm square waveguide made of dielectric material with $n_1 = 1.5$ surrounded by air, supporting a waveguide mode at $\lambda = 1500$ nm polarized in the x-direction.

As described in the previous section, the (gradient) evanescent field extending into the air around the waveguide can be used to exert forces on charge-neutral dielectric objects. Consider a situation where a second, identical waveguide is introduced and placed in

proximity to the first, with each waveguide supporting a mode at $\lambda = 1500$ nm with the field profile shown in Fig. 1.3(a). When the waveguides are close enough together, the mode profiles overlap, with the field extending from each waveguide inducing an additional polarization in its neighbor, resulting in coupling. Depending on the relative phase of the fields in the two waves, the coupling will either form bonding (in-phase) or antibonding (out-of phase) states, which will have opposite **P** field symmetry, in a manner similar to a coupling between two hydrogen atoms. Correspondingly, the modes will generate different forces. In the bonding mode, the in-phase polarization field oscillations result in the inner surfaces of the two waveguides to be oppositely charged, generating an attractive force, while in the antibonding mode, the induced fields are out of phase with one another, producing like charges on the inner surfaces and generating a repulsive force.

The initial study by Povinelli, et al. in 2005 [9] has since lead to an explosion of work on near-field optical forces. Eichenfield et al.[10] first demonstrated optomechanical coupling between a photonic waveguide and a ring resonator, while Li et al.[11] were the first to demonstrate optomechanical coupling between a single waveguide and a substrate in a photonic circuit . Riboli et al.[12] analytically investigated these forces in a 2-D geometry while Li et al.[13] experimentally verified Povinelli's earlier result in parallel silicon waveguides. Eichenfield et al.[14]and Deotare et al.[15] demonstrated coupling between optical cavities in parallel dielectric waveguides; Rosenberg et al.[16] and Wiederhecker et al.[17] demonstrated bonding and antibonding interaction in coupled ring resonators, and Yang et al.[18] demonstrated forces in hybrid surface plasmon waveguides.

The work presented here is complimentary to much of this work and expands upon it in new and interesting directions. In Chapter 2, I explore the optomechanical properties of a silicon photonic crystal nanomembrane suspended above a silicon-on-insulator

substrate. The geometry supports large area, high optical quality factor modes which generate strong attractive and repulsive forces and can couple to the mechanical degrees of freedom of the suspended membrane, resulting in cooling and amplification of the mechanical motion. I explore the interplay between opto-mechanical and photo-thermal mechanical dynamics as well as the static behavior of the membrane, revealing hysteresis and bistability due to an optical resonance which shifts as the membrane is displaced.

Chapter 3 explores the forces generated by surface plasmons, first investigating the forces between guided surface plasmon waveguides in an analog to the work by Povinelli et al. [9] Second, I extend this work into mid-infrared and terahertz frequencies ranges using structured metal surface which support surface plasmon-like waves called "spoof" surface plasmons. Finally, I discuss preliminary theoretical work on repulsive plasmon forces in high-refractive index fluids on particles near an interface, presenting the possibility for frictionless photon-assisted particle waveguiding. This work was inspired by previous work in the Capasso group by Munday et al. [19–21], who investigated repulsive Casimir forces in fluids.

Chapter 4 explores the Casimir force, which results from quantum electromagnetic fluctuations (i.e. "virtual photons") and its potential for real-world applications. Specifically, I discuss the influence of the Casimir force on the devices presented in Chapter 2, which have tunable membrane-substrate separations around 200 nm. The Casimir force, which scales as the inverse fourth power of separation, can become a dominant effect in devices with gaps around 100 nm. Simulations and preliminary results reveal the nonlinear effect that the Casimir force can have on a mechanical oscillator in close proximity to another surface.

Chapter 2

Near Field Optical Forces

2.1 Resonant Optomechanical Dynamics

Devices exhibiting resonant mechanical dynamics have applications ranging from high-precision mass and force sensing in nanoelectromechanical systems (NEMS) [22–26] to novel quantum manipulation enabled by ground-state cooling of sub-micron-scale mechanical objects. [27–30] Additionally, the concentration of light into small volumes has been shown to have broad applications due to the sensitivity of the optical mode properties to its local environment.[14, 31] Recently, there have been rapid developments in the field of optomechanics that utilize light to actuate a new class of low-mass compact resonators[24, 31–34] and that push the limits of device scalability.[13, 22, 26, 35, 36] In particular, optomechanical devices that can be fully integrated onto a silicon chip can act as active sensors or reconfigurable elements in chip-based systems.[11, 13, 17, 33] Here, we present a versatile optomechanical structure fabricated with novel stress management techniques that allow us to suspend an ultrathin defect-free silicon photonic-crystal membrane above a Silicon-on-Insulator (SOI) substrate with a gap that is tunable to below

200 nm. Our devices are able to generate strong attractive and repulsive optical forces over a large surface area and feature the strongest repulsive optomechanical coupling in any geometry to date ($g_{OM}/2\pi \approx$ -65 GHz/nm). The interplay between the optomechanical and photo-thermal-mechanical dynamics is explored, and the latter is used to achieve cooling of the mechanical mode from room temperature down to 5 K with approximately one milliwatt of power and amplification of the mode to achieve three orders of magnitude of linewidth narrowing and oscillation amplitudes of approximately 1 nm. We achieve these figures by leveraging a delocalized "dark" mode of our optical system that minimize the impact of two-photon absorption while simultaneously generating large forces in our devices. Owing to the simplicity of the in- and out-coupling of light as well as its large surface area, our platform is well-suited for applications in both mass sensing (with sub-femtogram resolution), and refractive index sensing ($\delta\lambda/\delta n_{eff} \approx$ 100 nm per unit refractive index) and optomechanical accelerometry.

2.1.1 Bonding and Antibonding Modes

It has been previously shown[9, 37, 38] that two co-propagating modes at optical frequency ωin parallel dielectric waveguides separated by a distance $s$interact evanescently, resulting in "bonding" and "antibonding" eigenmodes of the structure. As $s$decreases, the coupling between the two waveguides increases, decreasing the eigenfrequency of the bonding mode and increasing the eigenfrequency of the antibonding mode. The force between the two waveguides can be written as $F_{opt} = U_{ph} g_{OM}/\omega$, where $U_{ph} = N\hbar\omega$ is the energy flowing in the waveguides, N is the number of photons in the mode, and g_{OM} is the optomechanical (OM) coupling coefficient, defined as $d\omega/ds$. In the "bonding" configuration, the fields in the two waveguides are in-phase and generate an attractive force ($d\omega/ds > 0$), while the "antibonding" configuration corresponds to out-of-phase

fields and a repulsive ($d\omega/ds < 0$) interaction. Because the above expression for the force is general,[1] we can extend it beyond the parallel waveguide geometry and apply it to our platform, shown in Figure 2.2(a).

2.1.2 Device Design and Fabrication

The platform consists of a square silicon photonic crystal (PhC) slab containing a 30 $\times$ 30 array of holes with periodicity p = 0.92μm and hole diameter d = 0.414μm, as defined in the illustration in Fig. 2.2(b), suspended a few hundred nanometers above a Silicon-on-Insulator (SOI) substrate and is capable of generating strong attractive and repulsive forces.[39] Our devices were fabricated as follows. First, two high resistivity Silicon-on Insulator (SOI) wafers (SOITEC, device layer thickness = 220 nm, Buried Oxide (BOx) thickness = 2 μm) were thinned down using thermal oxidation, reducing the silicon device layer thickness to 185 nm. Next, oxide-oxide bonding was used to bind the two wafers together. After low-stress nitride passivation, we then dry etch away the backside of one of the handle silicon wafers using KOH to wet-etch the exposed handle silicon. This is followed by a Buffered Oxide (7:1 H_20:HF) etch to remove the exposed box layer to reveal two 185 nm silicon device layers separated by 260 nm of thermal oxide, above the 2 μm BOx layer. Devices patterns were then written using conventional 100 keV e-beam lithography on ZEP-520 positive photoresist and transferred to the top device layer using inductively-coupled plasma reactive-ion etching. Finally, the oxide layer between the two Si slabs is removed by Hydrogen Fluoride Vapor-phase Etching to release the top device layer and provide the gap between the top and bottom membrane. The process is described visually in (Figure 2.1(a)). A cross section of the layer stack taken using a Scanning Electron Microscope is shown in Fig. 2.1(b).

[1]The expression for the force is only strictly true when the (complex) wavevector is constant under translation, though it can still be used when the change in optical Q is small over the distance ds.

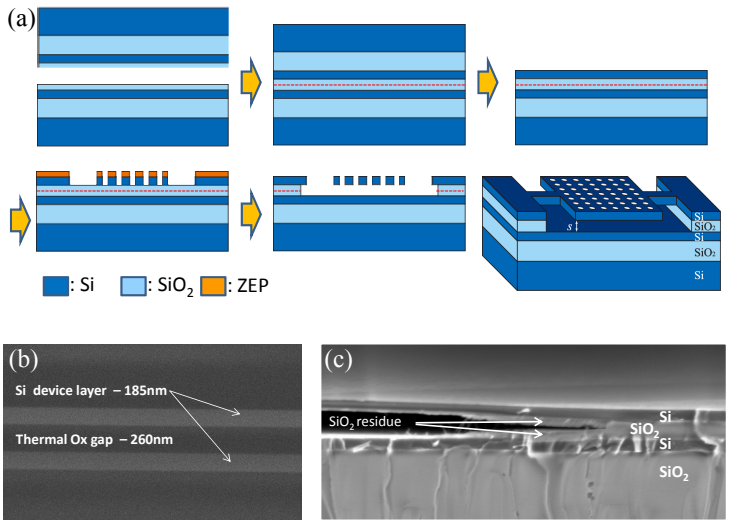

FIGURE 2.1: (a) Fabrication process. Two SOI wafers are bonded together with an oxide-oxide bonding process, creating a sandwich structure with two thin silicon device layers in the middle. SEM image of the sandwich shown in (b). Removal of one of the handle wafers with KOH and the thick oxide layer with BOE leaves a double-device layer chip, with the two Si layers separated by a 260 nm oxide gap. E-beam lithography followed by Reactive Ion Etching of the top silicon layer and HF Vapor Etching of the thermal-oxide gap layer create the final device (last panel of (a)). (c): HFVE selectively etches at a higher rate along the oxide-oxide bond interface (red-dashed line) than it etches through the oxide layer, resulting in SiO_2 residue along the Silicon surfaces.

The whole process of thermal oxidation, oxide-oxide bonding, and removal of the handle silicon results in stresses in the multi-thin film layer structure, which leads to buckling of the silicon device layer when it is released. As a consequence of these processing and fabrication steps, we have also observed faster oxide HFVE rates in the bond-interface region that result in the presence of residual oxide close to the silicon membrane, which can be wider than 1 μm at the edges of the etch area (Figure 2.1(c)). A bending moment $M_{||}$ due to the residual stress in the device layer (curved purple lines, Figure 2.4(a)i) causes a strong upward force on the devices fabricated with simple arms (Fig. 2.3(a) and 2.4(b)i), forcing them to deflect more than 300 nm. An additional annealing step was performed on some devices at 500 C for 1 hour in a nitrogen environment in order to maximize optical and mechanical quality factors.

The device parameters p and d were chosen to result in an antibonding mode (profile

shown in Fig. 2.2(c)) in the wavelength range accessible by our lasers (1480-1680 nm). We note that the field symmetry indicates that this is a dark mode of the structure and thus should not couple directly to free space. However, due to the finite size of our membrane, we are able to break the structural symmetry to access the mode.[40] The optical resonance frequency can be tuned by controlling the membrane-substrate separation s (red line in Figure 2.2(d). Using numerical modeling performed in COMSOL Multiphysics, we find that the g_{OM} (blue line, Figure 2.2(d)) of the mode is 2π × -3.3 GHz/nm at s = 350 nm and increases to 2π × -150 GHz/nm at s = 50 nm.

We explore this range of separations using novel techniques that we developed to leverage built-in stresses in the substrate. Commercial SOI wafers often have high levels of built in stress introduced during the process that bonds the device layer and buried oxide layer to the handle substrate,[41] but the sign and precise strength of the stress are often unknown. Furthermore, devices made in our double-SOI platform experience an additional bending moment tangential to the SiO_2 surfaces exposed during the HFVE process that produces an upward force on all undercut structures (see Supplement). To control these effects, we first introduce "accordion-like" arrays of narrow beams (Fig. 2.2(a) inset) to each arm that relieve the compressive (tensile) stress and prevent out-of plane buckling (breaking) through in-plane deformation of the accordion structure.[41] Next, we introduce a rectangular array of etch-holes at the base of each arm that rotate the axis of the bending moment by 90 degrees ($M_\perp$) and thus control the resulting force on the membrane arms. A simple rectangular etch-hole pattern (Figure 2.4(a) ii.) forms a "bridge" and forces the bending moment to act in a direction of much greater mechanical stiffness (red arrows), resulting in a significantly smaller upward deflection of the device (Fig. 2.3(d) and 2.4(b) ii.). Devices which do not contain either of these stress management techniques, such as the one pictured in Fig. 2.3(a), deflect upward by >350

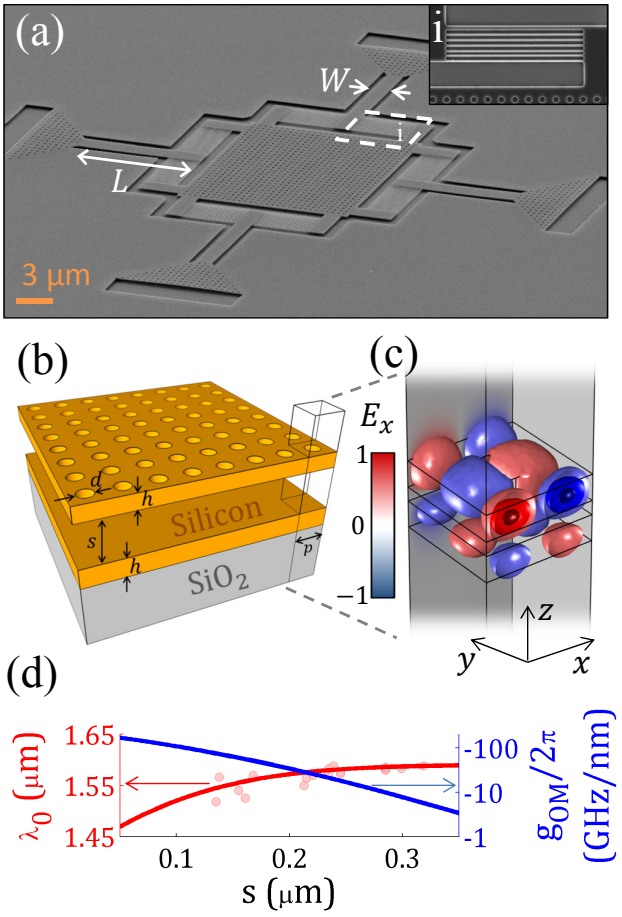

FIGURE 2.2: (a) SEM image of a device consisting of a h = 185 nm thick silicon membrane patterned with a square-lattice photonic crystal with a 30×30 periodic hole array of period p = 0.92 μm and hole diameter d = 0.414 μm suspended 165 nm above a Silicon-on-Insulator (SOI) substrate (h = 185 nm, buried oxide layer = 2 μm, cross-section shown schematically in (b)). The membrane is supported by four arms (L = 19.3 μm, W = 2.75 μm) that are terminated on their far ends by arrays of etch holes and on their near ends by "accordion-like" structures (inset i) which provide lithographic control of membrane-substrate separation. (c) A 3D optical mode simulation shows the x-component of the electric field of a single unit cell of the geometry in (b) with s = 100 nm for an antibonding mode of the structure at λ_0=1570 nm. The antisymmetric field symmetry with respect to the gap between the membrane and the substrate implies that this optical mode generates a repulsive force. (d) The calculated resonance wavelength λ_0 (red line) of the mode in (c) is plotted with data points (red circles) representing 16 different devices with identical membrane designs but different membrane-substrate separations. The separations were determined by interferometric measurements using an optical profilometer. The blue line is optomechanical coupling coefficient of the mode and is proportional to the slope of the red line ($g_{OM} \propto$ -dλ/ds).

nm, as shown in the optical profilometer measurement in Fig. 2.3(b). Introduction of the accordion-like structure and a rectangle-like array of etch-holes decrease the membrane deflection by over an order of magnitude (Fig. 2.3(d,e)). Importantly, by replacing the rectangle-like etch-hole pattern with a triangular one, we make the bridge less stiff farther from the device arm, resulting in a large upward deflection in the back of the bridge (large green arrow), while only generating a small deflection in the front (small green arrow). More importantly, however, is that this geometry generates a downward force on the device, whose strength is controllable by the pitch of the triangular array shape. On this device, we are able to deflect the membrane downward as seen in Fig. 2.3(g,h) by 105 nm. Fig 2.4(c) and (d) show optical and profilometer images of structures made up of two device arms and two sets of accordion structures in the center. As is clear in the images, the devices with the widest triangle etch-hole pattern (i.) generate the largest downward deflection (blue color in (d)). The narrower triangle pattern (ii.) generates a small downward deflection, the rectangular pattern (iii.) results in a small upward deflection, and the etch-hole free device (iv.) suffers from a large upward deflection.

These experimental observations were verified by numerical modeling of the devices under the same compressive stress conditions performed in COMSOL Multiphysics (Fig. 2.3(c,f,i)).This is an important and novel feature of our platform that gives us independent lithographic control of the membrane-substrate separation of different devices on the same chip. We have fabricated devices (red circles, Fig. 2.2(d)) with separations as small as 135 nm, corresponding to a g_{OM} of -$2\pi \times 65$ GHz/nm, which is the largest yet value of g_{OM} seen in a repulsive system[17] by a factor of four. Finally, we note that our devices are designed such that the majority of device deflection occurs in the support arms. Simulations show that the membrane has a radius of curvature of 2 cm for 100 nm deflections, such that it remains essentially flat during our experiments. However,

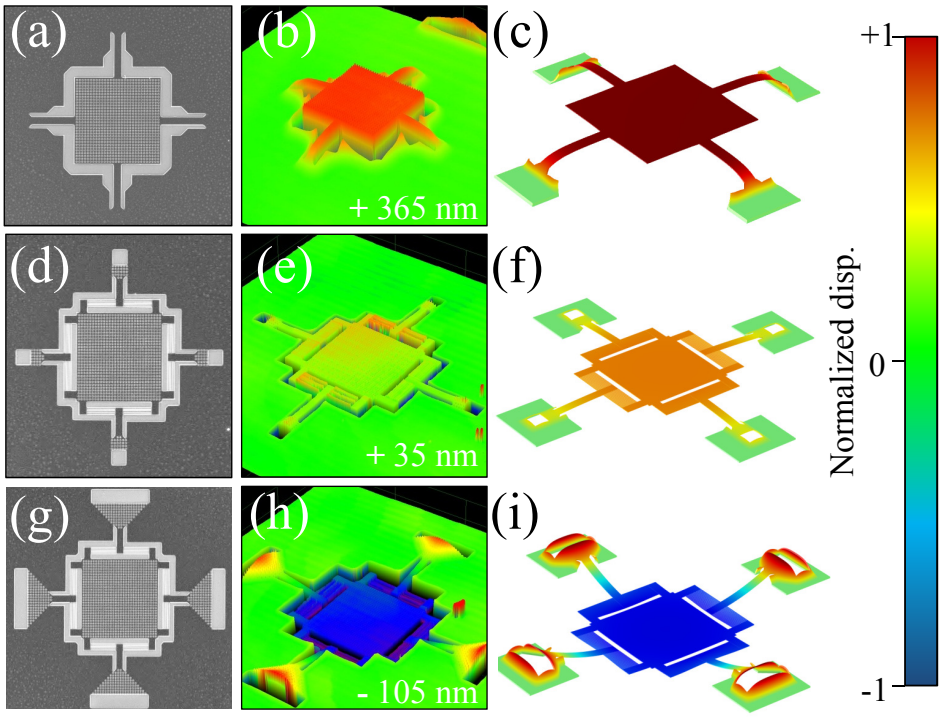

FIGURE 2.3: Scanning Electron Microscope (SEM) images (a,d,g), optical profilometer images showing interferometric measurements of height (b,c,h) and mechanical simulations in COMSOL Multiphysics confirming the behavior measured by the profilometer (d,f,i) are shown for three separate devices. The first device (a) has simple support arms which offer no control over the stresses inherent in the wafer. The result is a membrane which deflects strongly upward by 365 nm (b,c) due to compressive stress in the membrane and an upward torque caused by a bending moment at the Si-SiO_2 etch boundary. The second device (b) has an accordion-like structures between the arms and the membrane (see inset, Fig. 2.2(a)) and an approximately rectangular etch-hole pattern at the base of each arm to combat compressive stress and the bending moment at the etch boundary. The result is a device which only deflects upward 35 nm (e,f), an order of magnitude improvement over the device in (a). The triangular design of the etch-hole pattern in the third device (g) utilizes the torque induced at the etch boundary to generate a controllable downward deflection. The result (h,i) is a membrane which deflects downward 105 nm from the surrounding silicon layer.

confocal measurements using an optical profilometer on fabricated devices indicate that anisotropy intrinsic to the HFVE process can induce tilts in our devices that can be as large as 10 nanometers from side to side. Further modifications to the device design and fabrication process should be able to minimize this tilt, making this system a good candidate not only for current MEMS technologies but also for other innovative structures requiring parallel-plate geometries, such as plate-plate Casimir oscillators.

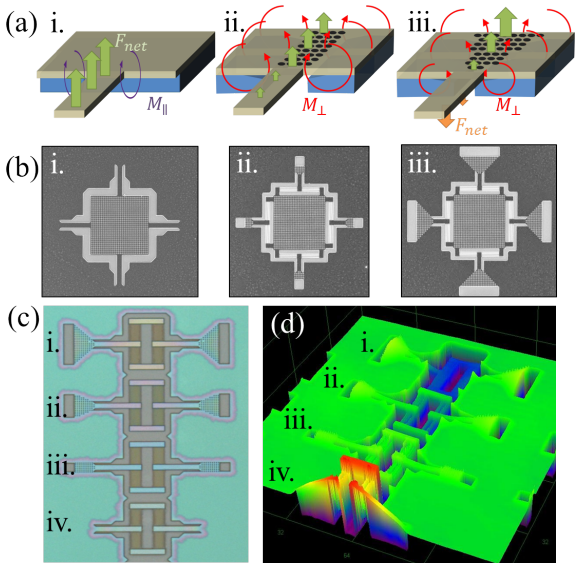

FIGURE 2.4: (a) Force diagram demonstrating our method for counterbalancing and counteracting the upward deflection caused by the oxide residue. i. With no modifications, the bending moment $M_{\parallel}$ (purple arrows) caused by the undercut SiO_2 (rendered in blue) etch-boundary produces a strong upward force (green arrows) on the membrane arms. ii. Etch-holes are introduced in a rectangular array at the base of the arm, forming "bridges" and changing the axis of the bending moment ($M_{\perp}$, red arrows). This results in an upward torque along the much stiffer axis which results in a smaller upward deflection of the device arms. iii. The shape of the hole array is triangular, making the bridge less stiff farther from the device arm, which results in a larger upward deflection in the back of the bridge than in the front of the bridge. The net effect of this tilt is to deflect the device arms downward (orange arrows). Devices corresponding to the diagrams in (a) are shown in (b), as well as Fig. 2 in the main text. Optical image (c) and interferometric measurement of the height profile (d) taken using the optical profilometer of four devices consisting of only two support beams and the "accordion" structure meant to absorb compressive/tensile stress. The termination of the arms varies and corresponds to the net deflection of the device, as follows: i. Wide triangle (large downward deflection) ii. Narrow triangle (small downward deflection) iii. Rectangle (small upward deflection) iv. No etch holes (large upward deflection).

2.1.3 Optomechanical and Photothermal Dynamics

Actuation in our system is achieved by a combination of optical and photothermal forces, the latter of which arises from absorption of light in the cavity that generates displacements through thermal expansion at the Silicon-SiO_2interface.[27, 33, 34, 42] Light absorption can also directly change the optical properties of the mode by modifying the refractive index of the silicon through the thermal-optic effect (dn/dT). In previous studies, which featured wavelength-scale mode-volumes ($\approx (\lambda_0/n)^3$) and poor thermal transport properties,[43, 44] the thermo-optic effect obscured the underlying

optomechanics,[45] due in large part to the strong two-photon absorption in silicon at near-IR frequencies. By employing a system containing extended photonic crystal modes[39, 46] with large optical mode volumes ($\approx 1500(\lambda_0/m)^3$) and thermal diffusion rates γ_t ($\approx$ 450 kHz) orders of magnitude larger than those of microcavity geometries, we avoid the problems commonly associated with silicon optomechanical systems while still achieving optical forces comparable to those achieved with microcavities.

To quantify the photo-thermal-mechanical (PtM) effects relative to the optomechanical (OM) effects, we define coefficients

$$L_{OM} = \frac{\omega_0}{g_{OM}} \tag{2.1}$$

and

$$L_{PtM} = \left[DC_{th}^{-1}\Gamma_{abs}\right]^{-1} \frac{\Omega_m^2 + \gamma_t^2}{\gamma_t} \tag{2.2}$$

as the inverse of the optical and photo-thermal forces, respectively, per unit stored optical energy in the cavity, where D is the material- and geometry-dependent thermal-mechanical force coefficient in units of Newtons per Kelvin (positive or negative for attractive or repulsive forces, respectively), $C_{th}$is the heat capacity, and Γ_{abs} is the total absorption coefficient of the material. In our devices, thermal expansion causes a downward deflection, effectively generating an attractive force (F_{pth}) between the membrane and the substrate, which puts the photo-thermal force in competition with the repulsive optical force. We note that F_{pth} and L_{PtM} are essentially independent of

membrane-substrate separation,[2] while, as shown in Fig 2.2(c), F_{opt} and L_{OM} are highly sensitive to changes in s.

Coupled-mode theory [47] is used to study how the coupling of the thermal, optical and mechanical degrees of freedom affects a device's mechanical angular frequency, Ω_m and its linewidth, Γ_m. (For full derivation, see Eq. 1-19 in supplement.) Physically, an optical cavity with linewidth κin a free-standing membrane undergoing Brownian motion (with an RMS amplitude δs at Ω_m) is perturbed by the optical field or thermal gradient such that the resonant frequency shifts ($\omega_0^{'} = \omega_0 + g_{OM}\delta s + \frac{d\omega}{dT}\delta T$), thus modulating the detuning $\Delta_0' \equiv \omega_l - \omega_0'$ between an incident laser source at ω_l and the shifted cavity resonance. This modulation in Δ_0' further modulates the stored cavity energy U_{ph}, the forces F_{opt} and F_{pth} and hence the overall displacement, which in turn modulates the optical resonance frequency and forms a feedback loop. This feedback has both in-phase and quadrature (out-of-phase) components that result in a mechanical frequency perturbation Ω_m and a mechanical linewidth perturbation Γ_m, respectively, both of which have odd symmetry with respect to Δ_0'.

Modifications to Ω_m can take two forms. The applied forces can act in the same direction of the vibrational restoring force, resulting in a stiffening ($\delta\Omega_m > 0$), or in the opposite direction, resulting in softening ($\delta\Omega_m < 0$). Similarly, modifications to Γ_m, known as "induced back-action[28]," describe the direction of energy flow between the mechanical mode and the optical or thermal field. A net energy flow into the mechanical mode decreases Γ_m and corresponds to mechanical amplification, while a net energy flow out of the mechanical mode increases Γ_m and corresponds to increased damping (i.e. mechanical cooling). The strengths and signs of the modifications to the mechanical motion due to PtM and OM effects depend on the magnitudes of the respective

[2]Near-field thermal heat-transfer will modify $_t$ by a small amount, though we ignore this small effect in our analysis here for simplicity.

forces (L_{OM}^{-1},L_{PtM}^{-1}) as well as the strength of the optomechanical coupling, g_{OM}. This results in OM perturbations which are independent of the sign of the force (g_{OM}/L_{OM}) and PtM perturbations which depend on the signs of both the optical and photothermal forces (g_{OM}/L_{PtM}).

2.1.4 Measurements

To study these dynamics and characterize our devices, we use the setup illustrated in Figure 2.5. Briefly, an optical fiber mounted on a z-translation stage with ϕ_x and ϕ_y angle control centered above the suspended membrane in the Rugar configuration[48] (detail in inset i.) is used to couple light into a device and also collect the signal back-reflected by the device. The chip containing the device rests on a four-axis (x,y,θ_x,θ_y) stage platform. The motorized x-y stage contains closed-loop feedback that allows us to repeatably align the fiber to the sample with sub-100 nm resolution, while the manual θ_x and θ_y tilt stages are used to keep the fiber-substrate distance constant under x-y translation. The whole setup is placed inside a high vacuum chamber (10^{-5} torr) to eliminate gas damping of the mechanical vibrations.

The stage construction and the vacuum chamber can be seen in panels (a) and (b), respectively, of Figure 2.6. We visually confirm fiber-substrate alignment using a camera which provides a side-on view of the fiber and substrate Fig. 2.6(c). To image the sample, we step the x-y stage and collect the reflected signal at each step, building up the image pixel by pixel. We are able to clearly image devices Fig. 2.6(d) with this technique with $1\mu m$ feature resolution to obtain optimal fiber-sample alignment. After using the θ_x and θ_y stages to flatten the x-y stage motion with respect to the optical fiber, we use the motorized ϕ_x and manual ϕ_y axes mounted on the z-stage to align the cleaved facet of the fiber to the substrate. The method for doing this is depicted in (e). To

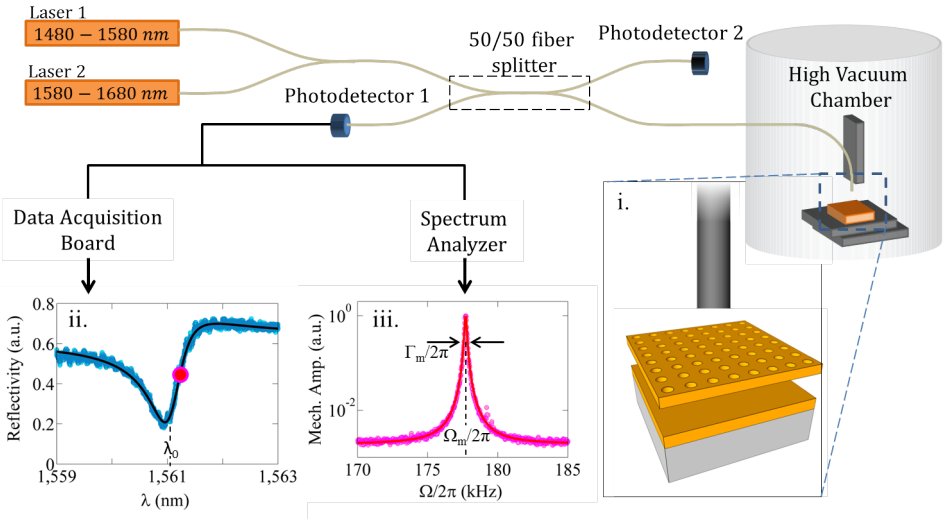

FIGURE 2.5: Experimental apparatus. The outputs from two tunable near IR lasers (λ = 1480 nm-1580 nm and λ = 1580 nm-1680 nm) are combined using a fiber-directional coupler. Half of the signal is diverted to Photodetector 2 as a reference and half is coupled into a high –vacuum chamber (HVC) via a custom made fiber-feedthrough port. The cleaved fiber is positioned above the center of the device, so that the cleaved fiber facet is parallel to the membrane (inset i., not to scale). The reflected optical signal is measured at Photodetector 1. Optical reflection spectra are taken by sweeping the lasers' wavelengths across the optical resonances and collecting the signal via the Data Acquisition (DAQ) board. The optical resonance centered at λ_0 = 1561.1 nm (inset ii) has a Fano shape (black line) and Q_{opt} = 2500. Mechanical spectra are obtained by taking the Fourier transform of the photodetector signal using the spectrum analyzer (SA) to measure the small thermal vibrations of the membrane. The fundamental mechanical resonance (inset iii), defined by resonance frequency Ω_m and linewidth Γ_m, is shown for a low-power measurement at λ=1561.2 nm (red dot, inset ii.).

start, we sweep the phi_x axis forward and backward while the fiber is positioned over an unpattered portion of the silicon wafer, resulting in a reflection curve showing fringes generated by the fiber-substrate cavity, such as the one pictured. When the fiber facet is perfectly parallel with the substrate (positions A, D, and in the middle of B and C in the graphic), we expect the signal to be maximized due to the build up of multiple reflections and we expect the fringes to be widest, since the facet-substrate separation should be at a minimum. After aligning the ϕ_x axis, we manually adjust the ϕ_y axis to maximize the amplitude of the ϕ_x sweep.

Optical spectra (Fig. 2.5, inset ii) were collected by sweeping the tunable laser sources across the optical resonance. Mechanical spectra (Fig. 2.5, inset iii) were collected

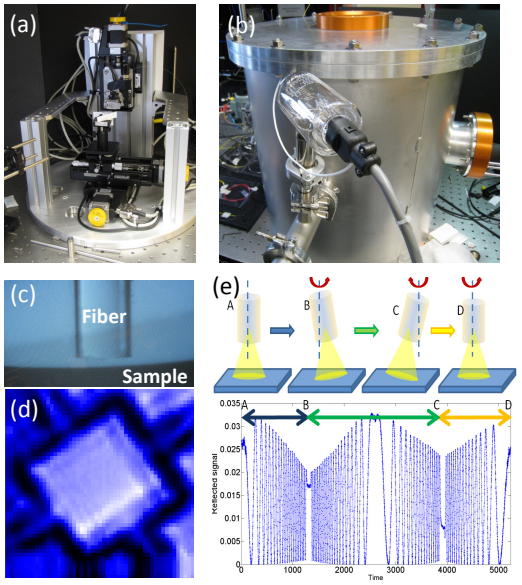

FIGURE 2.6: (a) Picture of multi-axis positioning system. This solid construction is placed inside of the vacuum chamber (b). Viewports on the side and top allow us to visually align the fiber to the sample when the system is under vacuum. A camera outside the side viewport provides images of the fiber and sample (c), which we use for coarse positioning and alignment. Stepping the x-y stage in a square grid, and collecting the back-reflected signal, we can image the devices (d) to obtain optimal fiber-sample alignment. (e) Graphic and signal data describing the planarization of the fiber to the substrate

at fixed excitation wavelengths on either side of the optical resonance by analyzing the signal reflected off of our membranes in a real-time spectrum analyzer (Tektronix RSA3303B). We measure the dynamic shifts in Ω_m and Γ_m of the fundamental vibrational mode of two different devices by fitting the measured mechanical resonance to a Lorentzian lineshape, and the best-fit parameters for Ω_m and Γ_m are plotted in Figure 2.7 (green circles) as a function of laser wavelength.

2.1.5 Results

We first explore an upward-deflected device (Fig. 2.2(d)) with membrane-substrate separation s = 300 nm at an incident optical power of 50 μW, in Fig 2.7(a). We observe blue-detuned ($\Delta_0' > 0$) cooling and softening and red-detuned ($\Delta_0' < 0$) amplification and stiffening, which fit well to theoretical predictions (black lines) for L_{OM} = -95

μm (g_{OM} = 2π × -3.3 GHz/nm) and L_{PtM} = 15 μm. As expected, PtM effects (red dashed lines) to dominate the dynamics due to the large membrane-substrate separation. Furthermore, we see no OM contributions (blue-dashed line) to the linewidth dynamics as a consequence of operating in the deep "sideband-unresolved" limit[28] where κ/Ω_m $> 10^6$. In this regime, the optical force acting on the mechanical oscillator is effectively instantaneous with respect to the oscillator period. All back-action in our devices is provided by PtM effects.

In a downward-deflected device with s = 160 nm, (Fig. 2.7(b), image in Fig. 2.3(e)), the increased OM contributions (blue-dashed line) to the overall dynamics (black line) flips the sign of the $\delta\Omega_m$curve compared to the upward-deflected device. The magnitudes of $\delta\Gamma_m$and $\delta\Omega_m$are similar to those in Fig. 2.7(a) but were achieved with an order of magnitude less optical power (6 μW). This is attributed to an increase in g_{OM} to 2π × -30 GHz/nm (L_{OM}= -6.4 μm), while L_{PtM} remained constant. When the incident optical power is increased to 30 μW (Figure 2.8(a)), a range of wavelengths (grey shaded region) exists in which Γ_m reaches its experimental minimum.[49] In this region energy is being added to the mode faster than it can dissipate, resulting in a "regenerative oscillation" amplitude on the order of a nanometer that scales linearly with power. This regime is of interest for applications in mass-sensing. For example, the mechanical response at λ = 1561.5 nm (red star), plotted in Fig 2.8(b), has $\Gamma_m/2\pi$ = 70 mHz, which corresponds to a mass sensing limit of 0.3 fg. Further optimization of the structure, with this application in mind, may result in even better mass sensitivity.

On the other side of the optical resonance, optical cooling takes place. The strength of the cooling is quantified by the mode's effective temperature T_{eff},[27] which, from the equipartition theorem, we can write as $T_{eff}/T_0 = \Omega_{m0}^2/\Omega_m^2 \times \Gamma_{m0}/\Gamma_m$, where,$\Gamma_m$ = $\Gamma_{m0} + \delta\Gamma_m = \Gamma_{m0}(1 + \beta P)$ T_0 is room temperature and β is a collection of constants

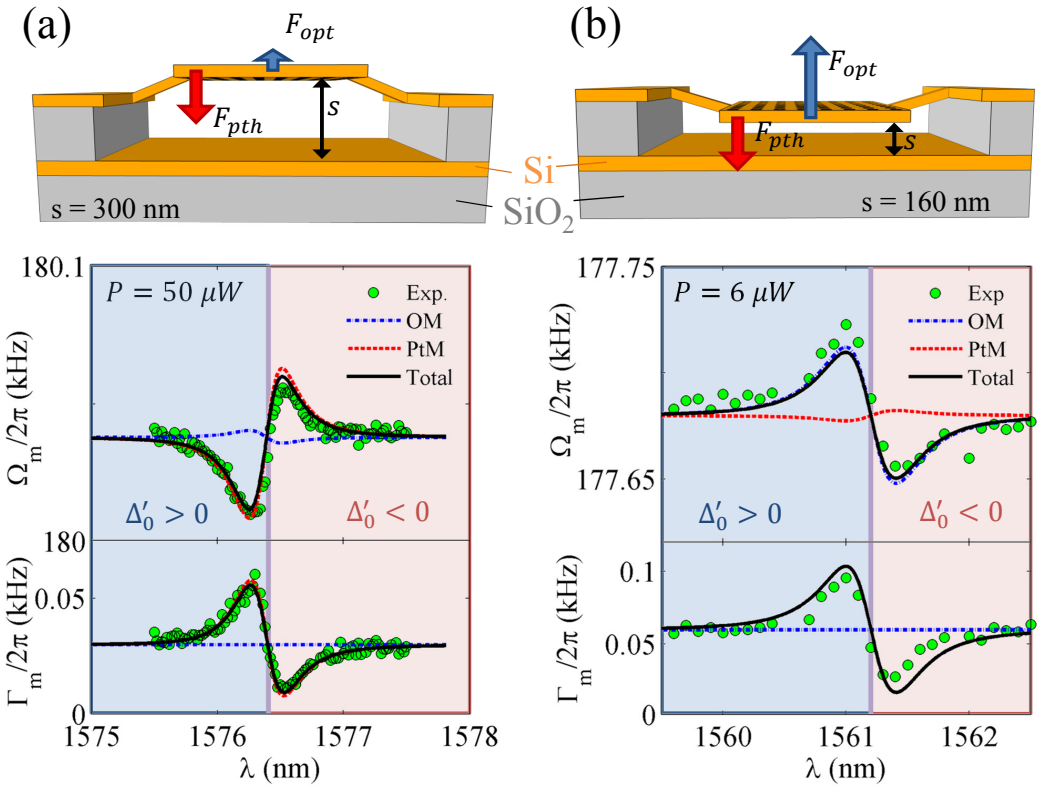

FIGURE 2.7: Optomechanical coupling curves for two devices with different membrane-substrate separations experiencing photothermal and optical forces. Data (green circles) were collected by measuring the vibrational spectra (Fig. 2.5, inset iii.) for several wavelengths around the cavity resonance. The data in (a) correspond to the device in Fig. 2.3(d), whose cavity resonance is centered at λ_0=1576.4 nm. The data in (b) correspond to the device in Fig. 2.3(g), whose cavity resonance is centered at λ_0=1561.1nm. The photothermal force F_{pth} (red arrows, top insets) is attractive and approximately constant in both devices. The repulsive optical force F_{opt} (blue arrows), increases in magnitude from (a) to (b), as the magnitude of $g_{OM}/2\pi$ increases from -3.3 GHz/nm to -30 GHz/nm. In our system, F_{opt} and F_{pth} have opposing effects on Ω_m (top panels). In (a), photo-thermal-mechanical (PtM) dynamics (red dashed lines) dominate and the device undergoes softening ($\delta\Omega_m < 0$) when the laser is blue-detuned ($\Delta_0^{'} > 0$, blue shaded region) and stiffening ($\delta\Omega_m > 0$) when red-detuned ($\Delta_0^{'} < 0$, red shaded region). In (b), optomechanical (OM) dynamics (blue dashed lines) dominate and the device undergoes blue-detuned stiffening and red-detuned softening. Bottom panels: Both devices undergo blue-detuned cooling ($\delta\Gamma_m > 0$) and red-detuned amplification ($\delta\Gamma_m < 0$) due to PtM effects only. The maximum values of $\delta\Omega_m$ and $\delta\Gamma_m$ shown in both (a) and (b) are approximately equal in magnitude, but the dynamics in (b) were achieved with an order of magnitude less optical power due to the of strength of opto-mechanical coupling (g_{OM}) in (b).

defined precisely in the Supplementary Materials. We quantify the strength of the mechanical cooling by exciting the structure at a fixed wavelength (λ = 1560.8 nm, blue star in Fig. 2.8(a)) and at six optical powers in the range of 6 μW (red line) to 200 μW (purple line). We note that $T_{eff}$is also proportional to the area under the mechanical resonance curves (blue shaded regions). As other processes can cause linewidth broadening without cooling, it is important to perform this check to confirm that we are indeed cooling the vibrational mode. The effective temperature of the mode at the six measured powers is shown in the Fig. 2.8(c) inset, where the colors of the circles correspond to the colors of the curves in the main figure. We find that T_{eff} reaches 22 K at 200 μW and 5.8 K at 1 mW, according to the curve fit (black line). These values, coupled with the large device mass, large g_{OM}, and ease of in- and out-coupling of light, make this platform an intriguing candidate for optical accelerometry,[31] which utilizes optomechanical cooling to damp mechanical ringdown.

2.1.6 Derivation of Dynamics

Cavity optomechanical dynamics can be represented by a system of two equations describing the stored cavity energy and the mechanical motion:

$$\frac{da}{dt} = -\frac{\kappa}{2}a - i\left(\Delta + g_{OM}x\right)a + \sqrt{\kappa_e} \tag{2.3}$$

$$\frac{d^2x}{dt^2} + \Gamma_m\frac{dx}{dt} + \Omega_m^2 x = -\frac{g_{OM}\left|a^2\right|}{m_{eff}\omega_0} \tag{2.4}$$

Equation 2.3 describes the properties of the optical cavity, where $a$is the amplitude of the optical field in the mode, $\epsilon$is the amplitude of the field incident on the structure

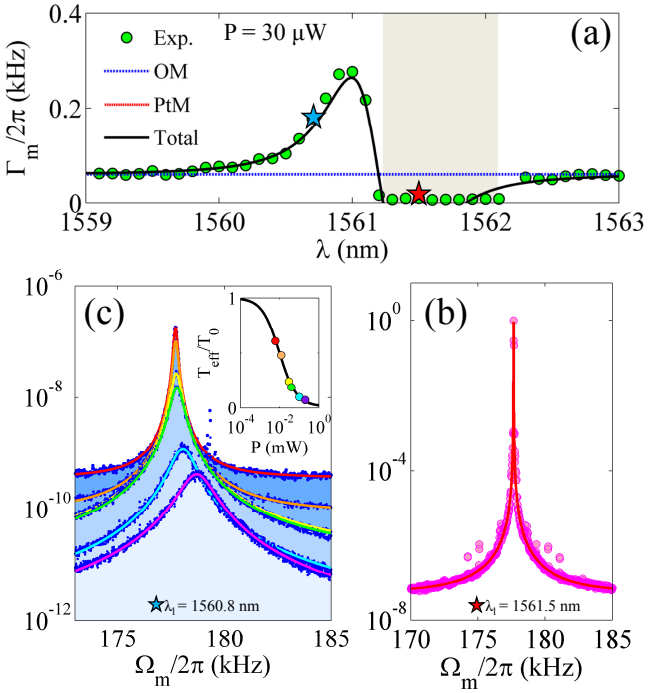

FIGURE 2.8: (a): Mechanical linewidth of the device (green circles) in Fig 2.7(b) as a function of laser wavelength at an incident power of 30 μW, showing blue-detuned cooling and red-detuned amplification. The overall dynamics (black line) are dominated by photo-thermal mechanics (red dashed line, not seen), since optomechanical interactions (blue dashed line) are negligible. On the red side of the resonance between 1561.2 nm and 1562.1 nm (grey shaded region of (a)), the mechanical linewidth hits a floor as the system undergoes generative oscillations. (b): The vibrational spectrum of the mode when λ_l= 1561.5 nm is shown (pink circles) with the lorentzian fit (red line), where $\Gamma_m/2\pi$ = 70 mHz. (c): On the other side of the resonance, the mechanical vibration is cooled. The mechanical resonance is plotted (dark blue dots) and fit for six powers: 6 (red line), 12 (orange line), 30 (yellow line), 40 (green line), 100 (blue line), and 200 μW (purple line). In our system, linewidth broadening is due to mechanical cooling only. Thus, Γ_m and the area under the mechanical resonance curves (blue shaded regions) are both be proportional to the effective temperature of the mode (T_{eff}), which is plotted as a function of power in the inset. The colors of the data points correspond to the colors of the lines in (c), and the points are fit to the expression in the text. At 1 mW, the effective temperature of the mode is 5.6 K when cooled from room temperature.

at,ω_l $\kappa_e$is the external coupling rate such that $\kappa_e|\epsilon|^2$ is the incident optical power, and. Equation 2.4 describes the mechanical behavior, where is the oscillation amplitude, and are the mechanical linewidth and frequency, respectively, and is the effective mass of the mechanical element. The perturbations to Ω_m and Γ_m from opto-mechanical coupling arise from in-phase ($\propto$ x(t)) and quadrature ($\propto$ x $\dot{(t)}$) driving terms driving the harmonic oscillator, and can be obtained by linearizing (1) and (2). These expressions can be written as functions of Δ in the so-called "sideband-unresolved" limit[28] (Ω_m$\ll \kappa/2$)

as

$$\delta\Omega_m = \Omega_m \frac{g_{OM}^2}{\omega_0^2 K_m} \left(\frac{\frac{\kappa_e}{2}|\epsilon|^2}{\frac{\kappa}{2}^2 + \Delta_0^2} \right) \frac{2\Delta\omega_0}{\frac{\kappa}{2}^2 + \Delta_0^2} \tag{2.5}$$

and

$$\delta\Gamma = -\Omega_m \frac{g_{OM}^2}{\omega_0^2 K_m} \left(\frac{\frac{\kappa_e}{2}|\epsilon|^2}{\frac{\kappa}{2}^2 + \Delta_0^2} \right) \frac{2\Delta\omega_o}{\left(\frac{\kappa}{2}^2 + \Delta_0^2\right)} \frac{2\Omega_m \frac{\kappa}{2}}{\left(\frac{\kappa}{2}^2 + \Delta_0^2\right)} \tag{2.6}$$

where $K_m = \Omega_m^2 m_{eff}$ is the mechanical spring constant, and.$\Delta_0 = \Delta - g_{OM}x$ In this limit, it is clear from the above equations that the change in the linewidth of the resonator must be significantly smaller than the change in the mechanical frequency. The two equations differ only by the term at the far right of Eq. 2.6, relating Ω_m to,$\kappa/2$ which by definition is $\ll 1$ in this limit. When thermal-optical and thermal-mechanical effects are included, equations 2.3 and 2.4 must be modified and a third equation describing the system's thermal properties must be added. The system then becomes:

$$\frac{da}{dt} = -\frac{\kappa}{2}a - i\left(\Delta - g_{OM}x - \frac{d\omega_0}{dT}\delta T\right)a + \sqrt{\kappa_e} \tag{2.7}$$

$$\frac{d^2x}{dt^2} + \Gamma_m \frac{dx}{dt} + \Omega_m^2 x = -\frac{g_{OM}\left|a^2\right|}{m_{eff}\omega_0} - \frac{D}{m_{eff}}T \tag{2.8}$$

$$\frac{dT}{dt} = -\gamma_{th}T + C_{th}^{-1}\left(\Gamma_{lin} + \Gamma'_{TPA}|a|^2\right)|a|^2 \tag{2.9}$$

where D is the thermal mechanical force coefficient in units of N/K, (D>0 for downward thermally-induced displacements), γ_{th} is the thermal time constant, C_{th} is the thermal heat capacity, Γ_{lin} is the linear absorption rate of silicon and Γ'_{TPA} is the two-photon absorption rate (included for competition) with the dependence on field intensity $|a|^2$ explicitly removed from the expression for clarity, such that the total absorption rate is $\Gamma_{abs} = \Gamma_{lin} + \Gamma'_{TPA}|a|^2$ To solve this system for its mechanical dynamics, we must first linearize it[5], rewriting $x(t)=x_0+\delta x(t)$, $a(t)=a_0+\delta a(t)$, and $T(t)=T_0+\delta T(t)$. The linearization of Eq. 2.9 results in separate expressions for T_0 and for $\delta T(t)$, though for this derivation, we are only interested in the equation for $\delta T(t)$, which takes the form

$$\frac{d}{dt}\delta T(t) = -\gamma_{th}\delta T(t) + c_{th}^{-1}\Gamma_{abs}\left(a_0\delta a^*(t) + a_0^*\delta a(t)\right). \tag{2.10}$$

Converting into Fourier space, this expression becomes

$$\delta T(\omega) = \frac{c_{th}^{-1}\Gamma_{abs}}{-i\omega + \gamma_{th}}\left(a_0\delta a^* + a_0^*\delta a\right), \tag{2.11}$$

where the expression for $a_0\delta a^* + a_0^*\delta a$ can be found by linearizing Eq. 2.7 and solving for a_0 and δa independently, then converting to Fourier space. Doing this, one finds

$$\begin{aligned} a_0\delta a^* + a_0^*\delta a = i|a_0|^2\left(g_{OM}\delta x(\omega) + \frac{d\omega}{dT}\delta T(\omega)\right) \\ \times\left[\frac{1}{\frac{\Gamma}{2} + i\left(\omega + \Delta_0'\right)} - \frac{1}{\frac{\Gamma}{2} + i\left(\omega - \Delta_0'\right)}\right]. \end{aligned} \tag{2.12}$$

Plugging Eq. 2.11 into Eq. 2.12 we find that

$$a_0\delta a^* + a_0^*\delta a = i|a_0|^2 g_{OM}\delta x(\omega) H\left(\omega, \Delta_0^{'}, |a_0|^2\right) \tag{2.13}$$

where

$$H\left(\omega, \Delta_0^{'}, |a_0|^2\right) = \left(\left[\frac{1}{\frac{\Gamma}{2} + i\left(\omega + \Delta_0^{'}\right)} - \frac{1}{\frac{\Gamma}{2} + i\left(\omega - \Delta_0^{'}\right)}\right]^{-1} - i|a_0|^2 \frac{d\omega}{dT}\frac{c_{th}^{-1}\Gamma_{abs}}{-i\omega + \gamma_{th}}\right)^{-1}. \tag{2.14}$$

Ultimately we are interested in the perturbations to Ω_m and Γ_m, which will need to be expressed as in-phase and quadrature driving terms in Eq. 2.8. In order to show this, we now force δx(t) and δa(t) to be harmonically oscillating functions at Ω_m, allowing us to write δx(ω) as 1/2 (δ(ω-Ω_m)+δ(ω+Ω_m)). Using this and separating the real and imaginary parts of H(Ω_m), we can rewrite Eq. 2.13 as

$$\begin{aligned} a_0\delta a^* + a_0^*\delta a = \frac{1}{2} g_{OM}|a_0|^2 \Big(& iR\left[H\left(\Omega_m\right)\right]\left(\delta\left(\omega - \Omega_m\right) - \delta\left(\omega + \Omega_m\right)\right) \\ & - I\left[H\left(\Omega_m\right)\right]\left(\delta\left(\omega - \Omega_m\right) + \delta\left(\omega + \Omega_m\right)\right)\Big), \end{aligned} \tag{2.15}$$

which in the time domain becomes

$$a_0\delta a^*(t) + a_0^*\delta a(t) = g_{OM}|a_0|^2 \left(\frac{R\left[H\left(\Omega_m\right)\right]}{\Omega_m}\delta\dot{x}(t) - I\left[H\left(\Omega_m\right)\right]\delta x(t)\right). \tag{2.16}$$

From here we plug Eq. 2.15 back into Eq. 2.11 and find

$$\begin{aligned}\delta T(\omega) = -\frac{c_{th}^{-1}\Gamma_{abs}|a_0|^2 g_{OM}}{\Omega_m^2+\gamma_{th}^2}\Bigg[\Big(&\gamma_{th}R\left[H(\Omega_m)\right]\\ &-\Omega_m I\left[H(\Omega_m)\right]\Big)\frac{\delta(\omega-\Omega_m)-\delta(\omega+\Omega_m)}{2i}\\ -\Big(&\Omega_m R\left[H(\Omega_m)\right]+\gamma_{th}I\left[H(\Omega_m)\right]\Big)\frac{\delta(\omega-\Omega_m)+\delta(\omega+\Omega_m)}{2}\Bigg],\end{aligned} \tag{2.17}$$

which in the time domain is

$$\begin{aligned}\delta T(\omega) = -\frac{c_{th}^{-1}\Gamma_{abs}|a_0|^2 g_{OM}}{\Omega_m^2+\ \gamma_{th}^2}\Bigg[&\delta\dot{x}(t)\,\frac{\gamma_{th}R\left[H(\Omega_m)\right]-\ \Omega_m I\left[H(\Omega_m)\right]}{\Omega_m}\\ &+\delta x(t)\ \ (\Omega_m R\left[H(\Omega_m)\right]+\gamma_{th}I\left[H(\Omega_m)\right])\Bigg].\end{aligned} \tag{2.18}$$

We can now go back to our original system of equations and linearize Eq. 2.8, finding

$$\frac{d^2}{dt^2}\delta x(t)+\Gamma_m\frac{d}{dt}\delta x(t)+\Omega_m^2\delta x(t) = -\frac{g_{OM}}{m_{eff}\omega_0}\left(a_0\delta a^*(t)+a_0^*\delta a(t)\right)+\frac{D}{m_{eff}}\delta T(t) \tag{2.19}$$

After plugging Eqs. 2.16 and 2.18 into the RHS of Eq. 2.19 it becomes clear that Eq. 2.19 can be rewritten as a simple driven harmonic oscillator with perturbations to Ω_m and Γ_m by grouping the terms on the RHS that contain δx $\dot{}$(the quadrature terms) with Γ_m and the terms that contain δx (the in-phase terms) with Ω_mˆ2. Doing this, we find that the system of equations involving thermal, optical, and mechanical dynamics

results in mechanical perturbations of the forms

$$\frac{\delta\Omega_m}{\Omega_m} = -\frac{|a|^2}{2K_m}\frac{g_{OM}}{L_{OM}}\ Im\left[H\left(\Omega_m\right)\right] - \frac{|a|^2}{2K_m}\frac{g_{OM}}{L_{PtM}}\ \left(\frac{\Omega_m}{\gamma_{th}}Re\left[H\left(\Omega_m\right)\right] + Im\left[H\left(\Omega_m\right)\right]\right) \tag{2.20}$$

$$\frac{\delta\Gamma_m}{\Omega_m} = \frac{|a|^2}{K_m}\frac{g_{OM}}{L_{OM}}Re\left[H\left(\Omega_m\right)\right] + \frac{|a|^2}{K_m}\frac{g_{OM}}{L_{PtM}}\left(Re\left[H\left(\Omega_m\right)\right] - \frac{\Omega_m}{\gamma_{th}}Im\left[H\left(\Omega_m\right)\right]\right) \tag{2.21}$$

We define $L_{PtM} \equiv \left[DC_{th}^{-1}\Gamma_{abs}\right]^{-1}(\Omega_m^2 + \gamma_t^2)/\gamma_t$ and $L_{OM} \equiv \omega_0/g_{OM}$, which can be physically understood as the inverse of the photo-thermal and optical forces per unit stored optical energy, respectively. From linearizing Eq. 2.7, we find that the circulating optical field can be expressed in terms of the incident power as $|a|^2 = \frac{\frac{\kappa_e}{2}|\epsilon|^2}{\frac{\kappa}{2}^2+\Delta_0'^2}$. Eqs. 18 and 19 are used to fit the data in shown in the main paper and the curves in Figure 2.9. We plot in Fig. 2.9 the Ω_m and Γ_m dynamics for the deflected down device at four different optical powers: 6 μW (red circles), 12 μW (orange circles), 20 μW (yellow circles), and 100 μW (blue circles).The best fit parameters reveal a photo-thermal force which scales linearly with power, and thus corresponds to linear absorption. However, the absorption rate Γ_{abs} seems to be larger than that expected from bulk silicon, most likely due to absorption from surface defects and surface adsorbents introduced during the fabrication process[50, 51], though it is difficult to decouple Γ_{abs} from D and thus know Γ_{abs} precisely. Measuring a set of devices before and after an annealing process seemed to confirm this, as both the mechanical quality factor and optical quality factor improved slightly after baking. We can find an upper bound on Γ_{abs} by finding the rate at which the thermal-optic effect (last term in Eq. 2.14) becomes notable, as our data reveals the effect to be quite small in our system. From this, we can estimate a value of the absorption quality factor: ($Q_{abs} = \omega_0/\Gamma_{abs} \approx 10^5$).

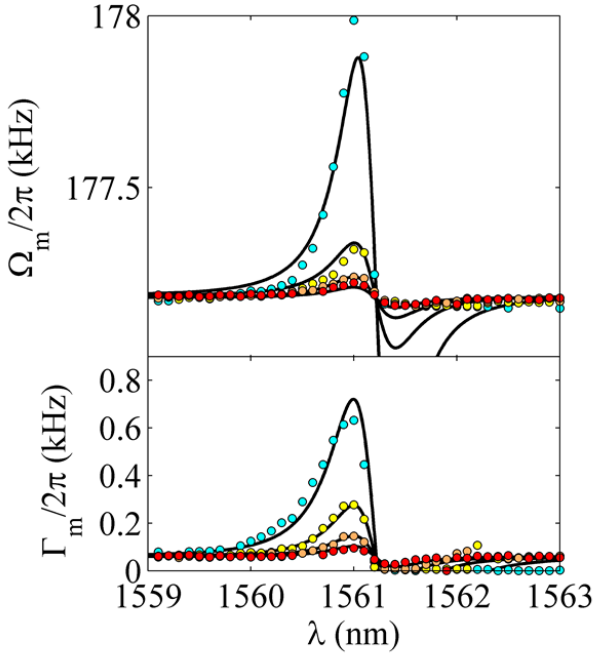

FIGURE 2.9: Mechanical frequency and linewidth at four different power levels (colors correspond to colors in Fig. 2.8(c)). The same fit parameters were used in all fitting curves, demonstrating a quality fit across multiple data sets and powers on the same device. Note that the fit to the photo-thermal-mechanical dynamics has linear power dependence, seen most clearly in the Γ_m dynamics (bottom panel) thus demonstrating the lack of two-photon absorption, which would have quadratic dependence.

2.1.7 Discussion and Conclusions

In summary, we have demonstrated a novel optomechanical platform based on a silicon photonic-crystal membrane suspended above an SOI substrate that exhibits a strong repulsive optical force. Using simple lithographic stress management techniques, we were able to control the membrane-substrate separation of our structures as well as their resulting optical and mechanical properties (e.g. resonance). The interplay between opto-mechanical and photo-thermal-mechanical effects was investigated, and both mechanical cooling and amplification have been demonstrated. Owing to its large size, our structure has many unique features including a large mass, ease of in- and out- coupling of light, and lack of two-photon absorption effects. Therefore, we believe that this structure is suitable for a range of applications. In addition to accelerometry and mass

sensing mentioned above, our devices can function as large-area liquid or gas-phase sensors, sensitive to refractive index changes of the environment.[52] The antibonding mode studied here is uniquely suited for this application, as the electric field distribution is extremely sensitive to the refractive index around the holes in the suspended membrane (Fig. 2.2(c)). Preliminary simulations in COMSOL Multiphysics indicate that the spectral sensitivity of the cavity resonance is $\approx$ 100 nm per refractive index unit, on par with previous values seen in similar geometries.[53] With control over both the optical and mechanical degrees of freedom, our membranes are good candidates for selective sensing technologies, where differences in mass and optical properties of analytes can be distinguished from one another and where the trade-off between large surface area and mechanical sensitivity can be tolerated.[54, 55]

Perhaps the most intriguing application of our platform is the investigation and control of the Casimir force. The Casimir effect causes two parallel surfaces separated by vacuum to be attracted to one another with a force proportional to s^{-4} and can cause failure in MEMS and NEMS systems. High, negative modes offer a method to counterbalance the Casimir and electrostatic pull-in forces that cause stiction. Additionally, the Casimir force can profoundly modify the mechanical dynamics of the system[56, 57] at separations of 100 nm or smaller, making this platform ideal for studying plate-plate Casimir dynamics. For example, the Casimir force acts as a nonlinear driving term to the mechanical oscillator, modifying Ω_m and introducing mechanical hysteresis, further improving the mass-sensing ability of the system by introducing bistability without the need for large oscillation amplitudes.[39] An integrated, tunable Casimir-mechanical oscillator is also desirable for testing of fundamental aspects of the Casimir effect, such as deviation from the proximity-force approximation[58, 59] for an arbitrarily structured surface.

While our platform has many potential applications, we note that this system has not been optimized for any one specific application, and the estimates presented here should not be taken as the limits of this new geometry. Most of the device parameters (Q_{opt}, Q_{mech}, g_{OM}) can be improved by modifications to the design and fabrication process[50, 51]. For instance, annealing of some devices at 500 C for 1 hour in a nitrogen environment improved Q_{opt} and Q_{mech} by about a factor of two. Actuation and sensing abilities both improve as the membrane-substrate separation decreases, leading to the possibility of low-power devices that can take advantage of the large area of the suspended membrane, such as optical accelerometers and combined mass and refractive-index sensors that are enhanced by the Casimir effect. By building these devices on silicon, we have opened up a new pathway for integration of novel optical components into MEMS and NEMS systems.

2.2 Optomechanical Hysteresis and Bistability

2.2.1 Overview

We demonstrate actuation of a silicon photonic crystal membrane with a repulsive optical gradient force. The extent of the static actuation is extracted by examining the optical bistability as a combination of the optomechanical, thermo-optic and photo-thermo-mechanical effects using coupled-mode theory. Device behavior is dominated by a repulsive optical force which results in displacements of > 1 nm/mW. By employing an extended guided resonance which effectively eliminates multi-photon thermal and electronic nonlinearities, our silicon-based device provides a simple, non-intrusive solution to extending the actuation range of MEMS devices.

2.2.2 Introduction

Rapid developments in the field of optomechanics have opened up avenues for fundamental research on quantum state manipulation with macroscopic structures [30] and show promise for novel optomechanical sensors [31] and technologies for both radio-frequency (RF) [60] and telecom applications.[61] While most attention has been devoted to compact structures featuring low (picogram) mass and ultrahigh-frequency (gigahertz) mechanical modes,[25, 26] the technological implication of static deformation due to optical forces has been less explored.[17] In coupled photonic waveguide geometries,[9, 62] bonding and anti-bonding optical modes are supported and the corresponding attractive and repulsive optical forces exerted on a pliant structure (low mechanical frequency) could serve to broaden the range of motion of integrated microelectromechanical devices. This translates to improvement in the detection range of pressure and displacement sensors and the actuation range of electrostatic actuators. In particular, the pull-in limit of electrostatic actuators could be extended by increasing the plate separation with a repulsive optical force. Additionally, novel schemes for preventing stiction, which occurs when attractive forces like the Casimir force and electrostatic force become overwhelmingly large compared to the mechanical restoring force, have been proposed [39] using a real-time monitoring of the structure's displacement and a counteracting feedback repulsive force (of the order of nano-Newtons and linear with excitation power). In this paper, we demonstrate nanometer-pulling of a thin silicon photonic crystal (PhC) membrane under high vacuum with a repulsive optical gradient force and an attractive photo-thermo-mechanical force. Furthermore, optical bistability induced by optical forces and thermo-optic effect is observed with large excitation powers while minimizing multi-photon nonlinearities.

2.2.3 Theory of Hysteresis and Bistability

Our devices – one of which is pictured in Fig. 2.10(a) and described in Fig. 2.10(b) – consist of a square silicon PhC slab suspended by four support arms ≈ 250 nm above a Silicon-on-Insulator (SOI) substrate. They are fabricated from a double-SOI platform, formed by oxide-oxide bonding of two thermally oxidized SOI wafers at atmospheric conditions. A sacrificial silicon dioxide layer between the two silicon layers is $s_0 = 265$ nm thick. Electron-beam lithography is performed on a layer of resist (ZEP-520A) to define the pattern. To combat the strong buckling of the silicon device layer by the compressive stress and upward turning moments of the oxide layer underneath, novel stress management techniques[41] were incorporated to obtain structures with lithographically determined membrane-substrate gaps. After developing, a fluorine-based reactive-ion etch is employed to transfer the patterns to the top silicon layer. The device is then released by undercutting the patterned silicon layer with the vapor-phase hydrofluoric acid etch. Finally, an annealing step was performed on at 500 C for 1 hour in a nitrogen environment to limit surface losses and maximize optical and mechanical quality factors. The height profiles of the released membranes from the substrate are characterized by a confocal microscope (Olympus LEXT OLS-4000).

The structure was designed to support an optical antibonding mode in the wavelength range of 1480-1680nm that results from the hybridization of waveguide modes in the membrane and substrate. The precise spectral location of the resonance is determined by the optomechanical coupling between the two modes, the strength of which is defined as $g_{OM} \equiv d\omega/ds$. The distribution of the x-component of the electric field in the top membrane is out-of-phase from that in the bottom membrane as pictured in Figure

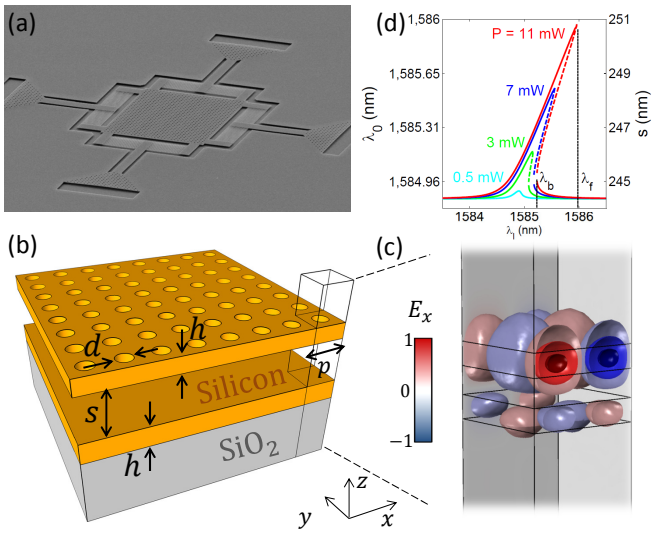

FIGURE 2.10: (a) Scanning Electron Microscope image of a device. (b) Schematic of membrane geometry consisting of a suspended silicon membrane above a silicon-on-insulator substrate. The top membrane is perforated by a 30×30 array of holes with diameter d = 0.414μm and period p= 0.92μm. Both silicon layers have thickness h = 185 nm. (c) 3D representation of the E_x field for the antibonding mode at $\lambda_0 = 1584.85$ nm in a single unit cell of the geometry. The solid color lines represent surfaces of equal field amplitude. (d) Calculated stable locations of the optical resonance as a function of laser wavelength, for four optical powers: 0.5 mW (cyan line), 3 mW (green line), 7 mW (blue line) and 11 mW (red line). At $P >= 3$ mW, the system has three solutions (two stable – solid line, one unstable – dashed line) for a certain range of wavelengths. Due to the intracavity-power dependence of optical detunings from optomechanical and thermo-optic effects, the system is bistable in this wavelength range, and displays hysteresis when the laser is swept continuously from short to long wavelengths (forward sweep) or vice versa (backward sweep). Two hysteretic transition points occur at λ_f for the forward sweep and λ_b for the backward sweep.

2.10(c), which corresponds to the generation of a repulsive gradient force. Additionally, the field symmetries along the x-z and y-z planes indicate that we are operating with a "dark" mode [40, 63], which theoretically does not couple to normally incident light because of mismatch in field symmetry. Optical dark modes exhibit high optical quality factors (Q_{opt}) and can be coupled into with normally incident light by breaking the periodicity of the full structure. Such devices have been the subject of numerous theoretical and experimental investigations on subjects ranging from the lowering of the laser thresholds [64] to increasing the sensitivity of photonic-crystal-based sensors [53]. Here, the dark mode is made accessible due to the finite size of the membrane and slight fabrication imperfection. The high Q_{opt} of the dark mode, together with the mode's

large optomechanical coupling coefficient $g_{OM} = 18$ GHz/nm, boosts the strength of the optical force and hence the range of actuation.

As previously described[39], the potential of a mechanical harmonic oscillator with equilibrium position s_0, when perturbed by the potential of an optical "spring" [65] centered at s_l for a laser wavelength λ_l can create a multiwell potential with two stable mechanical equilibria. The transition between these mechanical equilibria is reflected by the occurrence of optical bistability, due to the the dependence of the resonance frequency on s. Yet, the direct observation of the optomechanically-induced optical bistability can easily be obscured in actual systems by other competing mechanisms including thermo-optic effects, free-carrier dispersion and the Kerr nonlinearity [43]. While these effects have been actively pursued for realizing ultra-fast low-power optical switches and memory, such effects limit the the ability to take advantage of mechanical displacements. We designed our geometry to minimize these effects by exciting a guided resonance which is delocalized throughout the PhC membrane. We estimate the total mode volume to be $\approx 400(\lambda/n_g)^3$ from simulations of the whole superstructure performed in Lumerical. Due to its large modal volume, the thermal and electronic nonlinearities (which inversely scale with the modal volume) are dramatically reduced. This is in contrast with many of the optomechanical structures being studied, which have modal volumes $\approx (\lambda/n_g)^3$) and where thermal nonlinearities could be readily observed at even modest input powers. In our coupled PhC membrane, optomechanical detuning is larger than thermo-optic detuning even though our devices suffer from linear absorption due to defects introduced by fabrication processes, which is two orders of magnitude larger than the material absorption of silicon.

We can solve for the the optical and mechanical equilibria in the presence of the thermo-optic effect within the coupled-mode theory framework. We can find the stable solutions

by parameterizing the detuning Δ between the incident laser frequency ω_l and the resonance frequency. At an arbitrary value of Δ, we can calculate stored energy in the system $|a|^2$ as

$$|a|^2 = \frac{\kappa_e}{(\kappa/2)^2 + \Delta^2} P_{in} \tag{2.22}$$

where κ is the full-width half-max (FWHM) linewidth of the optical resonance, κ_e is the external coupling rate such that κ_e/k represents the fraction of incident power that gets coupled into the cavity, and P_{in} is the power incident on the structure. We use this to calculate the absorbed optical power and hence the temperature change of the system

$$\Delta T = \frac{\Gamma_{abs}|a|^2}{C_{th}\kappa_t} \tag{2.23}$$

where Γ_{abs} is the absorption coefficient of the system, C_{th} is the heat capacity, κ_t is the thermal diffusion rate, and the displacement of the membrane due to the respective photo-thermo-mechanical force and the repulsive gradient force

$$\Delta x = \frac{D\Delta T}{K} + \frac{|a|^2 g_{OM}}{\omega_l K} \tag{2.24}$$

where K is the spring constant of the mechanical resonator and D is the thermal-mechanical force coefficient in units of Newtons per Kelvin.[42] Both the temperature shift and mechanical displacement directly result in a change in the optical resonant frequency, such that we can express the expected change in the resonant frequency as $\Delta\omega_0 = g_{OM}\Delta x + (d\omega/dT)\Delta T$, where $d\omega/dT = (d\omega/dn)(dn/dT)$, n is the refractive index of silicon, $d\omega/dn$ is obtained from simulations and is equal to $-2\pi \times 5.05 \times 10^{13}$ Hz and

dn/dT is the thermo-optic coefficient of silicon, which is equal to $2 \times 10^{-4} K^{-1}$.[45] From here, we can find the steady state solutions by solving for where the parameter Δ is equal to the difference between the laser frequency and the perturbed optical resonance frequency $\omega_0' = \omega_0 + \Delta\omega_0$:

$$\Delta = \omega_l - \omega_0'. \tag{2.25}$$

The values of $\lambda_0' = 2\pi c/\omega_0'$ at which solutions of Eq. 2.25 exist are plotted in Fig. 2.10(d), as a function of laser wavelength $\lambda_l = 2\pi c/\omega_l$ for laser powers of 0.5 (cyan line), 3 (green line), 7 (blue line) and 11 mW (red line). The unperturbed optical resonance occurs at $\lambda_0 = 1584.85$ nm. The dashed portions of the curves correspond to unstable equilibria. At high powers, a clear bistable region exists in which there are two stable configurations of the membrane for fixed power and laser wavelength. The boundaries of the bistable region are denoted by λ_f and λ_b, representing the hysteretic transition wavelengths for a laser swept forward (left to right) and backward (right to left) across the resonance.

To investigate the hysteresis and bistability in our devices, we employ a free-space coupling setup described in Figure 2.11. A low power (60 μW) wavelength sweep is shown in the inset of Figure 2.11 (red curve), revealing a cavity resonance centered at $\lambda_0 = 1584.85$ nm. To account for interference fringes from parasitic reflections off of the vacuum chamber's window and other surfaces, we carefully fit both the optical resonance and the oscillating background (black line) to an expression which has the form[]

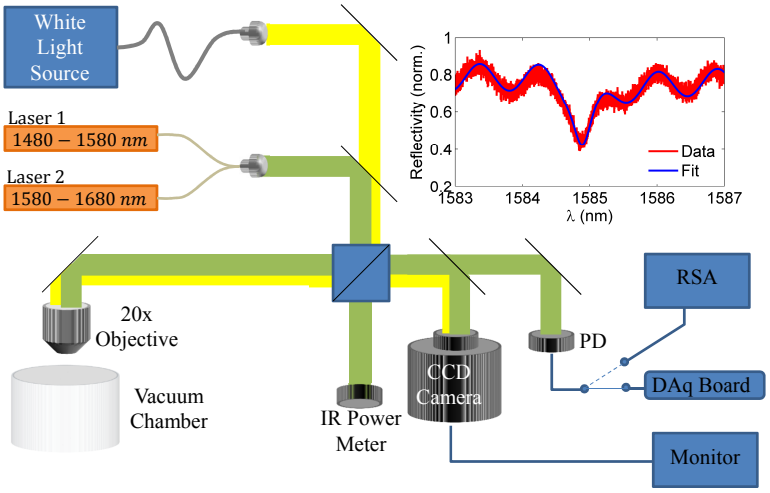

FIGURE 2.11: Free-space coupling setup. A white-light source and output from a near-IR laser are combined and sent through a 50-50 beam splitter, sending half of the signal to an IR power meter and half through a 20x objective placed above a vacuum chamber. The reflected signal is sent back through the beam splitter and can be directed onto a CCD camera allowing us to carefully align the laser spot to the membrane and to a photodetector (PD) to collect optical spectra via the DAq board and mechanical spectra via the real-time spectrum analyzer (RSA). Inset at right shows the reflection spectra of the device around the resonance centered at $\lambda_0 = 1584.85$ nm.

$$R = |r|^2 = \left| r_d(\lambda) e^{-i\phi} + \frac{\kappa_e}{-i\Delta_0' + \kappa/2} \right|^2 \tag{2.26}$$

where $r_d(\lambda)$ is the background reflectivity, and ϕ is the relative phase between the underlying background reflection and the optical cavity. Fitting parameters correspond to an optical cavity with $\kappa_e = 0.5\kappa$ and $Q_{opt}^{tot}\omega_0/\kappa = 4400$.

2.2.4 Freespace Mechanical Characterization

While the analysis in this section is primarily concerned with static dynamics of our membranes, this free space geometry is capable of producing extremely sensitive mechanical spectra. The fiber coupled geometry presented in Section 2.1 is comprised of almost entirely paraxial rays, which are collected at a small ($\approx 25\mu$m) distance from the

substrate, making the reflected intensity particularly insensitive to higher order, non-symmetric mechanical modes which would increase the angular spread of the reflected signal. This is tolerable, and perhaps even ideal, if we are only interested in dynamics surrounding the fundamental breathing mode of the structure, as we were earlier. However, higher order mechanical modes can be useful for studying the complex thermal dynamics of the membranes, as the amplitude of thermal-mechanical dynamics depends on the relative scales of the mechanical frequency and the thermal diffusion rate. When the mechanical frequency is much larger than the thermal diffusion rate, heat cannot diffuse away from the membrane over the course of one mechanical oscillation period, keeping the temperature oscillations fully in-phase with the amount of light contained in the optical cavity.

Mechanical resonance spectra of the first eighteen modes of the geometry are plotted in Figure 2.12. As expected, the fundamental mechanical mode has the largest spectral amplitude, 10 dBm larger than the next most prominent mode: the second-order breathing mode at $\Omega \approx 1.05$ MHz. Spectral peaks were matched to mechanical eigenmode profiles via simulations of the geometry performed in COMSOL Multiphysics, showing good agreement (within 5% on most modes with experiment. While we do not yet have the ability to directly address these higher order modes (i.e. we can only cool or amplify the fundamental mode due to the strong overlap between the optical mode and the mechanical mode), further study of this geometry or of a slightly modified geometry could permit excitation of these modes and a study of this geometry without influence of thermal dynamics.

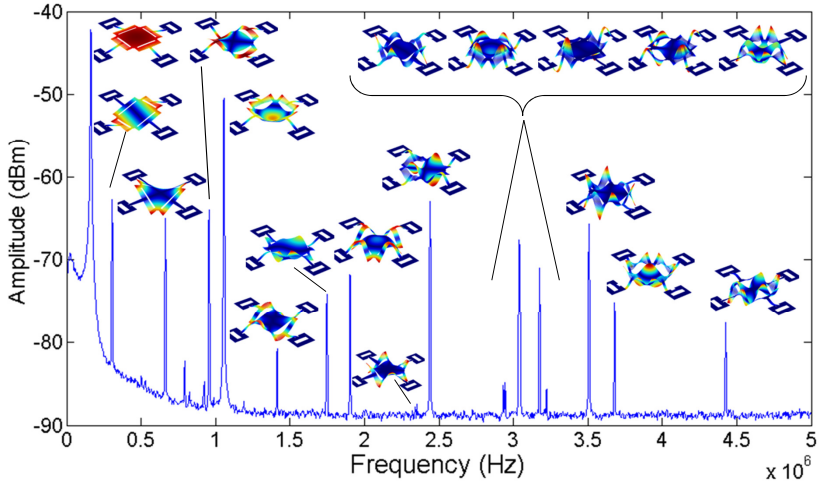

FIGURE 2.12: Mechanical resonance spectrum from 0 to 5 MHz. Measurements taken with the real-time spectrum analyzer reveal the first eighteen mechanical modes of the geometry, including the first five breathing modes at 180 kHz, 1.05 MHz and 1.9 MHz, 3 MHz and 3.75 MHz. In the fiber coupled setup, only the first two breathing modes were visible.

2.2.5 Results

Using these parameters, we can model the reflectance of the system as a function of laser wavelength at multiple powers (P = 0.04 to 6 mW), shown in Fig. 2.13(a) and offset for clarity, and compare the results to our experimental observations, shown in Fig. 2.13(b). The experimental data were collected by sweeping the tunable laser output from short to long wavelength (red curve) and then back (blue curve) at a fixed tuning speed of 1 nm/s. At 0.1 mW and higher, the mechanical resonator experiences regenerative oscillation when the laser wavelength is red-detuned ($\omega_l < \omega_0'$) from the optical resonance due to positive feedback between Brownian motion of the membrane at the membrane's fundamental mechanical resonance frequency Ω_m = 180 kHz and the thermal-mechanical force with a thermal diffusion rate $\gamma_t \approx 450kHz$, taken from simulations and careful fitting to optical and mechanical spectra. This can be seen in Fig. 2.13(b) as the thick red and blue sections of the curves, corresponding to periodic oscillation of the reflectance at Ω_m. Negative feedback between the membrane's motion

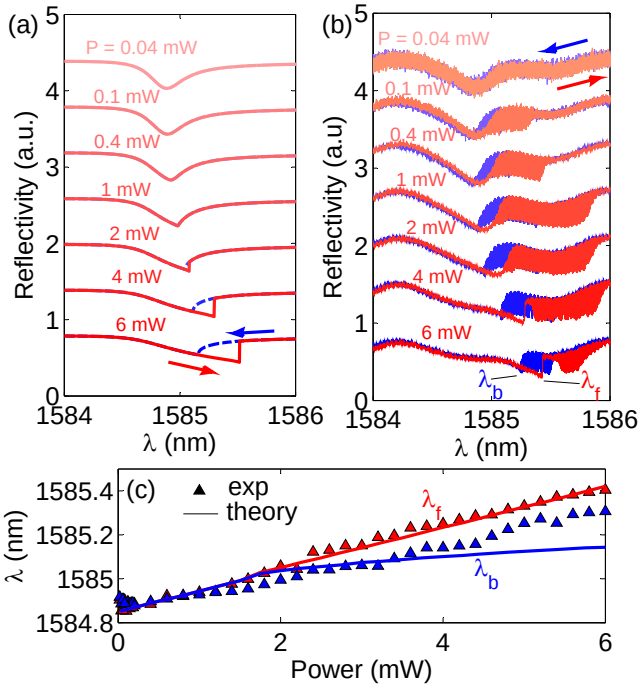

FIGURE 2.13: Theoretical (a) and experimental (b) reflection spectra for forward (red lines) and backward (blue lines) swept lasers from P =0.04 mW to 6 mW. Hysteresis is predicted to onset around 2 mW. (c) Locations of bistable transitions during forward and backward wavelength sweeps. The transition wavelength during the forward sweep λ_f (red triangles) is linear, and matches well to theory (red line). The backward transition wavelength (λ_b (blue triangles) predicts hysteresis at lower powers than theoretically predicted (blue line) and smaller hysteresis than expected at higher powers. Both of these discrepancies can be attributed to the static nature of the model, which does not take into account the effect of regenerative oscillations on hysteretic transitions.

and the photo-thermal-mechanical force occurs on the blue-detuned side of the resonance and works to damp the membrane oscillations in a process known as cooling [28, 66], allowing us to adequately treat the system as static at these detunings. While the optical spring effect and dynamic back-action have been thoroughly investigated in our system, this paper focuses on evaluating the static effect of the repulsive optical and photo-thermo-mechanical forces.

Abrupt transitions in the forward sweep direction occurring at λ_f can be seen in Fig. 2.13(b) for P = 4 and 6 mW, matching well with the transitions predicted by theory. The location of the backward transition at λ_b shows discrepancies with predictions, however, as the system appears to become bistable at lower powers than indicated by theory while

displaying a narrower bistable range than predicted at higher powers (Fig 2.13(c)). We believe that this discrepancy can be explained by the system's parametric instability. During the backward sweep, regenerative oscillation of the membrane supplies kinetic energy to the mechanical mode. When this mechanical energy is larger than the potential energy barrier separating the two stable equilibria, the system will jump into the second stable potential well. Upon doing so, the optical excitation abruptly becomes blue-detuned causing cooling of the motion of the membrane which is thus unable to recross the potential barrier. In effect this shrinks the bistable region, as it forces the backward transition to occur while the system is still bistable (i.e. before λ_l reaches λ_b). Alternately, we can investigate the range of actuation of the optical force by sweeping the *laser power* up and down at fixed wavelengths slightly red-detuned from the unperturbed cavity resonance. Theoretical predictions and experimental results are plotted in Fig. 2.14(a) and (b), respectively, showing the reflected power plotted against the incident laser power at six red detuned wavelengths: 1585 nm (cyan lines), 1585.1 nm (green lines), 1585.2 nm (blue lines), 1585.3 nm (red lines), and 1585.4 nm (magenta lines). The curves for the four longer wavelengths are each vertically offset from the $\lambda_l = 1585$ nm curves for clarity. For small detunings ($\lambda_l = 1585$ nm), the path traversed during an increase in input power from 0-10 mW (solid line) and a decrease in power (dashed line) coincide. At larger detunings, P_{out} experiences hysteresis. As the power is increased, the membrane enters the bistable region in the lower mechanical state and remains there until λ_b has redshifted such that $\lambda_b = \lambda_l$, at which point the membrane jumps to the upper curve. When decreasing the power, the membrane remains in the up-state until λ_f blueshifts back to λ_l, forcing the membrane to jump back down to the lower curve.

The agreement between theory and experiment in the upward and downward bistable

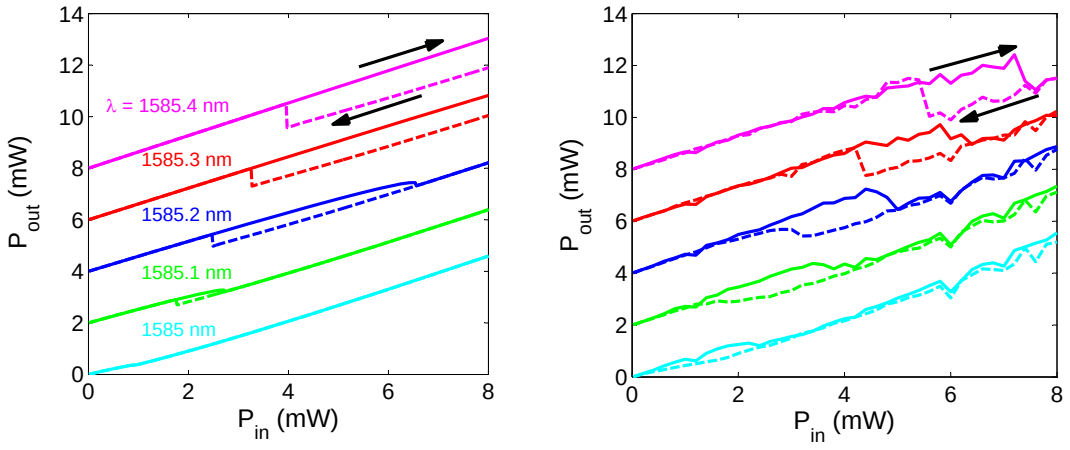

FIGURE 2.14: Predicted (a) and experimental (b) P_{in}-P_{out} curves of the device with the low power optical spectra seen in 2.10. Curves are plotted for five red-detuned wavelengths: $\lambda = 1585$ nm (cyan line), 1585.1 nm (green line), 1585.2 nm (blue line), 1585.3 nm (red line) and 1585.4 nm (magenta line). Solid lines represent the power output as a function of increasing laser power, while dashed lines represent power output as a function of decreasing input power. Modeling predicts hysteresis will occur at all wavelengths longer than 1585.1 nm. Some hysteresis is seen at 1581.1 nm experimentally, though this can be explained by the influence of dynamics on device behavior.

transitions is again affected by system dynamics as the bistable transitions also correspond to a jump between cooling and amplification. When the power is swept from high to low, λ_l goes from being blue detuned (in the bistable region) to being red-detuned, resulting in a cooling to amplification transition, with good agreement between theory and experiment. When the power is increased, the system goes from red-detuned to blue-detuned and from amplification to cooling, forcing the transition to occur at a lower power than predicted by theory. While both upward and downward transitions are visible in the data in Fig. 2.14(b) for all powers, only the downward transition is visible in Fig. 2.14(a) for $\lambda_l > 1585.1$ nm, as the upward transition occurs at $P > 8$ mW for these detunings, according to the theory.

When we decompose the perturbation to the optical resonance into its constituent parts, we find optomechanically-induced bistability to be the dominant effect. For example, at $P_{in} = 7$ mW, optomechanical effects correspond to a peak resonance shift $\Delta\lambda_{OM} = 0.5$

nm, while thermo-optic contributions lead to $\Delta\lambda_{PT} = 0.33$ nm and photo-thermal-mechanical contributions lead to $\Delta\lambda_{PTM} = 0.13$ nm. Furthermore, the membrane is mechanically pushed upward 4 nm by optomechanical effects and 1 nm downward by photo-thermal-mechanical effects, resulting in a net maximum displacement of 3 nm. These results hold promise for designing membranes which are less mechanically stiff and generate larger repulsive forces by increasing Q_{opt}. For instance, Q_{opt} is currently limited by fabrication imperfections and the finite size effect of the PhC and could be boosted by simply increasing the number of unit cells in the membrane [64]. To maintain the same compactness of the structure which is related to its dynamic range, the optical design could be modified with a smaller lattice constant and/ or graded hole modulation suggested by Srinivasan, et al.[67].

2.2.6 Conclusions

In conclusion, we demonstrated actuation of a micron-scale membrane with a repulsive optical force using an extended guided resonance in a coupled silicon PhC membrane. The net red-shift displayed in the optical resonance of our doubly-bonded SOI platform is a result of an optomechanically-induced red-shift, a thermo-optic red-shift, and a photo-thermo-mechanically induced blue-shift. Furthermore, simulations indicate that absorption in our system is dominated by surface defects and adsorbents, resulting in a linear absorption coefficient two orders of magnitude larger than that expected from bulk silicon. By minimizing these effects through fabrication process and design modifications, we can further isolate and exploit the unique optomechanical properties of this platform. Since multi-photon nonlinearities do not occur until the excitation power exceeds ≈ 1 W, the extent of pulling of the PhC membrane can be many tens

of nanometers. Our silicon-based device provides a simple, non-intrusive solution to extending the actuation range of MEMS devices.

Chapter 3

Surface Plasmons

3.1 Surface Plasmon Waveguide Forces

3.1.1 Overview

We analytically investigate the forces due to Surface Plasmon Polariton (SPP) modes between finite and infinitely thick metal slabs separated by an air gap. Using the Drude model and experimentally determined values of the dielectric functions of gold and silver, we study how frequency dispersion and loss in the metals affects the behavior of the SPP modes and the forces generated by them. We calculate the force using the Maxwell Stress Tensor for both the attractive and repulsive modes.

3.1.2 Introduction

Recent applications for harnessing the energy of light has explored the nature of radiation pressure in high Q-factor microresonators [10, 68], negative index systems [69, 70],

metamaterials [71], photonic crystals [72] and in dispersive dielectrics [70, 73, 74]. Additionally, studies have explored the evanescent wave bonding and antibonding between parallel dielectric optical waveguides [9, 12] and microresonators [37] and the enhancement of radiation pressure in waveguides due to slow-light effects [75].

Surface Plasmon Polaritons (SPPs) offer another avenue for generating mechanical motion from light [76]. SPPs are the result of coherent coupling of photons to free electron oscillations at the boundary between a metal and a dielectric. A significant amount of work has been devoted to studying the coupling of SPPs on surfaces that are in close proximity to one another [77, 78]. Long Range Surface Plasmon Polaritons (LRSPPs) [79–81], which result from the coupling of SPPs on opposite surfaces of a thin – on the order of the skin depth – metal slab in what is known as the Insulator-Metal-Insulator geometry (IMI), can propagate for distances up to 1 cm when excited at near-infrared frequencies [82]. SPP-induced field enhancement in gaps between metallic nanoparticles [83, 84] and between large planar surfaces in the Metal-Insulator-Metal (MIM) geometry [85–87] have been used for Surface Enhanced Raman Spectroscopy (SERS) [88–90] and the creation of nanoantennas [91].

The forces on metal and dielectric nanoparticles generated by SPP excitation on planar metal surfaces have previously been studied [92–96]. Progress has also been made on the nature of SPP forces in metal nanoparticle clusters [62, 97–100], though to our knowledge, no work thus far has addressed the forces between planar metal surfaces. In this paper we analytically investigate the forces generated by SPPs in the two-dimensional MIM and Insulator-Metal-Insulator-Metal-Insulator (IMIMI) geometries in the cases involving both "lossless" and lossy metals.

This chapter is structured as follows: in section 3.1.3, we derive the expressions for the

dispersion of the SPP modes in idealized metal-dielectric systems. We compare the SPP dispersion using the Drude model for the dielectric function of the metal to the SPP dispersion calculated with the tabulated dielectric data of silver and gold from Palik [101]. In section 3.1.4, we calculate the forces in the IMIMI geometries, and in section 3.1.5, we discuss the characteristics of the force curves the and applications of SPP waveguide forces.

3.1.3 Calculation of the Dispersion of SPP Waveguides

SPPs are transverse magnetic (TM) polarized modes that exist at the interface of two materials when the real part of the electric permittivity, $\epsilon(\omega)$, changes sign across the interface. The most common example of such a system is the boundary between a metal and a dielectric at optical frequencies. The field profile of an SPP at an interface is a solution of the wave equation, $\left(\nabla^2 - [\mu\epsilon(\omega)]^{-1}\partial^2/\partial t^2\right)\mathbf{E}(\mathbf{r},t) = 0$, where μ is the magnetic permeability and is equal to the permeability of free space, μ_0, for nonmagnetic materials at optical frequencies, and $\mathbf{E}(\mathbf{r},t)$ is the electric field. When $\epsilon(\omega)$ changes sign across an interface, the continuity of the normal component of the displacement vector, $\mathbf{D}(\mathbf{r},t)$, implies a solution with evanescent fields on both sides of the interface.

Using the coordinate system of Fig. 3.1, we express the electric field as $\mathbf{E}(\mathbf{r},t) = \mathbf{E}_0\exp(i\mathbf{k}\cdot\mathbf{r} - i\omega t)$, where $\mathbf{k} = k_0 n\hat{\mathbf{r}} = k_z\hat{\mathbf{z}} + \kappa\hat{\mathbf{y}}$ is the wavevector of SPPs, $-\hat{\mathbf{z}}$ is the direction of propagation and

$$k_0^2 n^2 = k_z^2 + \kappa^2. \tag{3.1}$$

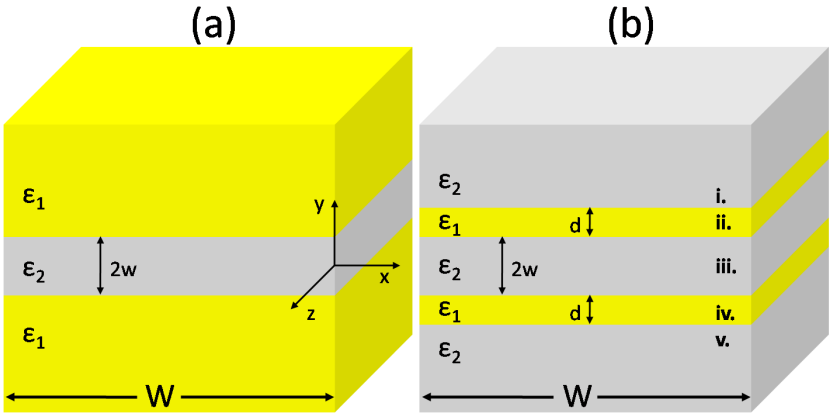

FIGURE 3.1: The Metal-Insulator-Metal (MIM, (a)) and Insulator-Metal-Insulator-Metal-Insulator (IMIMI, (b)) geometries. ϵ_1 is the electrical permittivity of the metal and ϵ_2 is the permittivity of the dielectric. The roman numerals in the IMIMI geometry correspond to the regions defined in Eq. 3.3. In both geometries, the origin is placed at the center of the dielectric gap of width $2w$, and SPP propagation is in the -z-direction in the calculations.

In Eq. (3.1), $k_0 = \omega/c$, n is the refractive index of the medium, k_z is wavevector in the direction of SPP propagation, which is conserved across the interface. We can write k_z as $\beta + i\alpha$, where β is the propagation constant and α is the loss factor. $\mathrm{Im}\{\kappa\} > \mathrm{Re}\{\kappa\}$ for SPPs. For convenience, we define $k_y \equiv i\kappa$ so that for SPPs we can rewrite Eq. (3.1) as

$$k_0^2 n^2 = k_z^2 - k_y^2. \tag{3.2}$$

Using these conventions, we can calculate the field profiles for SPPs supported in the two geometries shown in Fig. 3.1. The subscripts 1 and 2 will always be used to denote the metallic and dielectric regions, respectively in the equations throughout this paper, as labeled in Fig. 3.1.

The SPP fields in the IMIMI geometry can be expressed by the following set of equations:

$$H_x(y,z,t) = \begin{cases} \mathcal{A}\exp(-k_{y2}y) & \textbf{i. } y > d+w \\ \mathcal{B}\exp(-k_{y1}y) + \mathcal{C}\exp(k_{y1}y) & \textbf{ii. } w < y < d+w \\ \mathcal{D}\exp(-k_{y2}y) + \mathcal{F}\exp(k_{y2}y) & \textbf{iii. } -w < y < w \\ \mathcal{G}\exp(-k_{y1}y) + \mathcal{H}\exp(k_{y1}y) & \textbf{iv. } -(d+w) < y < -w \\ \mathcal{J}\exp(k_{y2}y) & \textbf{v. } y < -(d+w) \end{cases} \tag{3.3}$$

$$E_y(y,z,t) = -\frac{k_z}{\omega\epsilon} H_x(y,z,t) \tag{3.4}$$

$$E_z(y,z,t) = \frac{1}{i\omega\epsilon}\frac{\partial}{\partial y} H_x(y,z,t) \tag{3.5}$$

where $\mathcal{A}\ldots\mathcal{J}$ are the field amplitudes which satisfy the boundary conditions for the fields, k_{y1}, k_{y2} are the y-components of the k-vectors in the two materials, and the factor $\exp[-i(\omega t + k_z z)]$ has been dropped from the expressions for clarity. The equations for the MIM geometry are obtained by taking $d \to \infty$.

At interfaces between nonmagnetic materials, E_z and H_x are continuous. Because of the symmetry of the IMIMI structure, there are two independent solutions which satisfy its boundary conditions: one corresponding to $\mathcal{D} = \mathcal{F}$ and one to $\mathcal{D} = -\mathcal{F}$. We chose to define the overall mode symmetry in terms of the parallel electric field component, E_z, which matches the symmetry of the charge distribution in the structure. Thus, $\mathcal{D} = -\mathcal{F}$ corresponds to symmetric modes and $\mathcal{D} = \mathcal{F}$ corresponds to antisymmetric modes. Solving the system defined by Eq. (3.3)-(3.5) and the boundary conditions for the antisymmetric modes, we find the following relation:

$$\frac{k_{y2}\epsilon_1}{k_{y1}\epsilon_2}\tanh(k_{y2}w) = -\left[\frac{\frac{k_{y1}}{\epsilon_1}\sinh(k_{y1}d) + \frac{k_{y2}}{\epsilon_2}\cosh(k_{y1}d)}{\frac{k_{y1}}{\epsilon_1}\cosh(k_{y1}d) + \frac{k_{y2}}{\epsilon_2}\sinh(k_{y1}d)}\right]. \tag{3.6}$$

When combined with Eq (3.2) for each of the two media, Eq. (3.6) gives a transcendental equation for the dispersion, $\omega(k_z)$. The dispersion relation for the symmetric modes is given by replacing $\tanh(k_{y2}w)$ with $\coth(k_{y2}w)$ in the left hand side of Eq. (3.6). We find that Eq. (3.6) and its symmetric counterpart each give rise to two fundamental solutions corresponding to a SPP mode.

These four IMIMI geometry modes – two symmetric and two antisymmetric – represent the couplings between the four metal-dielectric interfaces in the geometry. To understand these modes, it is helpful to treat the geometry as coupled IMI SPP waveguides, as shown in Fig. 3.2. The E_z field profiles of the two LRSPP modes (Fig. 3.2(a)) are antisymmetric with respect to the center of the metal slabs, and can couple together symmetrically (Fig. 3.2(b)) and antisymmetrically (Fig. 3.2(c)). We refer to these modes as $\mathbf{S}_a$ and $\mathbf{A}_a$, respectively, where the capital character denotes the overall symmetry of the mode and the subscript corresponds to the symmetry of the constituent IMI waveguide modes.

IMI waveguides also support Short Range Surface Plasmon Polaritons (SRSPP), which have shorter propagation lengths due to a larger mode overlap with the metal slabs and have symmetric E_z field profiles with respect to the center of the metal slab (Fig 3.2(d)). Two SRSPP waveguide modes will couple symmetrically (Fig. 3.2(e)) and antisymmetrically (Fig. 3.2(f)). These modes are referred to as $\mathbf{S}_s$ and $\mathbf{A}_s$, respectively.

In the MIM limit ($d \to \infty$), $\mathbf{S}_s$ and $\mathbf{S}_a$ are degenerate, so only one symmetric mode exists (Fig. 3.2(g)). We refer to it here as $\mathbf{S}_0$, where the subscript 0 implies this degeneracy. Similarly, the MIM geometry supports only one antisymmetric mode, $\mathbf{A}_0$ (Fig. 3.2(h)). At this point, we can use the field symmetry to find the sign of the force generated by each of our modes. Since a symmetric mode corresponds to symmetric charge oscillations,

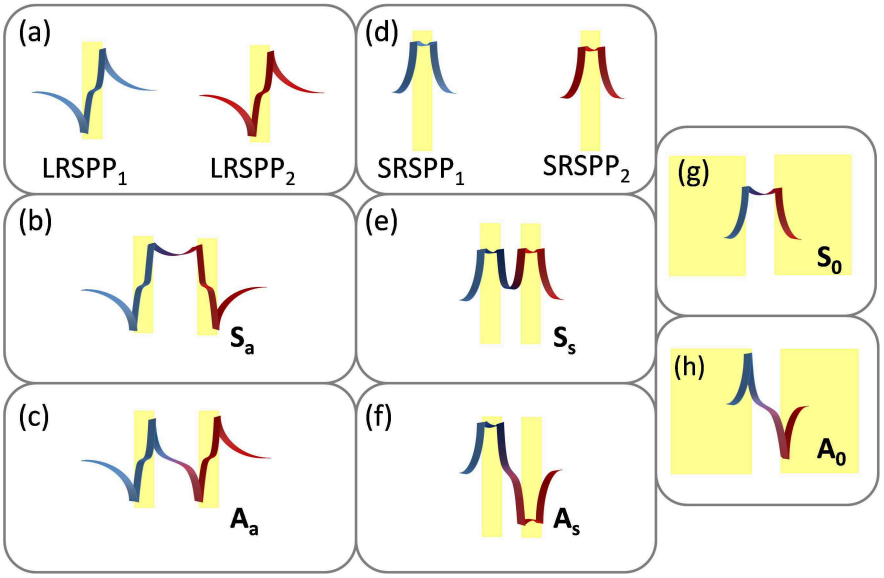

FIGURE 3.2: E_z field shapes and naming conventions for the modes supported by the IMIMI and MIM geometries. (a) shows two isolated IMI stripe waveguides each supporting a Long-Range Surface Plasmon Polariton (LRSPP) mode. When these waveguides are brought in proximity to one another, $LRSPP_1$ and $LRSPP_2$ will couple symmetrically (b) and antisymmetrically (c). The symmetric Short Range Surface Plasmon Polariton (SRSPP) modes supported by the IMI waveguide (d) will also couple symmetrically (e) and antisymmetrically (f). The MIM geometry supports only two modes, known here as $\mathbf{S}_0$ (g) and $\mathbf{A}_0$ (h).

we expect modes with symmetric profiles to generate repulsive forces between the slabs. Likewise, we expect the antisymmetric modes to be attractive.

In the limit of $d \to \infty$, the right hand side of Eq. (3.6) equals -1, yielding the transcendental MIM dispersion relation. It is worth noting that by taking both d and $w \to \infty$, the single planar surface plasmon dispersion relation, $\beta = (\omega/c)\mathrm{Re}[\sqrt{\epsilon_1\epsilon_2/(\epsilon_1+\epsilon_2)}]$, is recovered.

In order to solve the dispersion relation, we need to model the dielectric function of the meal and the insulator. By letting the insulator be air, we can set $\epsilon_2 = \epsilon_0$. The simplest model for the metal is the Drude model, which allows us to write the dielectric function as:

$$\frac{\epsilon_1(\omega)}{\epsilon_0} = 1 - \frac{\omega_p^2}{\omega^2 + \gamma^2} + i\frac{\omega_p^2 \gamma}{\omega(\gamma^2 + \omega^2)}. \tag{3.7}$$

The Drude model treats a metal as a damped free electron gas where $\omega_p = 2\pi\nu_p = \sqrt{Ne^2/\epsilon_0 m_0}$ is the plasma frequency and $\gamma = Ne^2/\sigma_0 m_0$ is the damping coefficient. In these expressions, N is the density of free electrons in the metal, e is the electron charge, m_0 is the electron mass and σ_0 is the DC conductivity of the metal. The damping coefficient, γ, is very small compared to ω_p for lightly damped systems like noble metals. We find that we can simplify things further by ignoring the loss and taking only the real part of Eq. (3.7), maintaining the key characteristics of the model and noting that below ω_p, $\epsilon'' \ll \epsilon'$. By substituting the real part of Eq. (3.7) into Eq. (3.6), we solve for the dispersion relations of the modes described in Fig. 3.2, and plot $\beta(\omega)$ in Fig. 3.3 for both the MIM and the IMIMI geometries, for gap widths of 25 nm and 100 nm.

The $\mathbf{S}_0$ mode (cyan lines, Fig. 3.3(a) and (c)) exhibits a cutoff and does not exist at optical frequencies for values of w of interest to us, i.e., $w < \pi/\beta$, where π/β is equal to half of the SPP wavelength. For this reason it will not be discussed in this paper. The $\mathbf{A}_0$ mode wavevector (red lines) increases asymptotically toward a cutoff frequency, $\nu_p/\sqrt{2} = \omega_p/\sqrt{8\pi^2} = 1.54 \times 10^{15}$ Hz for both gap widths plotted, though it approaches the asymptote more quickly for larger gap widths.

Figure 3.3(b) and 3.3(d) show the frequency dispersion of the two symmetric modes – $\mathbf{S}_s$ (blue lines) and $\mathbf{S}_a$ (cyan lines) – and the two antisymmetric modes – $\mathbf{A}_s$ (red lines) and $\mathbf{A}_a$ (green lines) – for gap widths of $2w = 30$ nm and $2w = 100$ nm, respectively, and a slab thickness of 20 nm in the IMIMI geometry. Comparing Fig. 3.3(b) to Fig. 3.3(a) reveals that the IMIMI $\mathbf{S}_a$ and $\mathbf{A}_s$ modes have dispersive properties similar to those

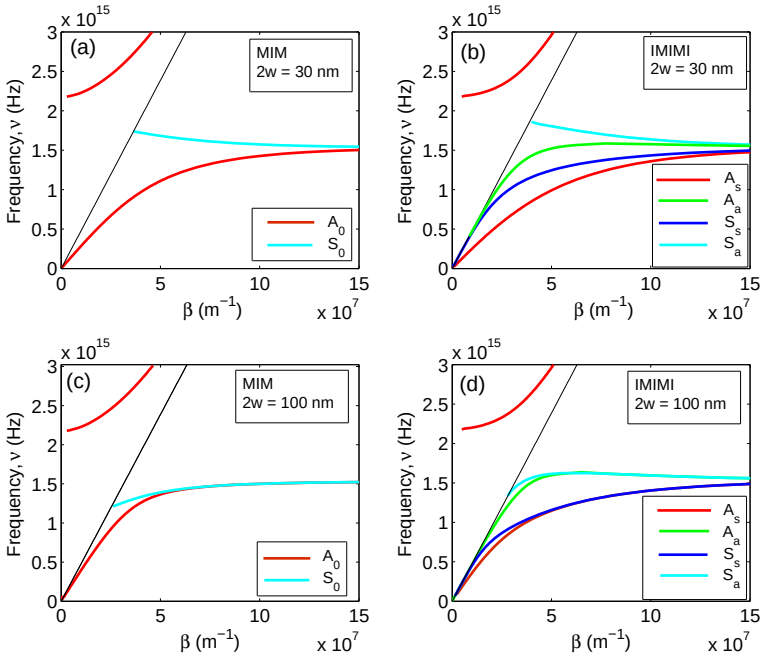

FIGURE 3.3: Drude Plasmon dispersion for the MIM ((a) and (c)) and IMIMI ((b) and (d)) geometries for gap widths, $2w$, of 30 nm (a) and (b) and 100 nm (c) and (d), respectively, modeled with the plasma frequency and damping coefficient for gold: $\omega_p = 1.37\times10^{16}\,\mathrm{s}^{-1}$ ($\nu_p = \omega_p/2\pi$) and $\gamma = 3.68\times10^{13}\,\mathrm{s}^{-1}$. The values for silver do not differ from these values enough to produce plots that are distinguishable from those shown here. The thicknesses of the metal slabs in the IMIMI geometry are held constant at 20 nm.

of the MIM $\mathbf{S}_0$ and $\mathbf{A}_0$ modes, respectively, particularly at small gap widths. For this reason we will also not discuss $\mathbf{S}_a$ in this paper. $\mathbf{A}_s$ and the remaining IMIMI modes all approach the $\nu_p/\sqrt{2}$ asymptote. $\mathbf{A}_a$ exhibits the least dispersion at low frequencies, as evidenced by the fact that below 10^{15} Hz, the wavevector remains close to the light line.

As the gap width increases, we see that the $\mathbf{A}_a$ and $\mathbf{S}_a$ modes and the $\mathbf{A}_s$ and $\mathbf{S}_s$ modes each approach degeneracy (Fig. 3.3(c) & (d)). At large gap widths, the interaction of the SPPs between the two slabs weakens, so the remaining two degenerate modes are those of the IMI LRSPP and SRSPP.

The bulk plasmon appears in red in all four panels of Fig. 3.3 above the light line ($\beta > \omega/c$) and above the plasma frequency ($\nu_p = 2.18\times10^{15}$Hz), where metals experience ultraviolet transparency.

Figure 3.4 shows the dispersion relations for the MIM (3.4(a),(c)) and IMIMI (3.4(b),(d)) geometries modeled with the tabulated date for gold from Ref. [101], and Fig. 3.5 shows the same modes modeled with the tabulated dielectric functions for silver (also from Ref. [101]), for the same two gap widths depicted in Fig. 3.3. The data in Ref. [101] is compiled from multiple researchers and from samples fabricated under different conditions. The slight bump in the dispersion curves for SPPs on silver slabs (Fig. 3.5) around 7×10^{14}Hz is due to a change in the data set tabulated by Palik, and is not due to an actual physical characteristic of silver. The dielectric function – particularly the imaginary part – of amorphous, polycrystalline and single crystal metals will be notably different from one another, with a variance of up to 20% [102], so it is important to realize that this tabulated data will not precisely match the actual dielectric function of a fabricated metal film.

We note that in both of these figures, we have only plotted the $\mathbf{A}_0$ mode in the MIM geometry (red lines, panels (a) and (c)) and the $\mathbf{A}_s$ (red lines, panels (b) and (d)) and $\mathbf{S}_s$ (blue lines, panels (b) and (d)) modes in the IMIMI geometry. Once again, the MIM $\mathbf{S}_0$ and the IMIMI $\mathbf{S}_a$ modes do not exist at optical frequencies for these gap widths and the IMIMI $\mathbf{A}_a$ mode has such weak dispersion that the force generated by it will be at least an order of magnitude smaller than the $\mathbf{A}_s$ and $\mathbf{S}_S$ modes. We have also included the Drude model dispersion (gray dots) for the two modes in both figures for comparison.

Figure 3.4 shows that the Drude model is an excellent approximation for gold below $4{\times}10^{14}$ Hz ($\lambda_0 \approx 750\,\mathrm{nm}$), but becomes increasingly worse above that frequency. The reason is that the free electron model for a metal does not account for interband absorption, which begins for gold around the aforementioned frequency, and for silver around 6e14 Hz ($\lambda_0 \approx 500\,\mathrm{nm}$). When absorption increases to the point that $\epsilon''(\nu) = \epsilon'(\nu)$, the

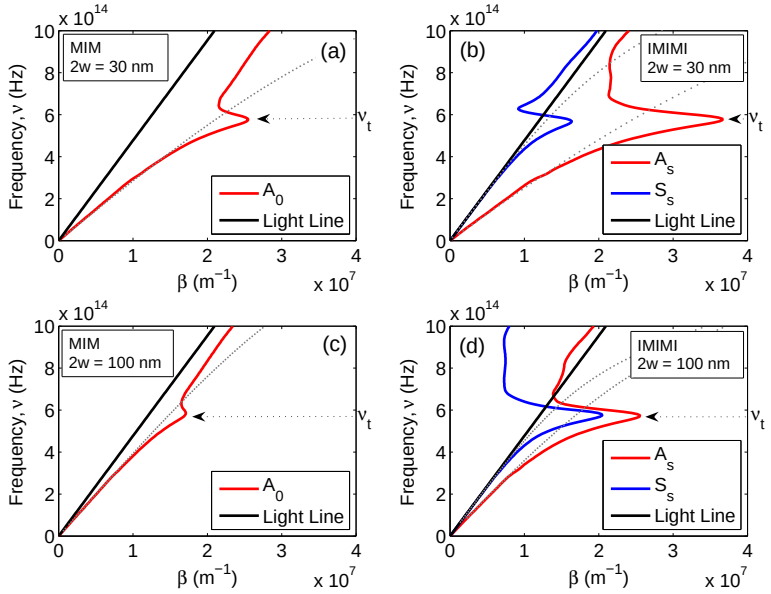

FIGURE 3.4: SPP Dispersion for the MIM $\mathbf{A}_0$ (red lines (a), (c)) and IMIMI $\mathbf{A}_s$ (red lines, (b), (d)), and $\mathbf{S}_s$ (blue lines, (b), (d)) modes for gap widths of 30 nm (a) and (b) and 100 nm (c) and (d), respectively, modeled with the dielectric data for gold, taken from Ref. [101]. Grey dots represent the modes calculated with the Drude model. The thicknesses of the metal slabs are held constant at 20 nm.

SPP mode switches from having normal dispersion to having anomalous dispersion. We refer to this frequency, where $d\beta/d\nu = \infty$, as the turnaround frequency, ν_t, which for gold is approximately $\approx 6{\times}10^{14}$ Hz. For silver, $\nu_t \approx 9{\times}10^{14}$ Hz.

In both the MIM and IMIMI geometries, the analysis of the modes in Fig. 3.3 for Drude metals applies to gold and silver. The $\mathbf{A}_0$ wavevector between the slabs is larger below ν_t when the gap width is small (Fig. 3.4(a), Fig 3.5(a)) than when it is large (Fig. 3.4(c), Fig3.5(c)). In the IMIMI geometry, as the frequency increases toward ν_t, the wavevectors of both modes become significantly larger than predicted by the Drude model. However, they still behave in the same way. The $\mathbf{S}_s$ wavevector at a given frequency decreases as the gap width decreases, while the $\mathbf{A}_s$ wavevector increases. While gold is more dispersive than silver below $\nu \approx 6{\times}10^{14}$Hz, silver exhibits significant dispersion between $\nu_{t,Au}$ and $\nu_{t,Ag}$. Extremely large wavevectors are achievable in small-gap width (Fig. 3.4(a),(c)) silver-insulator plasmonic structures. In the IMIMI geometry, both $\mathbf{A}_s$ and

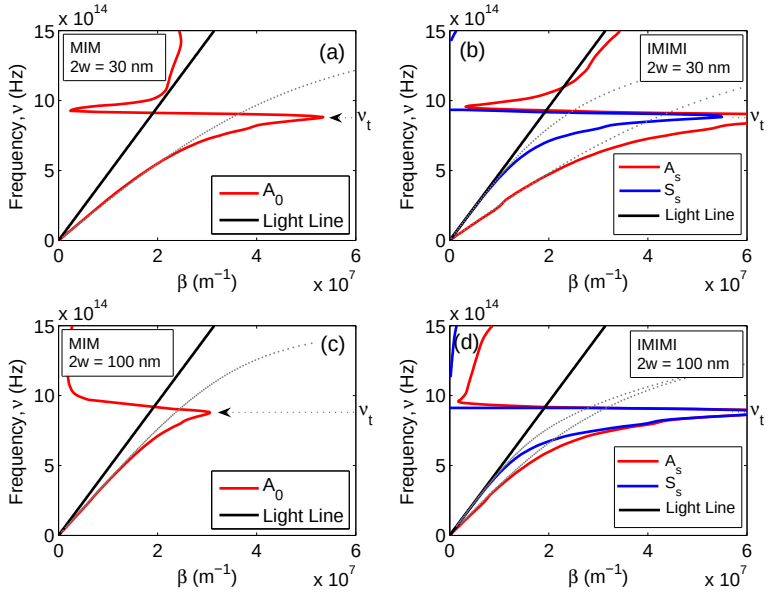

FIGURE 3.5: SPP Dispersion for the MIM $\mathbf{A}_0$ (red lines, (a), (c)) and IMIMI $\mathbf{A}_s$ (red lines, (b), (d)) and $\mathbf{S}_s$ (blue lines, (b), (d)) modes for gap widths of 30 nm (a) and (b) and 100 nm (c) and (d), respectively, modeled with the dielectric data for silver, taken from Ref. [101]. Grey dots represents the modes calculated using the Drude model. The thicknesses of the metal slabs in the IMIMI geometry are held constant at 20 nm.

$\mathbf{S}_s$ are extremely dispersive beneath ν_t at small and large gap widths, while once again, these modes approach degeneracy at large gap widths (Fig. 3.4(d), Fig. 3.5(d)).

Figure 3.6 further illustrates this point. The wavevectors of the three modes are plotted using the Drude model and the Palik data for gold and silver as a function of gap width, $\beta(2w)$, at a freespace wavelength of $\lambda_0 = 600\,\text{nm}$. The effective mode index, $n_{eff} = \beta c/\omega$, is plotted along the right y-axis.

The wavevectors for the MIM $\mathbf{A}_0$ mode (Fig. 3.6(a)) calculated using the different models differ only slightly, with the wavevector calculated with Palik's data for gold being predictably larger due to the proximity of the operating frequency to ν_t. By contrast, the IMIMI $\mathbf{A}_s$ wavevector (Fig. 3.6(b)) calculated with Palik's gold data is significantly larger than the wavevectors calculated with the Drude mode and Palik's data for silver. Comparing (a) to (b), however, reveals that $\mathbf{A}_s$ behaves like $\mathbf{A}_0$, especially when dispersion and loss are low, as is true for silver and Drude metals at $\lambda_0 = 600\,\text{nm}$. The

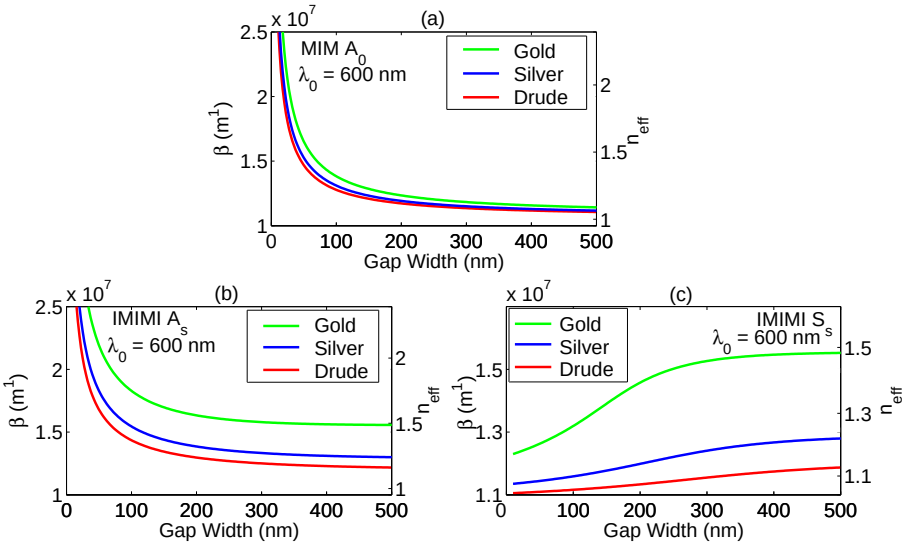

FIGURE 3.6: SPP Wavevectors for the MIM $\mathbf{A}_0$ (a) and IMIMI $\mathbf{A}_s$ (b) and $\mathbf{S}_s$ (c) modes for as the gap width is varied, modeled with the dielectric data for gold (green lines) silver (blue lines), taken from Ref. [101], and the Drude model (red lines). The thickness of the metal slabs in the IMIMI geometry is 20 nm.

similarity of these modes implies that the $\mathbf{A}_s$ mode represents a strong coupling between the inner surfaces of the thin metal slabs of the IMIMI geometry, and that the mode's behavior is only weakly dependent on the thickness of the slabs.

Independent of the metal model, the wavevector of these two modes increases exponentially, meaning the group velocity, $v_g = c(n_{eff} + \omega \mathrm{d}n_{eff}/\mathrm{d}\omega)^{-1}$, decreases exponentially as the gap width between the slabs decreases. Thus these two modes, for extremely small gap widths, can generate slow light, as well as the enhanced field "hot spots" at optical frequencies that has been described in previous MIM waveguide studies [86–89].

The $\mathbf{S}_s$ wavevector (Fig. 3.6(c)) decreases as the gap width decreases for all dielectric models of the metal. This behavior, in contrast to that of the antisymmetric modes, is asymptotic, not exponential. The wavevector, β, is largest between two gold slabs due to the proximity of the operating frequency to ν_t. As the gap width approaches zero, the $\mathbf{S}_s$ wavevector approaches the value of an IMI SRSPP waveguide of thickness $2d$, implying that this mode corresponds to a depletion of optical energy from in between

the two slabs, in contrast to the enhancement from the antisymmetric modes. We will discuss this further in section 4 when we analyze the energy profiles of the modes. We can also see clearly that at large gap widths – approaching the region of weak coupling between the two gold slabs – the $\mathbf{A}_s$ and $\mathbf{S}_s$ wavevectors approach the same value – the value of the SRSPP wavevector in the IMI waveguide geometry.

3.1.4 Calculations of SPP Forces in the MIM and IMIMI Geometries

With the values of the SPP wavevectors obtained with Eqs. (3.2)-(3.6) (and plotted in Figs. 3.3-3.6), we can solve for $\mathcal{A}, \mathcal{B}, \mathcal{C}, \mathcal{F}, \mathcal{G}, \mathcal{H}$ and $\mathcal{J}$ in terms of $\mathcal{D}$. By taking advantage of the symmetry of the geometry, we know that $\mathcal{F} = \pm\mathcal{D}$, $\mathcal{G} = \pm\mathcal{C}$, $\mathcal{H} = \pm\mathcal{B}$, $\mathcal{J} = \pm\mathcal{A}$, where the '+' solutions correspond to the antisymmetric modes and the '−' solutions correspond to the symmetric modes. The antisymmetric solutions have the following amplitudes:

$$\mathcal{A} = 2\mathcal{D}\frac{\frac{k_{y1}}{\epsilon_1}\cosh(k_{y2}w)}{\frac{k_{y1}}{\epsilon_1}\cosh(k_{y1}d) + \frac{k_{y2}}{\epsilon_2}\sinh(k_{y1}d)}\exp\left(k_{y2}[w+d]\right) \tag{3.8}$$

$$\mathcal{B} = \mathcal{D}\frac{\cosh(k_{y2}w)\left(\frac{k_{y1}}{\epsilon_1} + \frac{k_{y2}}{\epsilon_2}\right)}{\frac{k_{y1}}{\epsilon_1}\cosh(k_{y1}d) + \frac{k_{y2}}{\epsilon_2}\sinh(k_{y1}d)}\exp\left(-k_{y1}[w+d]\right) \tag{3.9}$$

$$\mathcal{C} = \mathcal{D}\frac{\cosh(k_{y2}\mathrm{w})\left(\frac{k_{y1}}{\epsilon_1} - \frac{k_{y2}}{\epsilon_2}\right)}{\frac{k_{y1}}{\epsilon_1}\cosh(k_{y1}d) + \frac{k_{y2}}{\epsilon_2}\sinh(k_{y1}d)}\exp\left(k_{y1}[w+d]\right). \tag{3.10}$$

The symmetric solutions can be obtained by replacing $\cosh(k_{y2}w)$ with $\sinh(k_{y2}w)$ in Eqs. (3.8)-(3.10).

We can relate the field amplitudes for each of the modes to the power flowing in them along the z-axis:

$$P_z = \mathrm{Re}\left\{ \iint \mathbf{S} \cdot \hat{z} \mathrm{d}x\mathrm{d}y \right\} \tag{3.11}$$

where $\mathbf{S} = (1/2)\mathbf{E} \times \mathbf{H}^*$ is the Poynting vector for complex fields and * denotes the complex conjugate. We can rewrite Eq. (3.11) as the power per unit waveguide width (see Fig. 3.1) using the relationship between E_y and H_x expressed in Eq. (3.4) as

$$\mathcal{P} = \frac{P_z}{W} = \mathrm{Re}\left\{ \frac{k_z}{\omega\epsilon} \right\} \int_0^\infty |H_x|^2 \mathrm{d}y, \tag{3.12}$$

then solve Eq. (3.12) for $|\mathcal{D}^2|$ in terms of $\mathcal{P}$:

$$\begin{aligned} |\mathcal{D}|^2 = \omega\mathcal{P} \times \\ \left\{ \frac{\beta}{\epsilon_2} \left[\frac{|\bar{\mathcal{A}}|^2 \exp\left(-2k'_{y2}[w+d]\right)}{2k'_{y2}} + \frac{\sinh\left(2k'_{y2}t\right)}{k'_{y2}} \pm \frac{\sin\left(2k''_{y2}t\right)}{k''_{y2}} \right] \right. \\ + \quad \frac{\beta\epsilon'_1 + \alpha\epsilon''_1}{|\epsilon_1|^2} \quad \times \\ \left[\left(\frac{|\bar{\mathcal{B}}|^2 \exp\left(-k'_{y1}[2w+d]\right)}{k'_{y1}} + \frac{|\bar{\mathcal{C}}|^2 \exp\left(k'_{y1}[2w+d]\right)}{k'_{y1}} \right) \sinh\left(k'_{y1}d\right) \right. \\ \left. \left. + \frac{2\mathrm{Re}\{\bar{\mathcal{B}}\bar{\mathcal{C}}^* \exp[-ik''_{y1}(2\mathrm{w}+d)]\}}{k''_{y1}} \sin(k''_{y1}d) \right] \right\}^{-1} \end{aligned} \tag{3.13}$$

where $\bar{\mathcal{X}} \equiv \mathcal{X}/\mathcal{D}$ for $\mathcal{X} = \mathcal{A}, \mathcal{B}, \mathcal{C}$. Additionally, $k_{yj} \equiv k'_{yj} + ik''_{yj}$, and $\epsilon_j \equiv \epsilon'_j + i\epsilon''_j$ where $j = 1, 2$, and '$\pm$' corresponds to the antisymmetric and symmetric mode solutions, respectively. We will hold $\mathcal{P}$ constant at 1 mW/μm throughout this paper.

With the field amplitudes in terms of power, we can solve for the force using the Maxwell Stress Tensor (MST). Starting with microscopic Maxwell's Equations, we can calculate the macroscopic dielectric properties of our system by representing the materials as an ensemble of dipole resonators and taking the average of response. From this, a statement of conservation of momentum can be obtained [74, 103]:

$$\int_A \overleftrightarrow{T}(\mathbf{r},t)\cdot\mathbf{n}(\mathbf{r})\,\mathrm{d}a = \frac{d}{dt}\int_V \frac{(\mathbf{E}\times\mathbf{H})}{c^2}\mathrm{d}^3\mathbf{r} + \int_V \left[(\rho - \mathbf{P}\cdot\nabla)\,\mathbf{E} + \left(\mathbf{J} + \frac{\partial\mathbf{P}}{\partial t}\right)\times\mathbf{B}\right]\mathrm{d}^3\mathbf{r}, \tag{3.14}$$

where

$$\overleftrightarrow{T} = \left[\epsilon_0\mathbf{E}\mathbf{E} + \mu_0\mathbf{H}\mathbf{H} - \frac{1}{2}\left(\epsilon_0\left|\mathbf{E}\cdot\mathbf{E}\right| + \mu_0\left|\mathbf{H}\cdot\mathbf{H}\right|\right)\overleftrightarrow{\mathbf{I}}\right] \tag{3.15}$$

is the MST, $\mathbf{E}\mathbf{E}$ represents the outer product of the two vectors, $\mathbf{P}$ is the polarization vector, with $\mathbf{D} = \epsilon_0\mathbf{E} + \mathbf{P}$, $\leftrightarrow$ denotes a second rank tensor and $\overleftrightarrow{\mathbf{I}}$ is the identity tensor. The first term on the right hand side of Eq. 3.14 can be expressed in terms of the momentum of the electromagnetic field, $\mathbf{G}_{\text{field}}$, as

$$\frac{d}{dt}\int_V \frac{1}{c^2}(\mathbf{E}\times\mathbf{H})\,\mathrm{d}^3\mathbf{r} = \frac{d\mathbf{G}_{\text{field}}}{dt}, \tag{3.16}$$

which is equal to zero when averaged over one period of oscillation. The second term on the right hand side of Eq. 3.14 represents the mechanical force, and in a sourceless geometry ($\rho = 0, \mathbf{J} = 0$) is written as:

$$\langle \mathbf{F} \rangle = \left\langle \frac{\mathrm{d}\mathbf{G}_{\mathrm{mech}}}{\mathrm{d}t} \right\rangle = \int_V \left\langle \left(-\mathbf{P}\cdot\nabla\right)\mathbf{E} + \left(\frac{\partial \mathbf{P}}{\partial t}\right)\times\mathbf{B} \right\rangle \mathrm{d}^3\mathbf{r}, \tag{3.17}$$

where $\langle \dots \rangle$ denotes the time average. We can see from this equation that the force can be expressed in terms of the local, oscillating charges and currents that result from the polarizability of the material. However, since we do not care about the distribution of the force density throughout our volume, we can use the left hand side of Eq. 3.14 to find the force in the y-direction, between the metal slabs. We can write the force for the symmetric mode as

$$\langle \mathbf{F}_y \rangle = \frac{\mu_0}{2}\left(1 - |n_{eff}|^2\right)|\mathcal{D}|^2, \tag{3.18}$$

and the antisymmetric mode forces as

$$\langle \mathbf{F}_y \rangle = \frac{\mu_0}{2}\left(\left|\frac{ck_{y2}}{\omega}\right|^2\right)|\mathcal{D}|^2, \tag{3.19}$$

where Eq. 3.19 becomes the negative of Eq. 3.18 in the lossless limit. Previous work [9, 75] showed that one could equivalently calculate the force between dielectric waveguides by taking the spatial gradient of the electromagnetic energy:

$$F = -\left.\frac{\mathrm{d}U}{\mathrm{d}w}\right|_{k_z}, \tag{3.20}$$

where $U = N\hbar\omega$ and N is the photon density in the mode, and the derivative is taken at constant wavevector, k_z, due to translational invariance of the modes. This method is not accurate in plasmonic systems for two reasons. First, translational invariance along

the direction of propagation as well as conservation of the adiabatic invariant U/ω, which is proportional to N, cannot be assumed any longer due to optical losses. Secondly, a change in ω and the corresponding change in $\epsilon(\omega)$ will lead to a shift in k_z, making Eq. 3.20 nonphysical. Therefore, we must rely on the Stress Tensor to calculate forces.

The forces generated by the $\mathbf{A}_s$ and $\mathbf{S}_s$ modes in the IMIMI geometry are plotted in Fig. 3.11(a) and (b) for the freespace wavelength $\lambda_0 = 600$nm. We plot the force between 20nm thick gold (green lines), silver (blue lines) and Drude metal (red lines) slabs. In Fig. 3.11(c) and (d), we plot the $\mathbf{A}_s$ and $\mathbf{S}_s$ mode forces between silver slabs at three freespace wavelengths: $\lambda_0 = 450\,\text{nm}$ (cyan lines), $\lambda_0 = 600\,\text{nm}$ (blue lines), and $\lambda_0 = 1000\,\text{nm}$ (magenta lines). We plot the force in units of $\text{pN}/\mu\text{m}^2$ and note that $1\,\text{pN}/\mu\text{m}^2 = 1\,\text{Pa}$. We note that the modes in (a) and (b) of this figure correspond directly to the modes plotted in Fig. 3.6 (b) and (c). Additionally, we have only plotted the magnitudes of the forces, noting that the $\mathbf{S}_s$ mode is repulsive and the $\mathbf{A}_s$ mode is attractive.

There are two distinct coupling regimes for the two modes. The first, at large gap widths, is characterized by weak mode coupling and weak forces. The magnitudes of the forces generated by both the $\mathbf{A}_s$ and $\mathbf{S}_s$ modes in this regime are identical, as seen by comparing the force curves in Fig. 3.11(a) to those in Fig. 3.11(b) and the curves in Fig. 3.11(c) to those in Fig. 3.11(d). The gap width at which the forces generated by the $\mathbf{A}_s$ and $\mathbf{S}_s$ modes are no longer identical is on the order of 1μm.

The gap width at which the attractive and repulsive modes begin to behave differently depends on the penetration depth of the mode in the dielectric, $\delta_2 = 1/k_{y2}$, for large w. This value is directly related to the point where the SRSPP modes on the two slabs begin to overlap with each other. At $\lambda_0 = 600$nm (Fig. 3.11(a) and (b)), δ_2 is largest

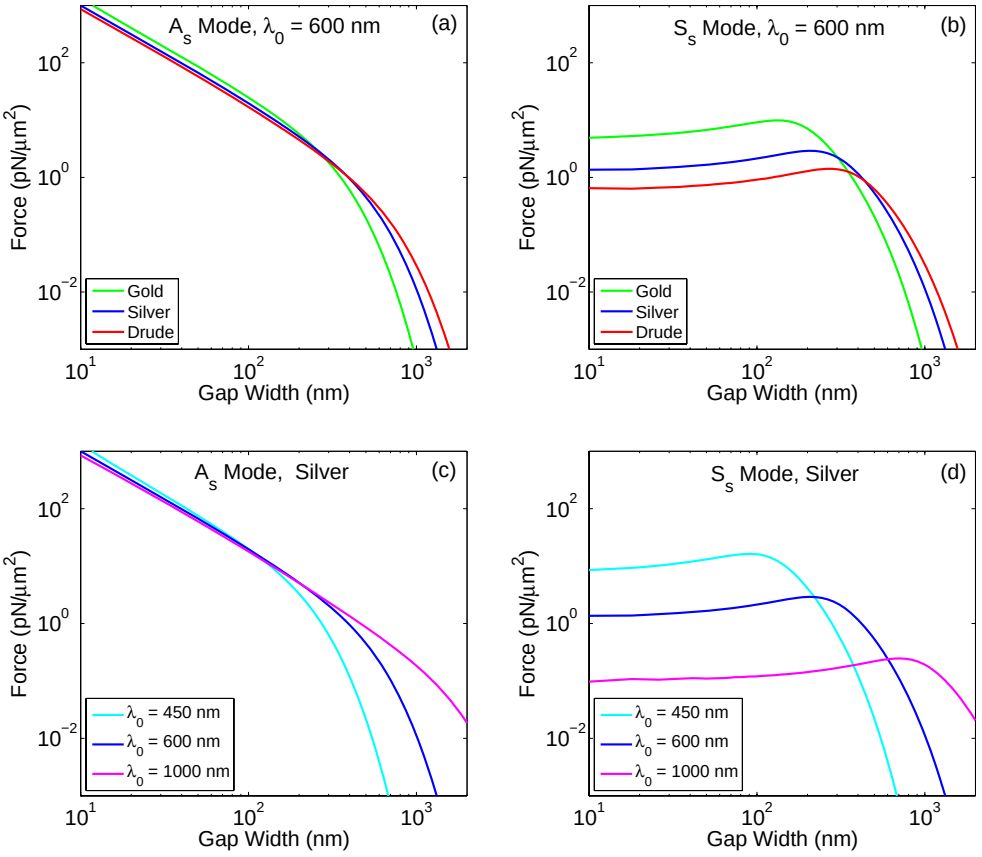

FIGURE 3.7: (a) and (b): The force from the SPP modes in the IMIMI geometry, calculated using three models for the metal: tabulated data for gold (green lines) and silver (blue lines), and the Drude Model (red lines) at an operating wavelength of $\lambda_0 = 600\,\text{nm}$. Plotted in (a) is the magnitude of the attractive $\mathbf{A}_s$ mode force, while the repulsive $\mathbf{S}_s$ mode force is plotted in (b). (c) and (d): The $\mathbf{A}_s$ and $\mathbf{S}_s$ mode forces between silver slabs at $\lambda_0 = 450\,\text{nm}$ (cyan lines), $\lambda_0 = 600\,\text{nm}$ (blue lines), $\lambda_0 = 1000\,\text{nm}$ (magenta lines). The MIM $\mathbf{A}_0$ mode behaves like the IMIMI $\mathbf{A}_s$ mode, and so is not plotted here.

for Drude metal slabs and smallest for gold slabs. For silver slabs (Fig. 3.11(c) and (d)), δ_2 is largest at $\lambda_0 = 1000$nm and smallest at $\lambda_0 = 450$nm. In both of these cases, δ_2 is largest when the operating frequency is closest to the turnaround frequency of the metal, ν_t. This agrees with what we would expect by looking at Eq. 3.2, where we can see that δ_2 should vary inversely with β. We can also see that the force in this regime at a given gap width is stronger when δ_2 is larger.

The second coupling regime is at small gap widths, where the coupling between the two slabs is strong and the attractive and repulsive modes behave quite differently. The

force generated by the attractive, $\mathbf{A}_s$, mode increases exponentially, but at a slower rate than when the coupling was weak. The strength of the $\mathbf{A}_s$ mode force is only weakly dependent on the dielectric function (Fig. 3.11(a)) and the freespace wavelength (Fig. 3.11(a)), with the stronger force occurring when the wavevector, β, is largest.

The force generated by the repulsive, $\mathbf{S}_s$, mode peaks at the boundary between weak and strong coupling and decreases as the slabs are brought closer together. At $\lambda_0 = 600$nm (Fig. 3.11(b)), the force peak is highest for gold and smallest for Drude metals. For silver slabs (Fig. 3.11(d)), the force peak is highest at $\lambda_0 = 450$nm and smallest at $\lambda_0 = 1000$nm. The peak is highest when β is largest, which occurs at frequencies closest to ν_t for the metal being used.

The strength of the repulsive force in the strong coupling regime corresponds directly to the change that the wavevector undergoes as the gap width changes, as shown in Fig. 3.6(c). As the gap width $2w \to 0$, the wavevector asymptotically approaches the value corresponding to a geometry where the two metal slabs are in contact, effectively creating an IMI structure with a metal thickness $2d = 40$nm. For silver and Drude metals, the change in wavevector β is small, but it is significantly larger for gold slabs at $\lambda_0 = 600$nm.

3.1.5 Discussion and Conclusions

To understand the difference between in behavior of the $\mathbf{A}_s$ and $\mathbf{S}_s$ modes more concretely, it is helpful to look at how the distribution of energy changes in the mode as the gap width changes. The electromagnetic energy density in a linear, dispersive material has been thoroughly discussed theoretically [7, 104, 105] and can be expressed as

$$u(\mathbf{r}) = \frac{1}{4}\epsilon' \left(1 + \frac{\omega}{\epsilon'}\frac{\mathrm{d}\epsilon'}{\mathrm{d}\omega}\right) \left[\mathbf{E}\left(\mathbf{r}, t\right) \cdot \mathbf{E}^{*}\left(\mathbf{r}, \mathbf{t}\right)\right] + \frac{1}{4}\mu_0 \left[\mathbf{H}\left(\mathbf{r}, t\right) \cdot \mathbf{H}^{*}\left(\mathbf{r}, \mathbf{t}\right)\right]. \tag{3.21}$$

We can solve this equation in the metal region using the Drude model and in the dielectric region where dispersion is negligible ($\mathrm{d}\epsilon'/\mathrm{d}\omega = 0$) for the two modes at an operating wavelength ($\lambda_0 = 450\,\mathrm{nm}$) and plot the cross-sections for a range of gap widths in Fig. 3.8. We choose Drude metal slabs in Fig. 3.8 because they most clearly illustrate the key features of the energy distribution within the modes. This analysis applies independent of the metal or frequency, however, as long as it is below ν_t. The energy density inside the metal slabs is plotted as having negative value for clarity.

Figure 3.8(a) shows the energy cross-sections for the $\mathbf{A}_s$ mode and Fig. 3.8(b) shows the cross-section for the $\mathbf{S}_s$ mode. Note that the colormaps in the two panels are not of the same scale. At large gap widths, the SPPs on the two metal slabs are essentially uncoupled. The value of the energy density at the inner and outer surface of each metal slabs is approximately equal for both modes, displaying little mode overlap and little interaction between the two modes on the IMI waveguides.

At small separations, the strong coupling across all four metal-dielectric interfaces is evident. In Fig. 3.8(a), as the gap width decreases below 100 nm, the energy density in the $\mathbf{A}_s$ becomes concentrated in the space between the slabs, and becomes more than an order of magnitude larger than the energy density outside the slabs. This redistribution of energy, from outside to inside the slabs, is due to the antisymmetric surface charge distribution across the gap, and explains the attractive nature of the $\mathbf{A}_s$ mode. Additionally, the amount of energy carried in the metal increases at small gap widths, corresponding to the higher n_{eff} and β seen in Fig. 3.6(b).

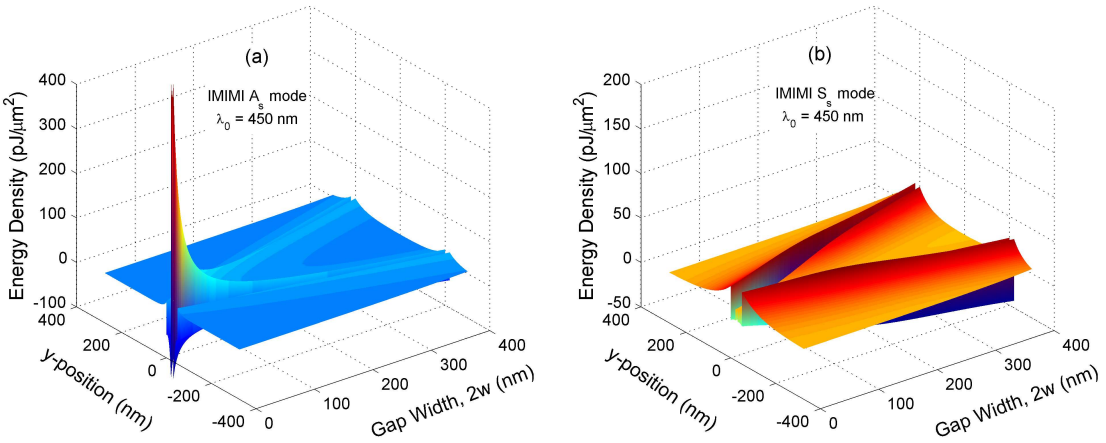

FIGURE 3.8: IMIMI energy density cross-sections at $\lambda_0 = 450$nm for geometries using Drude metals. The plots show the energy density of the modes for gap widths between 10 and 400 nm. In (a), the cross-sections for the $\mathbf{A}_s$ mode. In (b), the cross-sections for the $\mathbf{S}_s$ mode. Note that the colormaps in the two panels are not of the same scale.

Conversely, the energy density of the $\mathbf{S}_s$ mode (Fig. 3.8(b) decreases to zero as the gap width decreases, while the amount of energy outside of the slabs increases. This redistribution is due to the symmetric surface plasmon charge oscillations across the gap, and corresponds to the repulsive nature of this mode. Furthermore, the energy carried in the metal slabs simultaneously decreases, resulting in the smaller n_{eff} and β seen in Fig. 3.6(c).

Nanomechanical forces will play important roles in future devices, both as an avenue for discovery and as a hindrance. SPPs offer an on-chip, optical, solution, to actuation and detection of motion in a nanomechanical resonator, for charge and mass sensing and switching applications. Furthermore, at the length scales relevant to optical forces, one will also have to contend with the Casimir force. For comparison, the Casimir force – $-\hbar c\pi^2/3840\mathrm{w}^4$ – between parallel ideal metal plates separated by 100 nm is $13\,\mathrm{pN}/\mu\mathrm{m}^2$ and decreases to $\approx 5.5\,\mathrm{pN}/\mu\mathrm{m}^2$ between two 20 nm thick gold slabs. This value is only slightly smaller than the optical forces presented here at the power level assumed in this paper. We can imagine a system, however, where we can control the power level of our

excitation source, and selectively excite the repulsive $\mathbf{S}_s$ mode to cancel out the attractive Casimir interaction. The ability to generate a net-neutral interaction between supported metallic nanostructures offers new directions for preventing stiction in nanomechanical devices.

We have shown detailed calculations of the dispersion of SPP modes in two geometries: Metal-Insulator-Metal and Insulator-Metal-Insulator-Metal-Insulator. We have treated the metals using the Drude model and with tabulated data for silver and gold from Ref. [101]. From the wavevector dispersion, we have calculated the field profiles, energy, and forces for the modes of these two geometries. Because of the significant dispersion of gold at green-to-red visible frequencies, SPP mode forces are significantly larger than seen with the Drude model and the tabulated data for silver. While the MIM geometry supports attractive forces, the IMIMI geometry support modes with both attractive and repulsive characteristics, making it potentially desirable for many nanomechanical applications.

3.2 Spoof Surface Plasmon Forces

3.2.1 Overview

Spoof surface plasmon (SSPs) are surface plasmon-like waves that propagate along metal surfaces with deeply sub-wavelength corrugations and whose dispersive properties are determined primarily by the corrugation dimensions. Two parallel corrugated surfaces separated by a sub-wavelength dielectric gap create a "spoof" analog of the plasmonic metal-insulator-metal (MIM) waveguide. These structures, dubbed "spoof-insulator-spoof" (SIS) waveguides, allow for the extension of plasmonic waveguiding concepts

beyond visible and near-infrared (IR) frequencies and into the mid-IR and terahertz frequency ranges, where light is harder to confine. Here, we study the attractive and repulsive forces generated by the propagating "bonding" and "anti-bonding" waveguide modes of the SIS geometry, respectively, and the role that surface structuring plays in controlling the modal properties. By changing the depth of the grooves, strong attractive and repulsive optical forces between the surfaces can be generated at nearly any frequency, paving the way for a new class of on-chip mid-IR and terhertz optomechanical devices.

3.2.2 Spoof Plasmon Dispersion

Surface plasmons (SPs) are the result of the coupling between photons and free electron oscillations in a metal at its interface with a dielectric and have been extensively studied over the past decade [106, 107]. SPs in metal-insulator-metal (MIM) waveguides can lead to extreme sub-wavelength confinement [89], strong field enhancement [86], and even negative refraction [108, 109]. Additionally, the field of active plasmonics has seen significant growth in recent years as researchers have attempted to integrate plasmonic elements into micro- and nano-electromechanical systems (MEMS and NEMS) for applications including optical circuitry[110], ultrafast optical switching [111], and optomechanics [112]. However, these studies have been limited almost entirely to the visible and near-infrared (IR) frequency ranges where materials like gold, silver, and transparent conducting oxides have strong plasmonic resonances [113, 114] but are also highly lossy. Subwavelength corrugations on the surfaces of metals allow for the extension of these concepts to lower frequencies where absorption losses can be much smaller [115–118]. Corrugated surfaces support SP-like waves known as spoof surface plasmon

(SSPs), which are TM-polarized waves whose behavior depends primarily on the geometry of the corrugations instead of the optical properties of the metal. The dispersion equation for SSPs on a corrugated perfect electric conductor (PEC) has been analytically calculated [116] as

$$\frac{\kappa_z^g}{k_0} = \frac{a}{d}\tan\left(k_0\sqrt{\epsilon_d}h\right) \tag{3.22}$$

where $k_0 = 2\pi/\lambda_0$, λ_0 is the free space wavelength, ϵ_d is the dielectric function of the bounding dielectric, set here to 1 to represent air, $\kappa_z^g = ik_z^g = \sqrt{\beta^2 - k_0^2\epsilon_d}$, β is the propagation constant, and h, d and a are defined in Figure 3.9(a) with $d << \lambda_0$. The solution to Eq. 3.22 is shown in Figure 3.9(b) for $h = 2$ μm, $d = 0.5$ μm, and $a/d = (0.002, 0.2, 0.4, 0.6, 0.8, 0.98)$ (dark to light green lines). The single SSP dispersion curve is formed by the "anticrossing" of the dispersion curve of a plane wave propagating along the corrugated surface and the curve corresponding to a localized $\lambda/4$ cavity resonance of a single corrugation at the so-called spoof surface plasmon frequency (wavelength), $\omega_{ssp,0} = \pi c/2h$ ($\lambda_{spp,0} = 4h$). Thus the SSP can be thought of as a propagating mode when $\omega << \omega_{ssp,0}$ and a localized mode when $\omega \approx \omega_{ssp,0}$ [117, 119], with the transition between these two regimes becoming more gradual with increasing duty cycle a/d (Fig. 3.9(b)).

Two corrugated metal surfaces separated by a dielectric gap create a metamaterial analog to the plasmonic MIM waveguide, which we refer to as a spoof-insulator-spoof (SIS) waveguide (Figure 3.9(a)) [117, 120, 121]. The dispersion equation for this geometry can be calculated using the transfer matrix method described in Refs. [116, 121], which requires us to define an effective permeability and permittivity of the corrugated layer of thickness h which is valid under TM excitation. We do this using two simple heuristics.

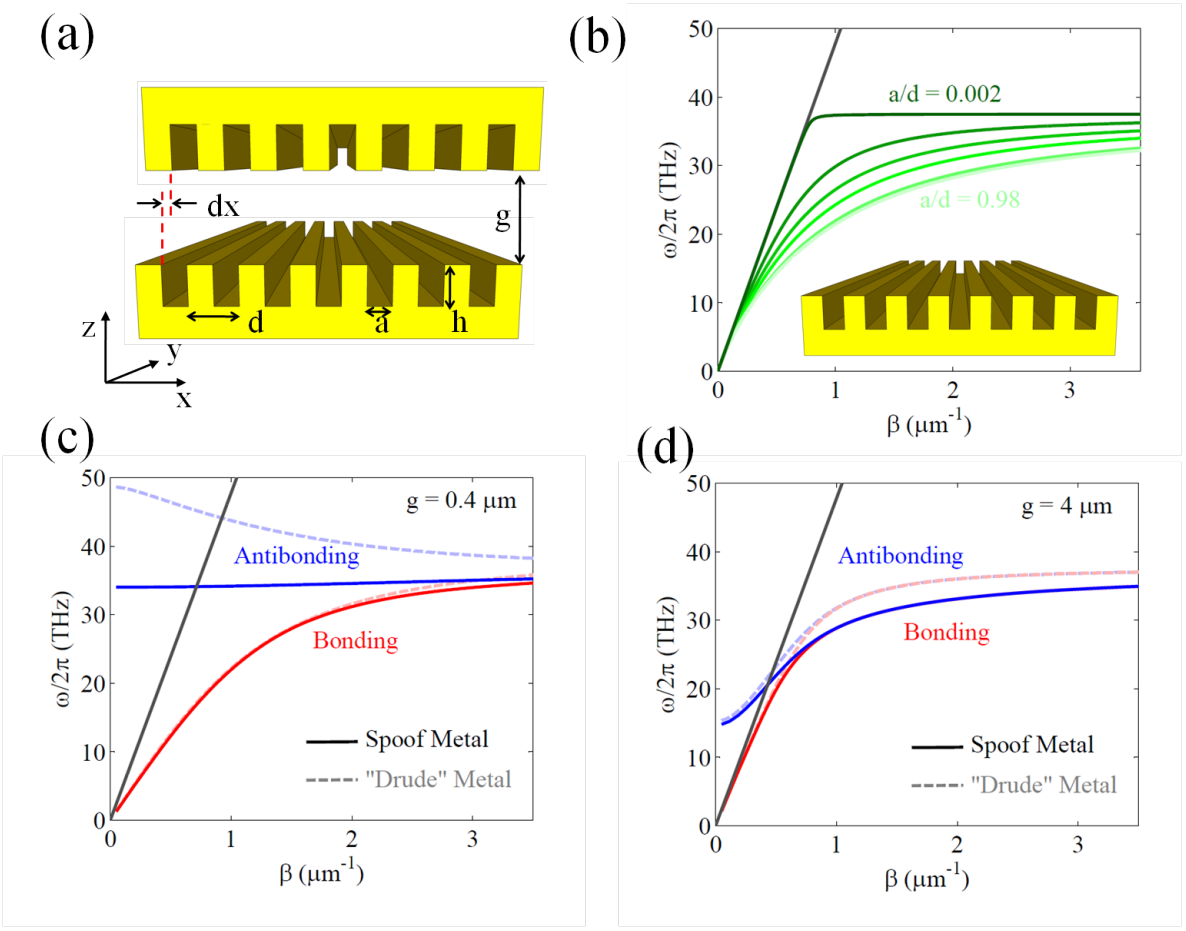

FIGURE 3.9: (a): The coupled SSP waveguide geometry, with height h, period d, duty cycle a/d, and gap g. The offset between the upper and lower grooves is represented by dx. (b): The dispersion relation of an uncoupled SSP mode as determined by Eq. 3.22, for $h = 2$ μm, $d = 0.5$ μm and $a/d = (0.002, 0.2, 0.4, 0.6, 0.8, 0.98)$. (c,d): The bonding (red) and antibonding (blue) modes in a spoof-insulator-spoof (SIS) waveguide for $g = 0.4$ μm (c) and $g = 4$ μm. For comparison, the modes of a MIM waveguide consisting of artificial Drude metals with plasma frequency $\omega_p = \sqrt{2}\omega_{ssp,0}$ are plotted as faded dashed lines in (c) and (d).

First, we recall that the reflectivity of a layer is defined by its impedance $\eta = \sqrt{\mu_s/\epsilon_s}$. For the corrugated layer, this must be equal to the duty cycle of the corrugations a/d, since the PEC sections are perfectly reflective and the gaps are perfectly transmittive. Second, the fraction of the light that is transmitted travels through the layer at c (with $k_z^s = k_0$) since the gaps are filled with air, implying that $n_{eff} = \sqrt{\epsilon_s \mu_s} = 1$. From these two expressions, we can infer that $\epsilon_s = d/a$ and $\mu_s = a/d$. Plugging these values into the transfer matrix for the multilayer stack yields the dispersion relation [121]

$$\frac{\kappa_z^g}{k_0} = \frac{\epsilon_d}{\epsilon_s} \tan\left(k_0\sqrt{\epsilon_d}h\right) \tanh^{\pm 1}\left(\kappa_z g\right) \tag{3.23}$$

where g is the gap in the waveguide and the ± corresponds to the bonding and antibonding modes, respectively. These modes are plotted in Figure 3.9(c) and (d) as the red (bonding) and blue (antibonding) lines for the values of h and d given earlier and $a/d = 0.5$. For comparison, we also plot the bonding and antibonding modes of a non-corrugated MIM waveguide modeled with a lossless artificial "Drude" metal (dashed lines, $\epsilon_{Drude} = 1 - \omega_p^2/\omega^2$, $\omega_p = \sqrt{2}\omega_{ssp,0}$).

At small gaps ($g = 0.4$ μm, Fig. 3.9(c)), SSPs in the bonding mode behave like the bonding-mode SPs in the MIM waveguide geometry, exhibiting strong dispersion and approaching the asymptote at $\omega_{ssp,0}$ as $\beta \to \infty$. Spoof plasmons in the antibonding mode, however, exhibit dispersive properties distinct from antibonding MIM-waveguide plasmons. As $g \to 0$, the SIS antibonding mode has nearly flat dispersion, corresponding to nearly zero group velocity, with $v_g = d\omega/d\beta \to 0^+$, whereas the MIM-waveguide antibonding mode has strong anomalous dispersion ($d\omega/d\beta < 0$) at these gaps. At large gaps ($g = 4$ μm, Fig. 3.9(d)), the SIS waveguide modes and MIM waveguide modes are nearly identical, implying the "plasmon-like" designation is valid in this limit. As $g \to \infty$ the bonding and antibonding modes approach degeneracy, where the only difference between the two modes is the relative phase of the waves on the two corrugated surfaces. The bonding mode corresponds to in-phase waves, while the antibonding mode corresponds to out-of-phase waves, with a corresponding field intensity node in the center of the waveguide. We note that Eqs. 3.22 and 3.23 are valid only for SSPs on PECs when β is less than π/d by approximately a factor of two, since we can no longer treat the corrugated layer in the effective medium limit when the wavelength in the structure

approaches the periodicity of the corrugations. Additionally, the preceding analysis avoided the impact of losses that are present in systems involving real metals.

3.2.3 Spoof Plasmons on Real Metals

In order to account for all geometric and material effects, we use numerical techniques. We simulate a single unit cell of an SIS waveguide with gold surfaces using the finite element method as implemented in COMSOL Multiphysics, enforcing Floquet periodicity at the unit cell boundaries, fixing the wavevector β in each individual simulation. Because COMSOL does not account for material dispersion, we employ an iterative method to accurately determine the eigenfrequencies of the geometry. We start by solving Eq. 3.23 for a fixed β to obtain ω_0^b and ω_0^a, the initial guesses for the resonant frequencies of the bonding and antibonding modes, respectively and use these values to obtain $\epsilon_{Au}(\omega_0^b)$ and $\epsilon_{Au}(\omega_0^a)$ from the Drude model for gold ($\epsilon_{Au}(\omega) = 1 - \omega_p^2/(\omega^2 + i\gamma\omega)$ with $\omega_p/2\pi = 2.18\text{e}15$ Hz, $\gamma/2\pi = 4.34\text{e}12$ Hz [112]). We then solve in COMSOL for the bonding and antibonding modes separately, obtaining our new eigenfrequency guesses, ω_1^b and ω_1^a. We then repeat this process until the values of the eigenfrequencies converge (i.e.: $(\omega_n^{b,a} - \omega_{n-1}^{b,a})/\omega_n^{b,a} < 0.01$). We do this at values of β ranging from $0.05\pi/d$ to $0.55\pi/d$. The resulting dispersion relations are plotted in Figure 3.10(a) for $g = 0.4\mu$m (circles) and $g = 4\mu$m (squares).

Comparing Fig. 3.10(a) to Fig. 3.9(c,d), we see that the real-metal dispersion relations are qualitatively similar to the dispersion relations of SSPs on PECs, though the differences are noteworthy. First, light inside the grooves does not propagate at c (i.e., $k_z^s \neq k_0$, as we assumed earlier). Instead, the grooves act as short MIM waveguides of gap a and have a corresponding effective mode index, $n_{eff} > 1$[122, 123] which changes the cavity resonance condition. Second, the periodicity of the structure introduces a band edge at

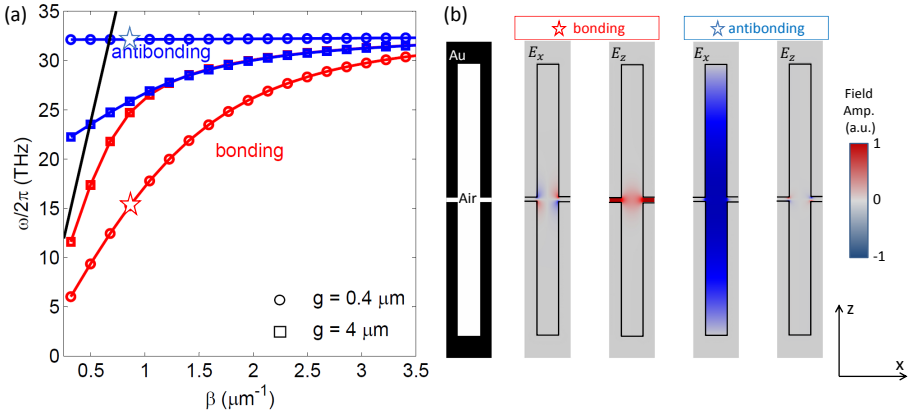

FIGURE 3.10: (a) Dispersion curves for the bonding (red lines) and antibonding (blue lines) modes of the SIS geometry simulated with corrugated gold surfaces corresponding to the geometry in Fig 1(a). Modes were solved at $g = 0.4\mu$m (circles) and $g = 4\mu$m (squares), corresponding to the parameters in Fig. 1(c) and (d). (b) Electric field profiles of a unit cell of the structure for the bonding and antibonding modes at $g = 0.4\mu$m and $\beta = 1\mu\text{m}^{-1}$

$\beta_{edge} = \pi/d$ causing the spoof plasmon frequency to occur at $\omega_{spp} = \omega(\beta_{edge}) < \omega_{ssp,0}$. We also note that our results also show a negligible dependence on the lateral offset dx between the corrugations on the two surfaces (Fig. 3.9(a)), confirming that the structures are in the effective medium limit.

Simulations of the field profiles (Fig. 3.10(b)), at $g = 0.4\mu$m and $\beta = 1\mu\text{m}^{-1}$ illustrate the differences between the two modes. The bonding mode is well confined within the small gap between the two corrugated surfaces and is dominated by the y-component of the electric field, similar to a parallel plate capacitor, or the TEM mode of a parallel-plate waveguide[124]. Like in a capacitor, the surface charge distribution with respect to the center of the gap is antisymmetric and corresponds to an attractive force between the surfaces. Light in the antibonding mode, on the other hand, oscillates back and forth within the deep corrugations and has symmetric charge symmetry with respect to the gap, resulting in a repulsive force.

We can calculate the force between the two spoof surfaces by integrating the Maxwell Stress Tensor (MST) across a plane P separating the two surfaces [7],

$$F = \int_P \overleftrightarrow{\mathbf{T}} \cdot \mathbf{n} da, \tag{3.24}$$

where $\mathbf{n}$ is normal to $\mathbf{P}$ and $\overleftrightarrow{\mathbf{T}}$ is the second-rank MST expressed as

$$\overleftrightarrow{\mathbf{T}} = \left[\epsilon_d \mathbf{EE} + \mu_0 \mathbf{HH} - \frac{1}{2}\left(\epsilon_d |\mathbf{E}\cdot\mathbf{E}| + \mu_0 |\mathbf{H}\cdot\mathbf{H}|\right) \overleftrightarrow{\mathbf{I}}\right], \tag{3.25}$$

with $\mathbf{E}$ and $\mathbf{H}$ as the electric and magnetic fields, respectively. We plot the magnitude of the force $|F_z|$ as a function of g in Figure 3.11(a) for the bonding (red lines) and antibonding modes (blue lines) at $\lambda = 10$ μm (solid lines, circles), 11 μm (dashed lines, squares), and 12 μm (dash-dot lines, triangles), normalizing the force per unit area to the power flowing through the waveguide. At large gaps ($g > \lambda/4$), the bonding and anti-bonding forces have approximately the same magnitude but opposite sign, corresponding to gaps where the dispersion curves approach degeneracy (see inset). As the gap decreases, the splitting between the modes increases and the bonding and antibonding force magnitudes diverge. The repulsive force generated by the antibonding mode grows asymptotically as $\beta \to 0$ and the separation approaches the value corresponding to cutoff for the mode g_c. g_c corresponds to the lowest order mode of a vertical cavity defined as the range extending from the bottom of a corrugation on the bottom surface to the top of a corrugation on the top surface, such that at small gaps, where the coupling between neighboring grooves can be ignored, cutoff occurs when $\lambda/2 \approx 2h + g$. (At larger gaps, the full structure of the surface must be taken into account, making this formula illustrative, but imprecise.) The bonding mode also experiences a cutoff as $\beta \to \pi/d$ due to the growth of the band gap, though this occurs at a much smaller separation. The force generated by the bonding mode increases exponentially as the gap width decreases, corresponding to the increase in field intensity in the gap, and

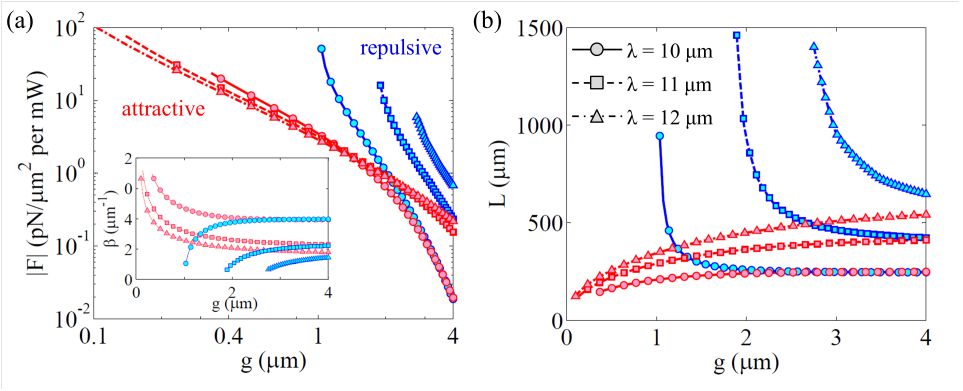

FIGURE 3.11: (a): Attractive (red lines) and repulsive (blue lines) forces generated by the bonding and antibonding modes, respectively, at three wavelengths: $\lambda = 10$ μm (solid lines), 11 μm (dashed lines), and 12 μm (dash-dot lines), as a function of gap width. The wavevectors of these modes are plotted in the inset, showing degeneracy at large gaps, and splitting at small gaps. The antibonding mode has a clear cutoff gap. (b): The propagation length of the bonding (red) and antibonding (blue) modes plotted in (a). The propagation length of the bonding mode deceases as the gap decreases, while the propagation length of the antibonding mode increases as it approaches cutoff.

the build-up of surface charge along the surface, mimicking the properties of the MIM waveguide bonding mode [112]. Both modes are capable of generating forces orders of magnitude larger than radiation pressure, which is 6.67pN/μm^2 per mW.

3.2.4 Discussion and Conclusions

Applications of these structures, like conventional surface plasmon waveguides, will ultimately be limited by absorption. MIM waveguides that achieve subwavelength confinement [89] have propagation lengths on the order of only one free-space wavelength at visibile and near-IR frequencies, introducing significant heating and limiting the possibilities for optical interconnects or active-plasmonic devices at these frequencies. Furthermore, other options for mid-IR and terahertz surface waveguidng, such as surface phonon polaritons, still suffer from significant absorption due to their proximity to a material resonance [125]. We quantify the absorption in our modes by calculating the propagation length L from the complex eigenfrequency given by our simulations, $\tilde{\omega} = \omega' + i\omega''$ at a fixed and purely real value of β. The resulting expression, $L^{-1} = -\omega''/2v_p$, is plotted in

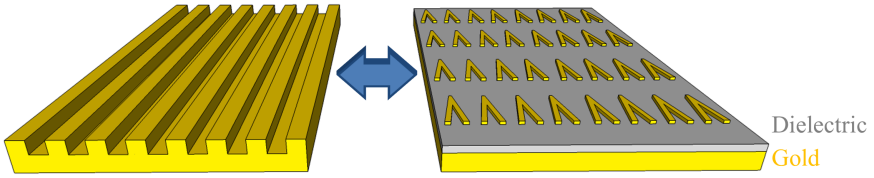

FIGURE 3.12: Spoof structure (left) and example of a spoof-equivalent structure (right) to simplify fabrication. The spoof-equivalent structure consists of resonant metallic elements separated from a metal back-plane by a thin dielectric spacer layer.

Fig 3.11(b) for the modes in (a). Much like standard surface plasmons, the propagation length of the bonding mode (red lines) decreases as the mode confinement increases, and is longest farther from the plasmon resonance frequency (i.e. longer wavelengths). The propagation length of the antibonding mode (blue lines), on the other hand, increases as it approaches cut-off. Recalling the plot in Fig. 3.10(a), this can be understood as the transition of the mode from plasmonic to photonic, as the wavevector (inset, Fig. 3.11(a) moves from outside to inside the light cone. Even when $g << \lambda_0$, both modes can propagate distances longer than $10\lambda_0$, with the antibonding mode propagating longer than $100\lambda_0$ as it approaches cutoff, making these modes viable for waveguiding applications.

Experimental realization of these structures will be necessary to demonstrate a new array of optomechanical devices at mid-IR and terahertz frequencies. While single SSP waveguides have been demonstrated [118–120], none have truly been in the metamaterial limit ($d < \lambda/10$), as the aspect ratio of the grooves required to reach this limit is difficult to achieve experimentally. However, structures equivalent to spoof surfaces have been demonstrated by placing a periodic array of metallic elements, such as patch antennas [126] or potentially v-antennas [127], above a metallic backplane, separated by a thin dielectric layer (Fig 4). Instead of controlling the depth of the grooves to determine the SSP resonance, the shape of the metallic elements changes the phase response of the surface, and thus also controls the resonance condition.

In conclusion, we have described the dispersion of spoof surface plasmon modes in spoof-insulator-spoof waveguides, demonstrating that MIM waveguiding concepts can be extended into the mid-IR and terahertz frequency ranges where losses are comparatively smaller. We investigated the forces generated by spoof surface plasmons and showed that forces greater than radiation pressure are attainable for highly confined mid-IR optical fields. The attractive and repulsive forces generated within SIS waveguides have a wide range of applications, as they extend optomechanical functionality to any frequency range while maintaining tight confinement of the optical field.

3.3 Repulsive Surface Plasmon Forces in Fluids

3.3.1 Introduction

Surface plasmon (SP) radiation forces were first experimentally investigated in the context of fluids. Volpe, et al. [93] published the first study on the forces from SPs on a glass sphere near a gold surface in water, using the so-called Kretchman configuration, shown in Figure 3.13. In this geometry, SPs can be excited at the gold-water interface through a prism, as long as the refractive index of the prism (n_p) is higher than that of the fluid (n_f) and the gold layer thickness is on the order of the skin depth so that light can couple from one side of the film to the other. Under these conditions, surface plasmons can be excited according to the following expression:

$$\frac{\omega}{c} n_p \sin(\theta) = \omega_c \sqrt{\left(\frac{\epsilon_f \epsilon_g}{\epsilon_f + \epsilon_g}\right)} \tag{3.26}$$

where θ is the angle between the incident field and the interface normal, and $\epsilon_i = n_i^2$ for $i = g, f$. Volpe et al. demonstrated that plasmons coupled in this matter were

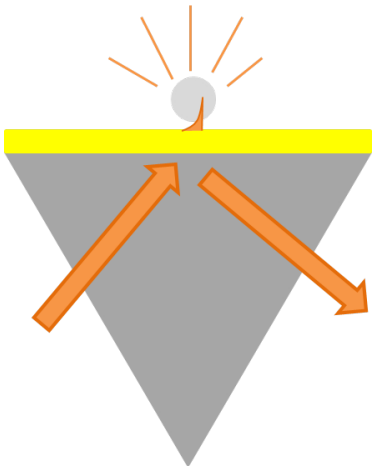

FIGURE 3.13: Kretchmann geometry. A high refractive index prism is coated with a thin metallic layer whose thickness is near the skin depth of the metal (typically 20 nm $< t <$ 50 nm. Transverse-magnetic polarized light incident on the metal film through the prism at the resonance angle θ_{spp} will excite SPPs on the top surface of the metal. Dielectric particles near the surface will interact with the surface plasmon field, scattering some of the light but also experiencing a force from the field gradient.

responsible for two forces on the particles in the fluid. First, a force due to light scattering off of the particle worked to push the particle along the surface, while the gradient worked to attract the particle to the surface. While some questions were raised about the methodologies used in analyzing this data, subsequent work by this and other groups demonstrated the power of surface plasmon forces in fluids [94, 128, 129].

In previous experiments, glass or polymer particles with refractive indexes around $n = 1.5$ were studied in water, which has a very low refractive index ($n \approx 1.33$) at visible frequencies. Recalling Eqs. 1.1 and 1.2, we see that the sign of the gradient force is a direct consequence of this refractive index contrast: the sign of the polarizability α of the particle depends on the relative values of the dielectric functions of the particle and its surrounding environment. By simply inverting this relationship, we can generate a repulsive gradient force, akin to a negative optical trap [130, 131]. Negative plasmon trapping - or negative total internal reflection trapping - have yet to be explored experimentally, yet it offers new avenues for spectroscopy using the optical near field, particularly in applications which wish to avoid direct interaction with the substrate. By

using repulsive forces, an optical field can effectively act as a buffer between the particle and the surface, where the minimum particle-substrate separation is determined by the power in the optical field.

3.3.2 Beyond the Dipole Limit: Forces on Large Particles

We chose to explore repulsive surface plasmon forces on particles larger than the optical wavelength such that Eqs. 1.1 and 1.2 fail to quantitatively represent the behavior of the particle in the fluid. In particular, Eqs. 1.1 and 1.2 assume that the particle does not significantly perturb the optical field. This assumption does not hold when the decay length of the plasmon L_d is smaller than the particle radius R but larger than the particle-substrate separation t. To get an analytical understanding of the behavior of the system in this limit, we can look at the 1-D case, where a metallic half-space and a solid-dielectric half-space are separated by a fluid of thickness t, as shown in Fig. 3.14. Using the transfer matrix method discussed in Section 3.2, we can write the dispersion relation for this geometry as

$$1 + \tanh(k_{y2}t)\frac{\left(\frac{k_{y2}}{\epsilon_2}\right)^2 + \frac{k_{y1}k_{y3}}{\epsilon_1\epsilon_3}}{\frac{k_{y2}k_{y3}}{\epsilon_2\epsilon_3} + \frac{k_{y1}k_{y2}}{\epsilon_1\epsilon_2}} = 0 \tag{3.27}$$

where $k_{yi} = \sqrt{(\beta^2 - (\omega/c)^2\epsilon_i)}$, $i = 1, 2, 3$, β is the wavevector, and ϵ_1, ϵ_2, and ϵ_3 are defined in Fig. 3.14.

For the following analysis, we chose to study a geometry consisting of a silicon dioxide particle ($n_{SiO_2} = \sqrt{\epsilon_{SiO_2}} = 1.45$) in bromobenzene ($n_{bromo} = 1.55$) above a gold film ($n_{Au} = 0.19 + 3.1i$) on a high-index glass prism ($n_{prism} = 1.78$). We plot the dispersion relation calculated using Eq. 3.27 in Figure 3.15 for two different fluid thicknesses:

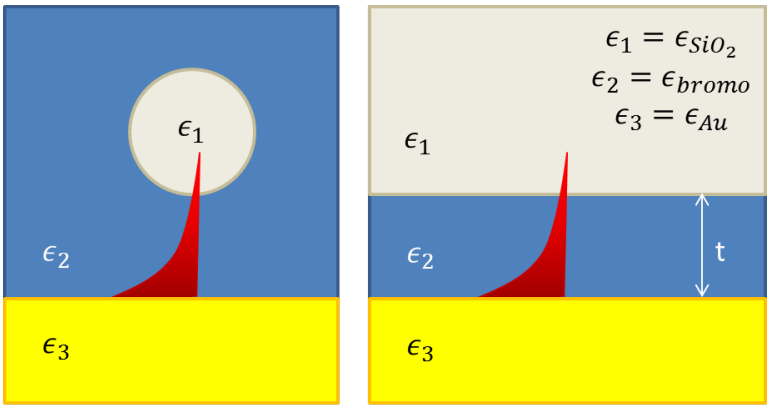

FIGURE 3.14: (a) Geometry consisting of a dielectric particle submerged in a fluid above a metallic surface such that dielectric function of the fluid is larger than that of the particle $\epsilon_2 > \epsilon_1$. (b): 1-D equivalent of the geometry in (a). As long as the particle radius is larger than the optical wavelength, one can reasonably approximate the cyllender-plate geometry as a plate-plate geometry.

t = 20 nm (red line) and t = 600 nm (blue line). The air light line ($\beta = \omega/c$ – solid black line), glass light line, ($\beta = \omega n_{glass}/c$ – large dashes) and bromobenzene light line ($\beta = \omega n_{bromo}/c$ (small dashes)) are plotted for reference. The range of frequencies plotted corresponds to visibile and near-IR wavelengths between 470 nm and 1250 nm. Across this range, $g_{OM} = d\omega/ds < 0$ (red-to-blue colored arrow), corresponding to a repulsive interaction. We plot the force F (Eq. 3.20 and Section 2.1.1) per unit optical power as a function of gap for three separate wavelengths: λ = 633 nm (red cirlces), 750 nm (blue squares), and 950 nm (green triangles) in Figure 3.16.

The trends shown in Fig. 3.16 reveal that at small separations, shorter wavelengths produce greater force, while at larger separations, longer wavelengths produce greater force, with an exponential dependence on the separation. This is an intuitive result when we consider that the main contributor to the force is the strength of the field gradient. Longer wavelengths have a longer evanescent decay length $l = 1/k_{y2}$, resulting in a more gradual gradient but longer reach than shorter wavelengths, which have a short, sharp, evanescent fields in the fluid. At visible frequencies (λ <750 nm), the repulsive plasmon gradient force out-performs radiation pressure ($F_{rad} = 2R_iP/c$, where R_i is the

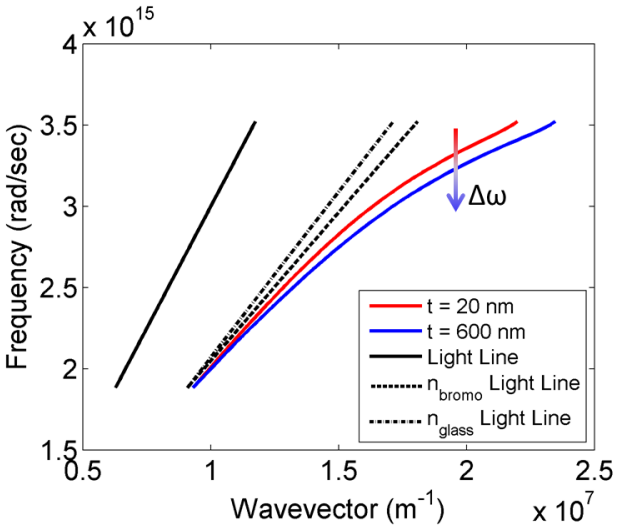

FIGURE 3.15: Dispersion relation for the repulsive plasmon geometry between $\omega = 1.5e15$ rad/sec ($\lambda = 1250$ nm) and $4e15$ rad/sec (470 nm). Gold has a surface plasmon resonance near $\lambda = 450$ nm, causing strong dispersion at the longer wavelengths near this resonance. The air light line (solid black line), glass light line (dash-dot line) and bromobenzene light line (dashed line) represent the speed of light in each medium. The dispersion curve of the plasmon when the gap is small ($t = 20$ nm, red line) follows the glass light line, while the dispersion curve at large gaps ($t = 600$ nm, blue line) follows the bromobenzene light line. At constant wavevector, the resonance frequency decreases as the separation increases (red-to-blue arrow), implying a $g_{OM} < 0$ and a repulsive force.

reflectivity of the glass-bromobenzene interface) by as much as an order of magnitude. At close separations, the plasmon field is almost entirely contained within the sold material, and the dispersion curve approaches that of a system in which there was no fluid at all. In this limit, the electric field amplitude at the fluid-dielectric interface is approximately equal to that on the metal-fluid interface, corresponding to the flattening of the force curves seen in Fig. 3.16.

While this 1-D simulation presents a rather simplistic picture of the sphere-plate geometry, the analysis provides results consistent with more rigorous numerical calculations and simulations. A 2-D geometry, Fig. 3.17, was modeled in COMSOL Multiphysics in order to account for the effects of the prism and of the curvature of the particle. The geometry consists of a infinite dielectric cylinder (directed in the plane of the page) with a 2.5 μm radius above a high-refractive index ($n_p = 1.78$) material coated with

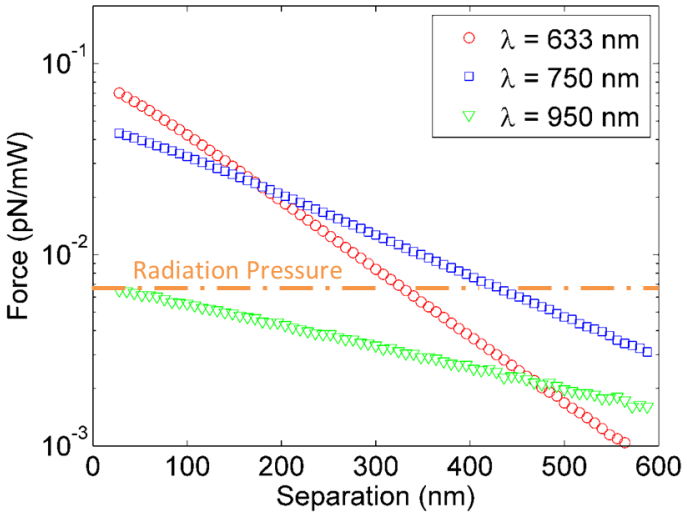

FIGURE 3.16: Repulsive plasmon forces. At visible frequencies, (λ =633 nm – red circles, λ =750 nm – blue squares), the surface plasmon force is capable of out-performing radiation pressure by an order of magnitude at separations smaller than 250 nm. At near-IR wavelengths (λ = 950 nm – green triangles), the plasmon force is smaller than radiation pressure but can generate larger forces at larger separation due to the longer evanescent tail of the field.

a 50 nm thick layer of gold. The simulations looked at modes at λ = 1500 nm propagating normal to the simulation plane and included periodic boundary conditions to in the x-direction to approximate the effect of an infinite surface in the x-direction. (The simulation geometry was made wide enough so that there would be no coupling across the periodic boundary.) Fig. 3.17 shows electric field profiles for two different values of t: 3 μm (a) and 200 nm (b). Both modes leak out into the prism, indicating that the mode can be coupled into through the prism in the Kretchmann geometry. In (a), the cylinder is well above the substrate and does not significantly perturb the evanescent plasmon field in the bromobenzene. In (b), the perturbation is quite strong. As discussed in Chapter 1, this effect can be understood by looking at the dipole picture of materials. The surface plasmon induces dipoles in both the fluid and the cylinder, though the fluid dipoles are stronger due to its higher refractive index. As a result, the strong displacement field generated in the fluid effectively induces an out-of-phase dipole in the particle at the fluid-particle interface, resulting in a screening of the field inside

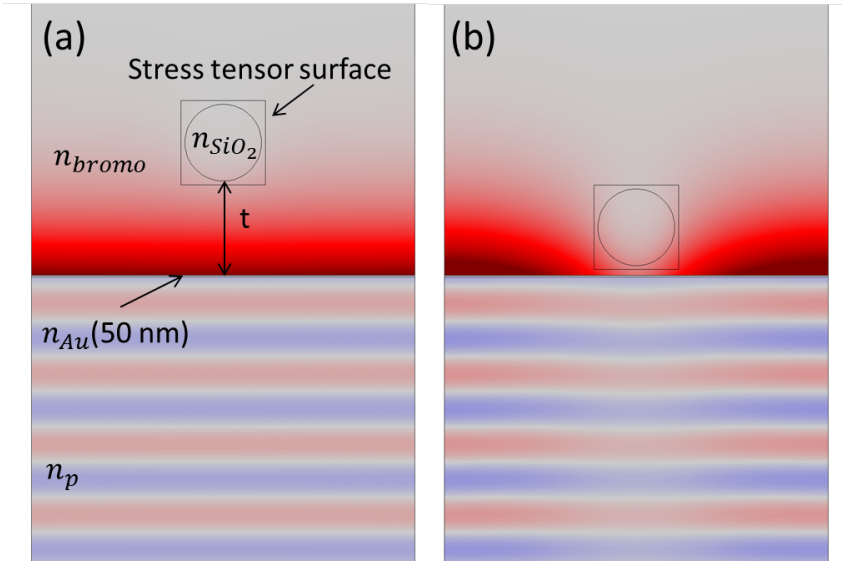

FIGURE 3.17: Field perturbation by a low index dielectric particle in bromobenzene above a gold coated glass prism. (a) A particle high above the substrate results in only a weak perturbation to the field. (b) A particle near the surface strongly perturbs the field, pushing the field concentration away from the particle. The force in both cases can be calculated by integrating the Maxwell Stress tensor on a boundary around the particle (square box around circle).

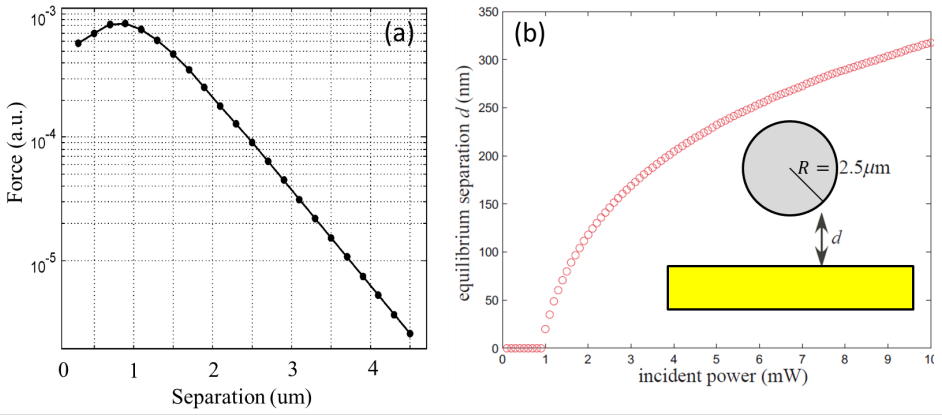

FIGURE 3.18: (a) Plasmon force on a glass particle in bromobenzene calculated using the Maxwell Stress Tensor on the boundary seen in Fig. 3.17 as a function of separation. The force decreases at small separations, differing from the curves in Fig. 3.16 due to finite size effects of the particle. (b) Equilibrium separation as a function of input power formed by the repulsive plasmon force and gravity, calculated using the proximity force approximation for an R=2.5μm particle.

the particle and a repulsive interaction.

Rather than use the Eq. 3.20 to calculate the force from the change in free energy as we did previously, we instead calculate the force via the Maxwell Stress Tensor on a square boundary surrounding the cylinder (as shown in Fig. 3.17). The results, shown in Fig.

3.18(a) as a function of separation, qualitatively agree with the analytic calculations for separations larger than 1 μm. At smaller separations, finite size effects come into play, causing in the magnitude of the force to decrease slightly. This decrease can be understood via the Proximity Force Approximation (PFA), which says that the force between a sphere and a plate can be calculated by representing the spherical surface as a stepped planar surface, as long as the $t << R$. Mathematically, the relationship between the plate-plate force and the sphere-plate force calculated using PFA is

$$\frac{F_{plate-plate}}{F_{PFA}} = \frac{3t}{R}. \tag{3.28}$$

This expression is illustrated in Fig. 3.19.

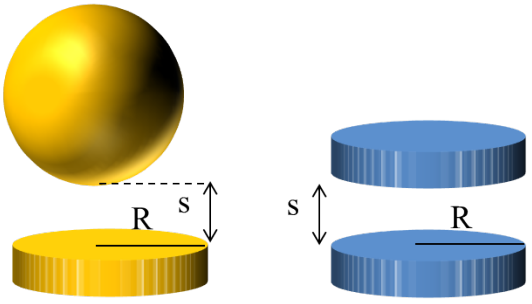

FIGURE 3.19: Graphical representation of the Proximity Force Approximation. The force between a sphere and a plate (left) can be obtained from calculating the force between two parallel plates (right) using Eq. 3.28 as long as $s << R$, allowing the sphere-plate geometry to be solved analytically.

Therefore, it follows that as the plate-plate interaction flattens out as $t \rightarrow 0$, the sphere-plate force should decrease in the same limit. Using this approximation, we can find the equilibrium height of the cylinder above the substrate under the influence of the plasmon force and gravity as a a function of optical power. The result is plotted in Fig. 3.18(b) for $\lambda = 633$ nm, showing a plasmon force which can overcome gravity at optical powers greater than 1 mW.

The repulsive plasmon force provides a unique new tool for investigating the behavior of dielectric particles near - but not against a surface, by allowing the combination of current surface plasmon resonance spectroscopy methods to be paired with optical trapping to study binding mechanisms [132, 133] and interface dynamics [79, 134] of chemicals or biomolecules. Furthermore, it allows for a kind of "frictionless waveguiding," where a particle could be guided along a strip of metal on a surface without touching the metal strip.

Chapter 4

The Casimir Effect

4.1 Introduction

The Casimir effect describes the force that arises between neutral objects from quantum and thermal fluctuations of the electromagnetic field. Due to the presence of a finite "zero-point" energy – i.e. the energy of a system in its quantum ground state – electric dipoles in an ensemble will be in a state of constant flux, spontaneously jostling about in space[135]. These spontaneous fluctuations generate fluctuating fields – exponential in time rather than sinusoidal – which in turn induce dipoles moments in nearby particles. These fluctuating fields must still obey the electromagnetic boundary conditions of their environment set by Maxwell's Equations. Hendrik Casimir predicted this effect based on a simple model involving two parallel, thin, perfectly conducting plates in vacuum separated by a distance s [136]. The boundary conditions of this system are simple: electric fields normal to the plates go to zero at the plate-vacuum interface, restricting modes within the gap which are evenly spaced in frequency: $\nu_n = cn/2s$, where $n = 0, 1, 2, 3, ...$ Outside of the plates, there are no such restrictions, resulting in a uniform

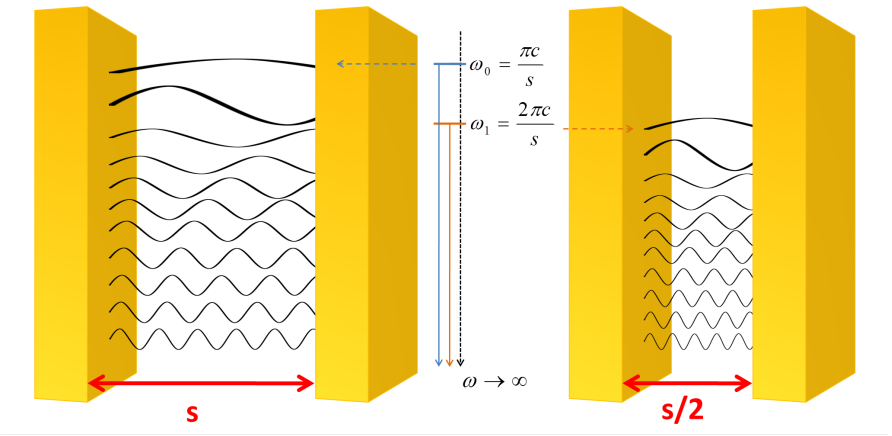

FIGURE 4.1: Two parallel, perfectly conducting plates, seen at left, separated by a distance s support equally space modes starting at $\omega_0 = \pi c/s$, separated by $\Delta\omega = \pi c/s$ and continuing to infinity. Decreasing the separation to $s/2$, as seen at right, results in evenly spaced modes starting at $\omega_{=}2\pi c/s$ and separated by $\Delta\omega = 2\pi c/s$ continuing to infinity. The narrower plates contain fewer modes than the wider plates due to the lower density (larger spacing) and larger fundamental frequency.

continuum of modes. Inside the plates, as the separation decreases, the fundamental frequency ω_0 increases, as does the spacing between the modes, resulting in a mode density which decreases with s, as pictured in Figure 4.1.

With this picture, we can think of the Casimir force heuristically. The modes outside of the plates exert a pressure on the plates which is out of balance with the pressure exerted by the modes inside the plates. This imbalance increases as the separation decreases, leading to an exponentially larger force as the separation decreases. Casimir demonstrated that the pressure between these plates could be written as

$$P_c = \frac{\hbar c \pi^2}{240 s^4}. \tag{4.1}$$

Lifshitz, Dzyaloshinskii and Pitaevskii later [137, 138] generalized Casimir's formulation, deriving an analytic expression for calculating the force between two parallel plates of any isotropic material known as the Lifshitz equation. The formulation relates the fields generated by the spontaneous dipole fluctuations to the dielectric functions of

the materials in the system. Because these fluctuations are broad-band - they happen spontaneously at all time scales - this formulation requires information on the entire dielectric function of the material. Additionally, the fields emitted by spontaneous dipole fluctuations are exponential rather than sinusoidal in time. We can thus study the system at imaginary frequencies $\xi \equiv i\omega$, where the dielectric function at imaginary frequencies $\epsilon(i\xi)$ can be obtained from $\epsilon(\omega)$ using the Kramers-Kronig relation:

$$\epsilon(\xi) = 1 + \frac{2}{\pi} \int_0^{infty} \frac{\omega \mathrm{Im}[\epsilon(\omega)]}{\omega^2 + \xi^2} d\omega. \tag{4.2}$$

The Lifshitz equation finds the Helmhotz free energy G of a system consisting of two thick slabs of identical isotropic material separated by a distance s and is written as:

$$G(s) = \frac{k_b T}{2\pi} \sum_{m=0}^{\infty\prime} \int_0^{\infty} k \mathrm{d}k \ln\left[\left(1 - \left[r_{2,1}^{TE}\right]^2 e^{-2k_2 s}\right)\left(1 - \left[r_{2,1}^{TM}\right]^2 e^{-2k_2 s}\right)\right] \tag{4.3}$$

where c and k_b are the speed of light and Boltzmann's constant, respectively, T is the temperature of the system, $r_{2,1}^{TE}$ and $r_{2,1}^{TM}$ are the TE and TM reflection coefficients for the air-slab interface given by

$$r_{2,1}^{TE} = \frac{k_1 - k_2}{k_1 + k_2} \tag{4.4}$$

and

$$r_{2,1}^{TM} = \frac{k_1 \epsilon_2 - k_2 \epsilon_1}{k_1 \epsilon_2 + k_2 \epsilon_1}. \tag{4.5}$$

In Eqs. 4.3-4.5, subscript 1 refers to the slab material while subscript 2 refers to the gap material and

$$k_i = \sqrt{k^2 + \frac{\epsilon_i \xi_m^2}{c^2}} \tag{4.6}$$

is the wavevector component in layer i normal to the interface. The prime on the sum in Eq. 4.3 indicates giving a half weight to the $m = 0$ term, which prevents double counting the TEM mode contribution (where the TE and TM modes are degenerate). We note that Eq. 4.3 is evaluated at discrete imaginary frequencies $\xi_m = \frac{2\pi k_b T}{\hbar} m$ (which appear in Eq. 4.6), known as Matsubara frequencies [137]. While it may seem at first as though we are skipping over key information by summing over ξ rather than integrating, recall that due to Eq. 4.2, the dielectric function at any one value of $i\xi$ contains information about ϵ at all ω. Furthermore, this construction allows us to see the connection between the underlying quantum and thermodynamic bases for Casimir by relating discrete energy levels at $\hbar\xi_m$ to the system's thermal energy $k_b T$ [135].

The Casimir pressure between two parallel plates can be calculated by taking the spatial derivative of the free energy,

$$P_{cas} = \frac{1}{A}\frac{dG}{ds}, \tag{4.7}$$

where A is the interaction area of the plates, and which is plotted in Fig. 4.2 for four materials: gold (blue line), silicon nitride (green line), high and low-doped silicon (red and cyan lines, respectively), and silicon dioxide (magenta line). The electric permittivities of the materials as a function of imaginary frequencies are plotted in the inset, and monotonically decrease as a function of $i\xi$. The Casimir force is strongest when the

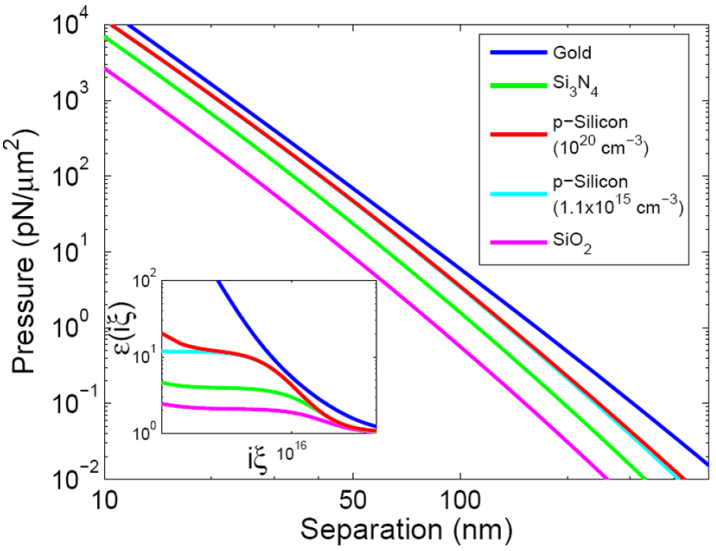

FIGURE 4.2: Pressure between two halfspaces comprised of different materials: Gold (blue line) high and low doped p-type silicon (red and cyan lines, respectively), Silicon Nitride (Si_3N_4, green line) and Silica (SiO_2, magenta line). The force between silicon slabs is independent of doping density and is approximately 75% the force between gold slabs. In general, the strength of the force scales with the magnitude of the dielectric function at imaginary frequencies (seen at inset).

slabs have the highest dielectric function (i.e. are the most metallic). The doping level of silicon, which only effects ϵ at low imaginary frequency, has negligible effects on the Casimir force. For scale, the pressure between two parallel perfect electric conductors separated by $s = 10$ nm is approximately 1 atm (10^5 pN/μ m^2), which is $\approx 30\%$ greater than the Casimir force between two gold plates.

Because this force becomes so strong at small gaps, it can be a source of failure in MEMS and NEMS devices [139]. However, the Casimir force can also be a source of nonlinearity which can be utilized to make dynamic mechanical elements that are extremely sensitive to changes in their local environment [39, 56]. In this chapter, I discuss the Casimir force as it pertains to the optomechanical devices discussed in Chapter 2 discussing preliminary experimental results as well as plans for future experiments.

4.2 Casimir MEMS

4.2.1 Theory

Note: Analysis in this section was taken primarily from Rodriguez, Woolf, et al. [39]. This work was conceived and executed by Rodriguez and Woolf, with Rodriguez implementing the Casimir modeling and Woolf implementing the mechanical modeling.

The optomechanical structure studied in Chapter 2 consists of a silicon membrane perforated with a square lattice of holes suspended above an SOI substrate by four arms. Initial simulations characterized a square membrane of width $W = 23.4\mu$m and thickness $h = 130$ nm supported by four arms of length $L = 35\mu$m and cross-sectional area 130 nm $\times$ 2 μm, containing a photonic crystal hole array of periodicity $p = 650$ nm. These parameters correspond to an attractive optical mode with $Q_{opt} \approx 1000$, $g_{OM} \approx 50$ GHz/nm, and a mechanical stiffness of $K = 5e^{-2}$ N/m. In what follows, we consider quasistatic membrane deformations induced by static and spatially uniform optical and Casimir forces. The mode profile is illustrated in Fig. 4.3 and consists of an approximately flat membrane with deformed supports, making this structure less susceptible to optical losses stemming from curvature.

For an initial membrane-surface separation s_0 and in the absence of optical forces, the membrane will experience two forces as a function of separation s: a restoring mechanical force $F_m = -K(s_0 - s)$ and the attractive, monotonically decaying Casimir force F_c. F_c was computed via the standard proximity-force approximation (PFA, see Chapter 3.3.2) which we have checked against exact time-domain calculations and found to be accurate to within 3%. The sum of these two forces corresponds to a harmonic oscillator potential ($U = K(s_0 - s)^2$) which is perturbed by a decaying exponential as $s \to 0$. The Casimir

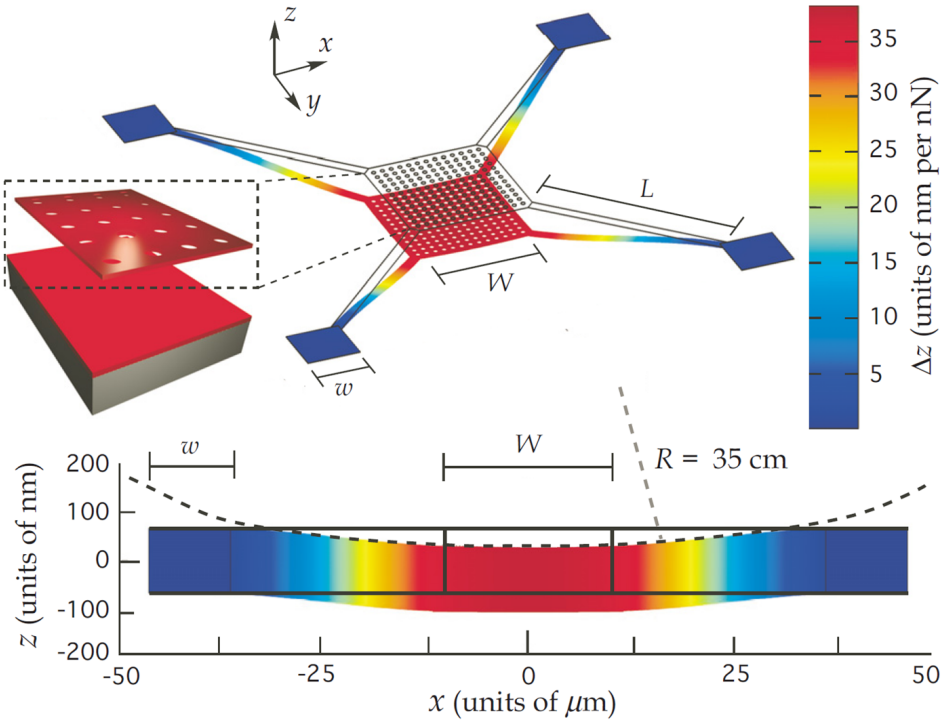

FIGURE 4.3: Preliminary geometry studied for investigation of the Casimir force in an integrated MEMS systems, consisting of a $W = 30\mu$m square silicon membrane supported by four arms of length $L = 35\mu$m. This membrane is initially suspended 150 nm above a silicon substrate. A 100 nm deflection of the membrane (seen in lower panel) results in a 35 cm radius of curvature of the membrane. The Casimir force for this curvature is 97% the plate-plate Casimir force, making this system a good a good candidate for plate-plate Casimir force experiments. (From [39])

effect shifts the potential minima to a slightly smaller separation while introducing an unstable "Casimir equilibrium" at the point where the mechanical restoring force and Casimir force are equal and in opposite directions. The optical force introduces an additional perturbation to the potential whose shape resembles an error function, in what is known as the optical spring effect [65].

Figure 4.4 displays the total potential, including the mechanical spring, the optical spring, and the Casimir effect, for a laser emitting 7 mW of power at wavelengths between 1537 nm and 1574 nm for two initial values of s_0: 155 nm (Fig. 4.4(a)) and 140 nm (Fig. 4.4(b)). At $s_0 = 155$ nm, the perturbation to the potential from the Casimir force (which introduces an unstable equilibrium at $s = 75$ nm and the drop-off in the

potential at smaller gaps) is small and can be ignored so that we can study the behavior of the system in the absence of the Casimir force. Because the optical resonance shifts as a function of separation, the incident laser frequency greatly determines the overall potential of the system. Furthermore, the system is bistable and exhibits hysteresis between $\lambda_l = 1551$ nm (cyan line) and 1559 nm (purple line), featuring a "mechanical equilibrium" near s_0 and an "optical equilibrium" at a smaller separation corresponding to when $\lambda_l = \lambda_0$. The equilibria at all wavelengths are labeled with circles.

If we decrease the initial membrane-substrate to $s_0 = 140$ nm (Fig. 4.4(b)), the Casimir force is no longer negligible. The system is still bistable at $\lambda_l = 1566$ nm and 1559 nm. However, at $\lambda_l = 1574$ nm (black line), the stable "optical equilibrium" merges with the unstable "Casimir equilibrium." In other words, sweeping the laser from 1537 nm to 1574 nm will result in stiction, as the Casimir force becomes stronger than the restoring mechanical force near $\lambda_l = 1574$ nm.

The equilbrium separations, labeled with circles in Fig. 4.4(a),(b), are plotted as a function of laser wavelength in the absence and presence of the Casimir force, in Fig. 4.5(a) and (b) respectively, for light incident at laser powers of 4 mW (black line), 7 mW (red line) and 15 mW (green line). Two bifurcation wavelengths, denoted by λ_+ and λ_- as indicated in the figure, represent the boundaries of the bistable region and thus correspond to abrupt jumps in the system's equilibrium as the laser wavelength is swept up (λ_+) or down (λ_-) across the optical resonance. The arrows indicate the hysteretic path followed during forward and backward sweeps of the laser. The dashed portions of the curves represent the location of an unstable equilibrium (i.e. the peak of the potential barrier between the two stable equilibria seen at the bistable wavelengths in Fig. 4.4). The inset in Fig. 4.5(a) shows the height of this potential, measured from the bottom of the "optical equilibrium" potential well to the peak of the barrier.

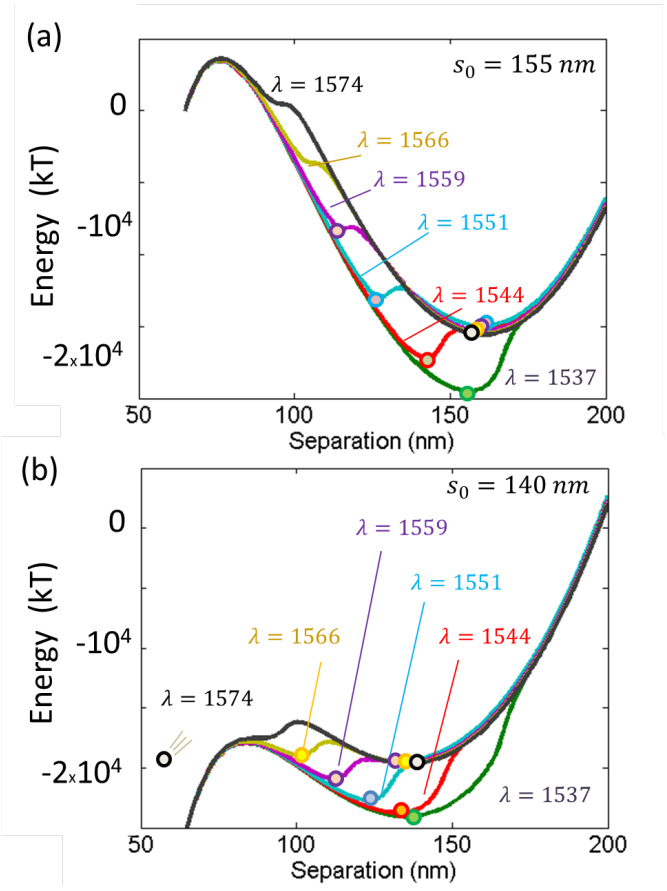

FIGURE 4.4: (a): Potential energy diagrams for a mechanically free silicon membrane 155 nm above a silicon substrate experiencing an optical force and the Casimir effect. The curves are shown for seven wavelengths: $\lambda = 1574$ nm (black line), 1566 nm (yellow line), 1559 nm (purple line), 1551 nm (cyan line), 1544 nm (red line) and 1537 nm (green line). Local minima are labeled with circles matching the color of the curve. The optical potential, which resembles an error function, shifts with wavelength according to the g_{OM} of the mode. For a range of wavelengths (1554 nm - 1559 nm), there are two stable solutions, indicating bistability. Correspondingly, forward and backward wavelength sweeps would display mechanical hysteresis. The Casimir force, responsible for the downward bend near s = 50 nm, is too small to significantly affect dynamics in this devce. (b): If we decrease the initial separation to 140 nm, the Casimir effect plays a more significant role. A wavelength sweep from 1537 nm to 1574 nm would lead to stiction, as the local minima generated by the optical potential disappears and is funneled into a global minima at s = 0.

The presence of the Casimir force (Fig. 4.5(b)) affects the membranes response to the optical force via the introduction of an additional unstable equilibrium between $s = 0$ and the separation corresponding to the "optical resonance" (dashed lines at the bottom of the figure). Increasing the laser wavelength in a continuous sweep results in a downward optical pressure on the membrane, decreasing the equilibrium, until the laser reaches λ_s, the bifurcation point where the stable "optical equilibrium" merges with the unstable

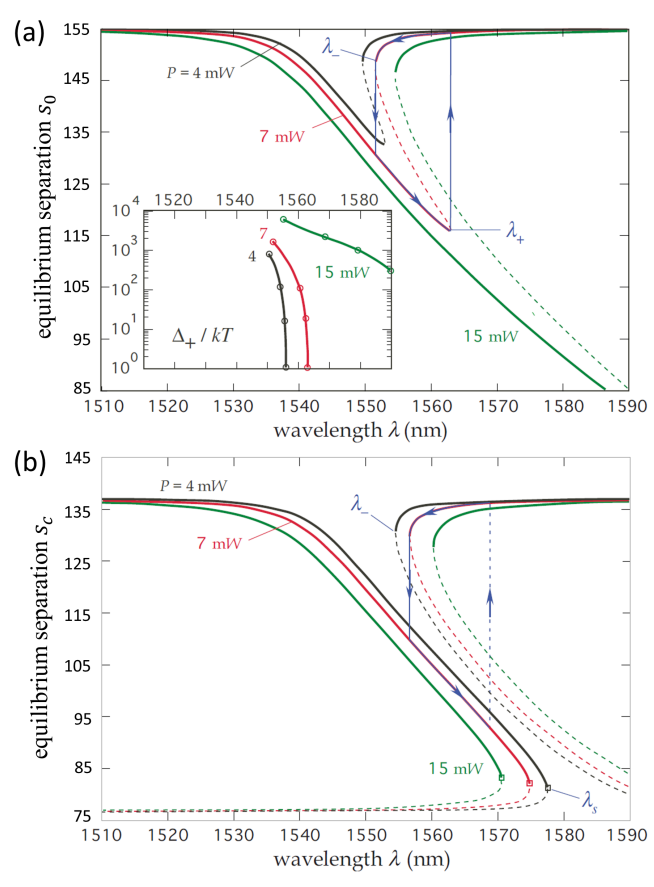

FIGURE 4.5: Equilibrium separation as a function of laser wavelength at $P = 7$ mW. A bistable region exists between λ_+ and λ_-. The arrows in this region indicate the hysteretic path traveled by the membrane as the laser is swept back and forth across the resonance. (From [39])

equilibrium caused by the Casimir force. Hysteresis may still appear in this configuration under the right conditions, however. If the membrane has enough kinetic energy to overcome the potential barrier (see analysis in Chapter 2.2.5), probabilistic transitions can occur between the two stable equilibria, roughly following the path denoted by the arrows in the figure.

4.2.2 Dynamics

Beyond studying the location of the stable mechanical equilibria, we can also discuss the effects of the Casimir force on the mechanical dynamics. A damped, driven harmonic oscillator feeling a strong Casimir force can me modeled as follows:

$$m\frac{d^2x(t)}{dt^2} + m\frac{\Gamma}{2}\frac{dx(t)}{dt} + m\Omega_0^2 x(t) = F_d + F_c \tag{4.8}$$

Where F_d is the harmonic driving force, and F_c is the Casimir force, m is the oscillator mass and $x(t)$ is the motion of the oscillator as a function of time. The Casimir force is highly nonlinear, so for small amplitudes x_0 of mechanical oscillation, we can Taylor expand $F_c(s-x_0)$ around s such that $F_c \approx F_c(s)+F_c'(s)x(t)+F_c''(s)x(t)^2/2+F_c'''(s)x(t)^3/6$. From here we can regroup the terms and rewrite Eq. 4.8 as

$$\frac{d^2x(t)}{dt^2} + \frac{\Gamma}{2}\frac{dx(t)}{dt} + (\Omega_0^2 - F_c'(s))x(t) = F_d + F_c(s) + \frac{F_c''(s)}{2}x(t)^2 + \frac{F_c'''(s)}{6}x(t)^3 \tag{4.9}$$

where we see that the zeroeth order contribution of the Casimir force will change the initial separation s_0, and the first order contribution will modify the mechanical resonance frequency $\Omega_0' = \sqrt{\Omega_0 - F_c'(s)}$. Beyond this, Eq. 4.9 can be solved [104], resulting in the following expression:

$$A^2\left[\left(\omega_i - \left[\Omega_0' + \kappa A^2\right]\right) + \frac{\Gamma}{2}\right] = \left(\frac{F_d}{m}\right)^2 \frac{1}{4\Omega_0'} \tag{4.10}$$

where A is the oscillation amplitude and the nonlinear contributions are expressed as

$$\kappa = -\frac{F_c'''(s)}{16\Omega_0'} + \frac{5F_c''(s)}{24\Omega_0'^3}. \tag{4.11}$$

Eq. 4.10 relates the oscillation amplitude A to the driving frequency ω_i, and reveals hysteresis and bistability introduced by a large κ. If we use parameters which represent

the device explored in Chapter 2, we can see how we expect the Casimir force to affect device dynamics as the membrane-substrate separation decreases. The results, plotted in Fig. 4.6, were generated assuming Ω_0 =180 kHz, a Casimir force between two 31×31 μm silicon membranes, and a driving force capable of generating oscillation amplitudes of a few nanometers. (These oscillation amplitudes are attainable with a few milliwatts of power, according to the data presented earlier.) Most significantly, Ω_m is highly sensitive to the membrane substrate separation, particularly at membrane-substrate separations near and below 100 nm. At these separations, a 1 nm change in s corresponds to more than a 1 kHz change in Ω_0', making these devices incredibly mechanically sensitive to s. Along with the mechanical frequency, the mechanical stiffness decreases as a function of membrane substrate separation, leading to larger oscillation amplitudes as the Casimir force grows. Additionally, strong hysteresis makes operation of a device at a fixed value of s strongly sensitive around the bistable transitions.

4.2.3 Preliminary Experiments

Chan, Capasso, and collaborators [56, 57] first investigated the effects of the Casimir force on a mechanical element in a similar system, consisting of a sphere suspended a short distance above a torsional oscillator, and demonstrated the potential power of such a system as a nonlinear switch. Their geometry required an AFM cantilever suspended above a MEMS resonator - an impractical geometry from potential applications due to the necessity of bulky external hardware. The geometry presented in Chapter 2 is uniquely suited for these sorts of Casimir experiments. The geometry, which consists of two parallel silicon plates separated by a lithographically defined small distance, is fabricated from a single chip and requires no external apparatus like the AFM in the previous experiments. We propose that the Casimir force can be measured by optically

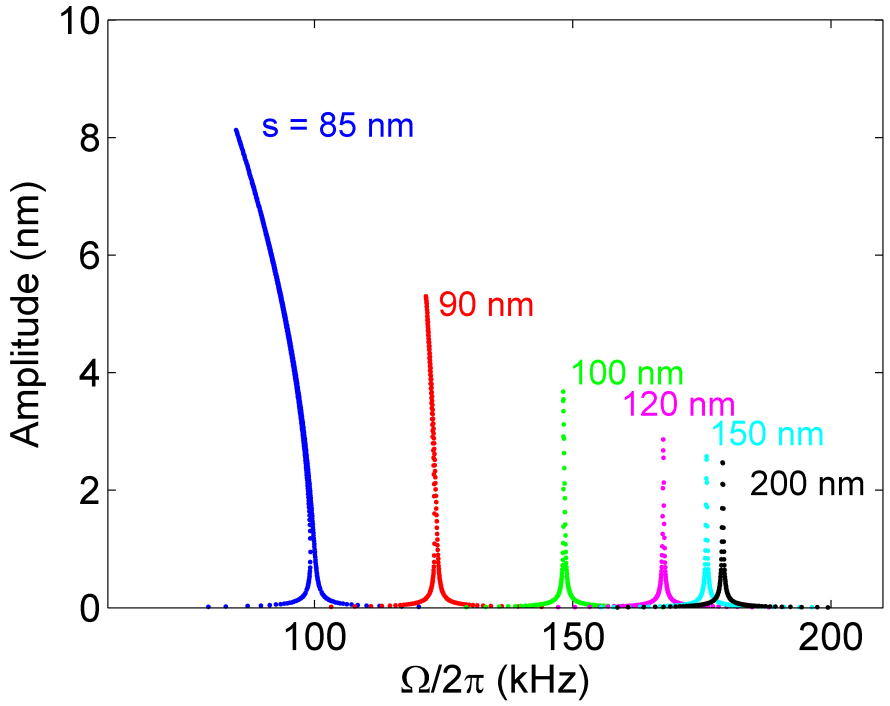

FIGURE 4.6: The mechanical response to a system experiencing a strong Casimir effect. The Casimir force perturbs the mechanical motion of the device, causing a decrease in mechanical frequency as the membrane-substrate separation decreases. Mechanical hysteresis and bistability occur for separations below 120 nm (blue, red and green lines), where the device behavior becomes increasingly nonlinear.

controlling the equilibrium separation in real time by illuminating the membrane with normally incident light at a tunable wavelength λ, where the resonant force allows one to dynamically determine the Casimir-induced threshold for stiction.

The previous section discussed the dependence of the mechanical resonance frequency on the membrane-substrate separation (Fig. 4.7(a)). We previously demonstrated the sensitivity, measured as g_{OM}, of the optical resonance location to the membrane-substrate separation (Fig. 4.7(b)).The combination of these two give us in-situ determination of the separation and of the strength of the Casimir force.

Figure 4.8 plots the two in-situ measurable quantities - optical resonance wavelength, and mechanical resonance frequency, against one another for various values of s. The colors of the circles correspond to the colors of the curves in Fig. 4.6, while the yellow triangles

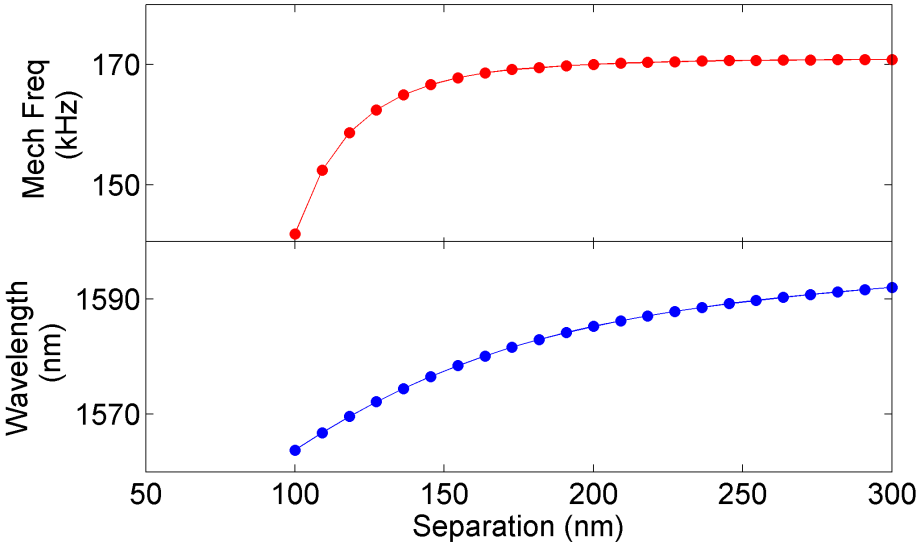

FIGURE 4.7: The mechanical resonance frequency (above) and optical resonance wavelength (below) as a function of separation. The mechanical resonance frequency is perturbed due to the Casimir force, while the optical resonance wavelength shifts due to the g_{OM} of the mode.

each correspond to measurements of individual devices. Over the range of separations achieved thus far, our experimental results match quite well with theoretical predictions: the mechanical frequency of the membrane decreases with membrane-substrate separation. Simulations of the mechanical modes with COMSOL Multiphysics taking into account the differences in the etch-hole patterns of the support structure indicate that design differences cannot account for this trend, nor can potential contributes from deformation of the membrane due to large deflections [140], which would result in a change in the stiffness of the membrane with respect to the absolute value of the membrane deflection. We cannot, however, rule out electrostatics, which, like the Casimir effect, results in an attractive force which gets stronger at smaller separations.

Further experiments will be needed to separate the Casimir effect from electrostatics. The Casimir force follows a s^{-4} power law, while the electrostatic force follows a s^{-2} power law, making then distinguishable from one another if data at smaller separations can be collected. Initial attempts to fabricate devices with separations as small as 100 nm

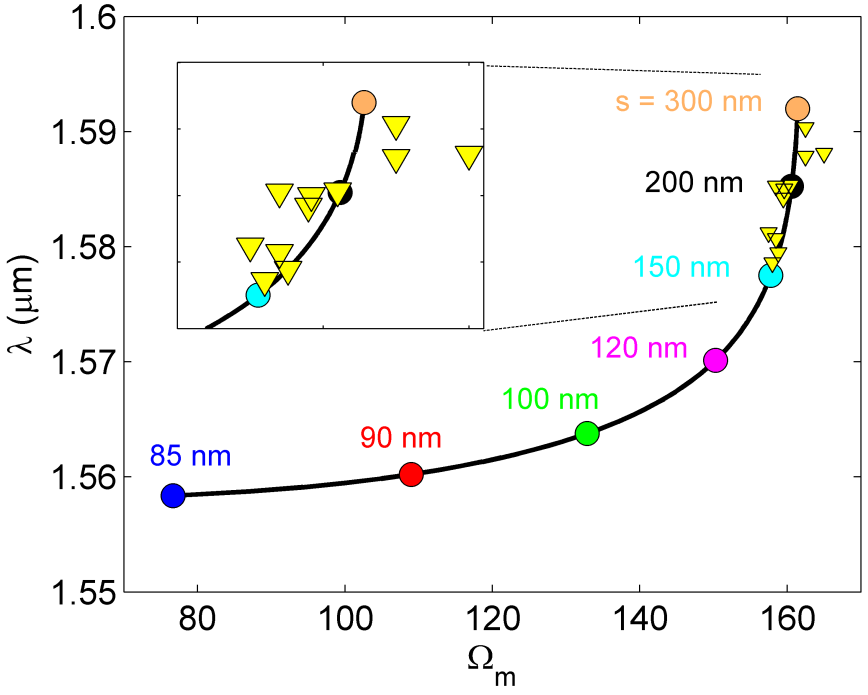

FIGURE 4.8: The optical resonance wavelength as a function of mechanical frequency due to displacement by the Casimir force for separations between s = 85 and s = 300 nm (black line). Devices with membrane-substrate separation below 150 nm are strongly affected by the Casimir effect. Current fabricated devices (yellow triangles) with separations between 300 nm and 150 nm follow the $\lambda - \Omega_m$ curve well, though the trend may include effects other than Casimir.

have experienced full or partial collapse, as methods of controlling membrane tilt remain unoptimized. However, the potential remains for the creation of a nonlinear Casimir-optomechanical oscillator, which could take advantage of both optical and mechanical hysteresis to become a highly sensitive gas-phase mass, force, and refractive-index sensor. Additional applications lie in the field of optofluidics. By replacing the thick, underlying buried oxide layer with a flow cell, biological or chemical binding events at the silicon-water interface would modify the optical resonance frequency, and, in turn, the mechanical resonance frequency, elegantly combining a free-space or vacuum mechanical element with liquid-phase refractive index sensing.

Bibliography

[1] P. Lebedew. Testings on the compressive force of light. *Annalen Der Physik*, 6 (11):433–458, 1901.

[2] E. F. Nichols and G. F. Hull. The pressure due to radiation (second paper). *Physical Review*, 17(1):26–50, 1903.

[3] R. L. Garwin. Solar sailing - a practical method of propulsion within the solar system. *Jet Propulsion*, 28(3):188–190, 1958.

[4] A. Ashkin, J. M. Dziedzic, J. E. Bjorkholm, and S. Chu. Observation of a single-beam gradient force optical trap for dielectric particles. *Optics Letters*, 11(5): 288–290, 1986.

[5] D. G. Grier. A revolution in optical manipulation. *Nature*, 424(6950):810–816, 2003.

[6] C. Xiong, W. H. P. Pernice, M. Li, and H. X. Tang. High performance nanophotonic circuits based on partially buried horizontal slot waveguides. *Optics Express*, 18(20):20690–20698, 2010.

[7] John David Jackson. *Classical electrodynamics*. Wiley, New York, 3rd edition, 1999.

[8] Lukas Novotny and Bert Hecht. *Principles of nano-optics*. Cambridge University Press, Cambridge ; New York, 2006.

[9] M. L. Povinelli, M. Loncar, M. Ibanescu, E. J. Smythe, S. G. Johnson, F. Capasso, and J. D. Joannopoulos. Evanescent-wave bonding between optical waveguides. *Optics Letters*, 30(22):3042–3044, 2005.

[10] Matt Eichenfield, Christopher P. Michael, Raviv Perahia, and Oskar Painter. Actuation of micro-optomechanical systems via cavity-enhanced optical dipole forces. *Nature Photonics*, 1(7):416–422, 2007.

[11] M. Li, W. H. P. Pernice, C. Xiong, T. Baehr-Jones, M. Hochberg, and H. X. Tang. Harnessing optical forces in integrated photonic circuits. *Nature*, 456(7221):480–U28, 2008.

[12] F. Riboli, A. Recati, M. Antezza, and I. Carusotto. Radiation induced force between two planar waveguides. *European Physical Journal D*, 46(1):157–164, 2008.

[13] M. Li, W. H. P. Pernice, and H. X. Tang. Reactive cavity optical force on microdisk-coupled nanomechanical beam waveguides. *Physical Review Letters*, 103(22), 2009.

[14] M. Eichenfield, J. Chan, R. M. Camacho, K. J. Vahala, and O. Painter. Optomechanical crystals. *Nature*, 462(7269):78–82, 2009.

[15] P. B. Deotare, M. W. McCutcheon, I. W. Frank, M. Khan, and M. Loncar. Coupled photonic crystal nanobeam cavities. *Applied Physics Letters*, 95(3), 2009.

[16] J. Rosenberg, Q. Lin, and O. Painter. Static and dynamic wavelength routing via the gradient optical force. *Nature Photonics*, 3(8):478–483, 2009.

[17] G. S. Wiederhecker, L. Chen, A. Gondarenko, and M. Lipson. Controlling photonic structures using optical forces. *Nature*, 462(7273):633–U103, 2009.

[18] X. D. Yang, Y. M. Liu, R. F. Oulton, X. B. Yin, and X. A. Zhang. Optical forces in hybrid plasmonic waveguides. *Nano Letters*, 11(2):321–328, 2011.

[19] J. N. Munday and F. Capasso. Precision measurement of the casimir-lifshitz force in a fluid. *Physical Review A*, 75(6), 2007.

[20] J. N. Munday, F. Capasso, V. A. Parsegian, and S. M. Bezrukov. Measurements of the casimir-lifshitz force in fluids: The effect of electrostatic forces and debye screening. *Physical Review A*, 78(3), 2008.

[21] J. N. Munday, F. Capasso, and V. A. Parsegian. Measured long-range repulsive casimir-lifshitz forces. *Nature*, 457(7226):170–173, 2009.

[22] N. V. Lavrik and P. G. Datskos. Femtogram mass detection using photothermally actuated nanomechanical resonators. *Applied Physics Letters*, 82(16):2697–2699, 2003.

[23] X. L. Feng, C. J. White, A. Hajimiri, and M. L. Roukes. A self-sustaining ultrahigh-frequency nanoelectromechanical oscillator. *Nature Nanotechnology*, 3 (6):342–346, 2008.

[24] B. R. Ilic, S. Krylov, M. Kondratovich, and H. G. Craighead. Optically actuated nanoelectromechanical oscillators. *Ieee Journal of Selected Topics in Quantum Electronics*, 13(2):392–399, 2007.

[25] Y. T. Yang, C. Callegari, X. L. Feng, K. L. Ekinci, and M. L. Roukes. Zeptogram-scale nanomechanical mass sensing. *Nano Letters*, 6(4):583–586, 2006.

[26] M. Eichenfield, R. Camacho, J. Chan, K. J. Vahala, and O. Painter. A picogram- and nanometre-scale photonic-crystal optomechanical cavity. *Nature*, 459(7246): 550–U79, 2009.

[27] C. H. Metzger and K. Karrai. Cavity cooling of a microlever. *Nature*, 432(7020): 1002–1005, 2004.

[28] T. J. Kippenberg and K. J. Vahala. Cavity opto-mechanics. *Optics Express*, 15 (25):17172–17205, 2007.

[29] A. Schliesser, P. Del'Haye, N. Nooshi, K. J. Vahala, and T. J. Kippenberg. Radiation pressure cooling of a micromechanical oscillator using dynamical backaction. *Physical Review Letters*, 97(24), 2006.

[30] J. Chan, T. P. M. Alegre, A. H. Safavi-Naeini, J. T. Hill, A. Krause, S. Groblacher, M. Aspelmeyer, and O. Painter. Laser cooling of a nanomechanical oscillator into its quantum ground state. *Nature*, 478(7367):89–92, 2011.

[31] A. G. Krause, M. Winger, T. D. Blasius, Q. Lin, and O. Painter. A high-resolution microchip optomechanical accelerometer. *Nature Photonics*, 6(11):768–772, 2012.

[32] O. Arcizet, P. F. Cohadon, T. Briant, M. Pinard, and A. Heidmann. Radiation-pressure cooling and optomechanical instability of a micromirror. *Nature*, 444 (7115):71–74, 2006.

[33] M. W. Pruessner, T. H. Stievater, J. B. Khurgin, and W. S. Rabinovich. Integrated waveguide-dbr microcavity opto-mechanical system. *Optics Express*, 19(22):21904–21918, 2011.

[34] H. Fu, C. D. Liu, Y. Liu, J. R. Chu, and G. Y. Cao. Selective photothermal self-excitation of mechanical modes of a micro-cantilever for force microscopy. *Applied Physics Letters*, 99(17), 2011.

[35] Q. Lin, J. Rosenberg, X. S. Jiang, K. J. Vahala, and O. Painter. Mechanical oscillation and cooling actuated by the optical gradient force. *Physical Review Letters*, 103(10), 2009.

[36] G. Anetsberger, O. Arcizet, Q. P. Unterreithmeier, R. Riviere, A. Schliesser, E. M. Weig, J. P. Kotthaus, and T. J. Kippenberg. Near-field cavity optomechanics with nanomechanical oscillators. *Nature Physics*, 5(12):909–914, 2009.

[37] M. L. Povinelli, S. G. Johnson, M. Loncar, M. Ibanescu, E. J. Smythe, F. Capasso, and J. D. Joannopoulos. High-q enhancement of attractive and repulsive optical forces between coupled whispering-gallery-mode resonators. *Optics Express*, 13 (20):8286–8295, 2005.

[38] M. Li, W. H. P. Pernice, and H. X. Tang. Tunable bipolar optical interactions between guided lightwaves. *Nature Photonics*, 3(8):464–468, 2009.

[39] A. W. Rodriguez, A. P. McCauley, P. C. Hui, D. Woolf, E. Iwase, F. Capasso, M. Loncar, and S. G. Johnson. Bonding, antibonding and tunable optical forces in asymmetric membranes. *Optics Express*, 19(3):2225–2241, 2011.

[40] J. Lee, B. Zhen, S. L. Chua, W. J. Qiu, J. D. Joannopoulos, M. Soljacic, and O. Shapira. Observation and differentiation of unique high-q optical resonances near zero wave vector in macroscopic photonic crystal slabs. *Physical Review Letters*, 109(6), 2012.

[41] E. Iwase, P. C. Hui, D. Woolf, A. W. Rodriguez, S. G. Johnson, F. Capasso, and M. Loncar. Control of buckling in large micromembranes using engineered support structures. *Journal of Micromechanics and Microengineering*, 22(6), 2012.

[42] D. Blocher, A. T. Zehnder, R. H. Rand, and S. Mukerji. Anchor deformations drive limit cycle oscillations in interferometrically transduced mems beams. *Finite Elements in Analysis and Design*, 49(1):52–57, 2012.

[43] P. B. Deotare, I. Bulu, I. W. Frank, Q. Quan, Y. Zhang, B. R. Ilic, and M. Loncar. All optical reconfiguration of optomechanical filters. *Nature Communications*, 2012.

[44] Y. Y. Gong, A. Rundquist, A. Majumdar, and J. Vuckovic. Low power resonant optical excitation of an optomechanical cavity. *Optics Express*, 19(2):1429–1440, 2011.

[45] T. J. Johnson, M. Borselli, and O. Painter. Self-induced optical modulation of the transmission through a high-q silicon microdisk resonator. *Optics Express*, 14(2): 817–831, 2006.

[46] S. H. Fan and J. D. Joannopoulos. Analysis of guided resonances in photonic crystal slabs. *Physical Review B*, 65(23), 2002.

[47] Hermann A. Haus. *Waves and fields in optoelectronics*. Prentice-Hall series in solid state physical electronics. Prentice-Hall, Englewood Cliffs, NJ, 1984.

[48] D. Rugar, H. J. Mamin, and P. Guethner. Improved fiber-optic interferometer for atomic force microscopy. *Applied Physics Letters*, 55(25):2588–2590, 1989.

[49] K. J. Vahala. Back-action limit of linewidth in an optomechanical oscillator. *Physical Review A*, 78(2), 2008.

[50] J. L. Yang, T. Ono, and M. Esashi. Surface effects and high quality factors in ultrathin single-crystal silicon cantilevers. *Applied Physics Letters*, 77(23):3860–3862, 2000.

[51] M. Borselli, T. J. Johnson, and O. Painter. Measuring the role of surface chemistry in silicon microphotonics. *Applied Physics Letters*, 88(13), 2006.

[52] J. O. Grepstad, P. Kaspar, O. Solgaard, I. R. Johansen, and A. S. Sudbo. Photonic-crystal membranes for optical detection of single nano-particles, designed for biosensor application. *Optics Express*, 20(7):7954–7965, 2012.

[53] M. El Beheiry, V. Liu, S. H. Fan, and O. Levi. Sensitivity enhancement in photonic crystal slab biosensors. *Optics Express*, 18(22):22702–22714, 2010.

[54] P. S. Waggoner and H. G. Craighead. Micro- and nanomechanical sensors for environmental, chemical, and biological detection. *Lab on a Chip*, 7(10):1238–1255, 2007.

[55] J. L. Arlett, E. B. Myers, and M. L. Roukes. Comparative advantages of mechanical biosensors. *Nature Nanotechnology*, 6(4):203–215, 2011.

[56] H. B. Chan, V. A. Aksyuk, R. N. Kleiman, D. J. Bishop, and F. Capasso. Nonlinear micromechanical casimir oscillator. *Physical Review Letters*, 87(21), 2001.

[57] H. B. Chan, V. A. Aksyuk, R. N. Kleiman, D. J. Bishop, and F. Capasso. Quantum mechanical actuation of microelectromechanical systems by the casimir force (vol 291, pg 1941, 2001). *Science*, 293(5530):607–607, 2001.

[58] A. W. Rodriguez, F. Capasso, and S. G. Johnson. The casimir effect in microstructured geometries. *Nature Photonics*, 5(4):211–221, 2011.

[59] S. J. Rahi, A. W. Rodriguez, T. Emig, R. L. Jaffe, S. G. Johnson, and M. Kardar. Nonmonotonic effects of parallel sidewalls on casimir forces between cylinders. *Physical Review A*, 77(3), 2008.

[60] M. Hossein-Zadeh and K. J. Vahala. Observation of injection locking in an optomechanical rf oscillator. *Applied Physics Letters*, 93(19), 2008.

[61] M. Davanco, J. Chan, A. H. Safavi-Naeini, O. Painter, and K. Srinivasan. Slot-mode-coupled optomechanical crystals. *Optics Express*, 20(22):24394–24410, 2012.

[62] Zhipeng Li, Mikael Kall, and Hongxing Xu. Optical forces on interacting plasmonic nanoparticles in a focused gaussian beam. *Physical Review B*, 77(8), 2008.

[63] O. Kilic, M. Digonnet, G. Kino, and O. Solgaard. Controlling uncoupled resonances in photonic crystals through breaking the mirror symmetry. *Optics Express*, 16 (17):13090–13103, 2008.

[64] S. L. Chua, Y. D. Chong, A. D. Stone, M. Soljacic, and J. Bravo-Abad. Low-threshold lasing action in photonic crystal slabs enabled by fano resonances. *Optics Express*, 19(2):1539–1562, 2011.

[65] B. S. Sheard, M. B. Gray, C. M. Mow-Lowry, D. E. McClelland, and S. E. Whitcomb. Observation and characterization of an optical spring. *Physical Review A*, 69(5), 2004.

[66] T. J. Kippenberg and K. J. Vahala. Cavity optomechanics: Back-action at the mesoscale. *Science*, 321(5893):1172–1176, 2008.

[67] K. Srinivasan and O. Painter. Momentum space design of high-q photonic crystal optical cavities. *Optics Express*, 10(15):670–684, 2002.

[68] Mani Hossein-Zadeh and Kerry J. Vahala. Observation of optical spring effect in a microtoroidal optomechanical resonator. *Optics Letters*, 32(12):1611–1613, 2007.

[69] V. G. Veselago. Electrodynamics of substances with simultaneously negative values of sigma and mu. *Soviet Physics Uspekhi-Ussr*, 10(4):509–&, 1968.

[70] M. Scalora, G. D'Aguanno, N. Mattiucci, M. J. Bloemer, M. Centini, C. Sibilia, and J. W. Haus. Radiation pressure of light pulses and conservation of linear momentum in dispersive media. *Physical Review E*, 73(5), 2006.

[71] A. D. Boardman and K. Marinov. Electromagnetic energy in a dispersive metamaterial. *Physical Review B*, 73(16), 2006.

[72] M. I. Antonoyiannakis and J. B. Pendry. Electromagnetic forces in photonic crystals. *Physical Review B*, 60(4):2363–2374, 1999.

[73] M. Mansuripur. Radiation pressure and the linear momentum of light in dispersive dielectric media. *Optics Express*, 13(6):2245–2250, 2005.

[74] Stephen M. Barnett and Rodney Loudon. On the electromagnetic force on a dielectric medium. *Journal of Physics B-Atomic Molecular and Optical Physics*, 39(15):S671–S684, 2006.

[75] M. L. Povinelli, M. Ibanescu, S. G. Johnson, and J. D. Joannopoulos. Slow-light enhancement of radiation pressure in an omnidirectional-reflector waveguide. *Applied Physics Letters*, 85(9):1466–1468, 2004.

[76] B. M. Han, S. Chang, and S. S. Lee. Enhancement of the evanescent field pressure on a dielectric film by coupling with surface plasmons. *Journal of the Korean Physical Society*, 35(3):180–185, 1999.

[77] Fang Liu, Yi Rao, Yidong Huang, Wei Zhang, and Jiangde Peng. Coupling between long range surface plasmon polariton mode and dielectric waveguide mode. *Applied Physics Letters*, 90(14), 2007.

[78] H. S. Won, K. C. Kim, S. H. Song, C. H. Oh, P. S. Kim, S. Park, and S. I. Kim. Vertical coupling of long-range surface plasmon polaritons. *Applied Physics Letters*, 88(1), 2006.

[79] J. Homola, S. S. Yee, and G. Gauglitz. Surface plasmon resonance sensors: review. *Sensors and Actuators B-Chemical*, 54(1-2):3–15, 1999.

[80] D. Sarid. Long-range surface-plasma waves on very thin metal-films. *Physical Review Letters*, 47(26):1927–1930, 1981.

[81] Pierre Berini, Robert Charbonneau, and Nancy Lahoud. Long-range surface plasmons on ultrathin membranes. *Nano Letters*, 7(5):1376–1380, 2007.

[82] T. Nikolajsen, K. Leosson, I. Salakhutdinov, and S. I. Bozhevolnyi. Polymer-based surface-plasmon-polariton stripe waveguides at telecommunication wavelengths. *Applied Physics Letters*, 82(5):668–670, 2003.

[83] P. Nordlander and E. Prodan. Plasmon hybridization in nanoparticles near metallic surfaces. *Nano Letters*, 4(11):2209–2213, 2004.

[84] E. Prodan and P. Nordlander. Plasmon hybridization in spherical nanoparticles. *Journal of Chemical Physics*, 120(11):5444–5454, 2004.

[85] T. W. Ebbesen, H. J. Lezec, H. F. Ghaemi, T. Thio, and P. A. Wolff. Extraordinary optical transmission through sub-wavelength hole arrays. *Nature*, 391(6668):667–669, 1998.

[86] Hideki T. Miyazaki and Yoichi Kurokawa. Controlled plasmon resonance in closed metal/insulator/metal nanocavities. *Applied Physics Letters*, 89(21), 2006.

[87] J. A. Dionne, L. A. Sweatlock, H. A. Atwater, and A. Polman. Plasmon slot waveguides: Towards chip-scale propagation with subwavelength-scale localization. *Physical Review B*, 73(3), 2006.

[88] Yoichi Kurokawa and Hideki T. Miyazaki. Metal-insulator-metal plasmon nanocavities: Analysis of optical properties. *Physical Review B*, 75(3), 2007.

[89] H. T. Miyazaki and Y. Kurokawa. Squeezing visible light waves into a 3-nm-thick and 55-nm-long plasmon cavity. *Physical Review Letters*, 96(9), 2006.

[90] C. E. Talley, J. B. Jackson, C. Oubre, N. K. Grady, C. W. Hollars, S. M. Lane, T. R. Huser, P. Nordlander, and N. J. Halas. Surface-enhanced raman scattering from individual au nanoparticles and nanoparticle dimer substrates. *Nano Letters*, 5(8):1569–1574, 2005.

[91] Ertugrul Cubukcu, Nanfang Yu, Elizabeth J. Smythe, Laurent Diehl, Kenneth B. Crozier, and Federico Capasso. Plasmonic laser antennas and related devices. *Ieee Journal of Selected Topics in Quantum Electronics*, 14(6):1448–1461, 2008.

[92] M. Nieto-Vesperinas, P. C. Chaumet, and A. Rahmani. Near-field photonic forces. *Philosophical Transactions of the Royal Society of London Series a-Mathematical Physical and Engineering Sciences*, 362(1817):719–737, 2004.

[93] G. Volpe, R. Quidant, G. Badenes, and D. Petrov. Surface plasmon radiation forces. *Physical Review Letters*, 96(23), 2006.

[94] Maurizio Righini, Giovanni Volpe, Christian Girard, Dmitri Petrov, and Romain Quidant. Surface plasmon optical tweezers: Tunable optical manipulation in the femtonewton range. *Physical Review Letters*, 100(18), 2008.

[95] Y. G. Song, B. M. Han, and S. Chang. Force of surface plasmon-coupled evanescent fields on mie particles. *Optics Communications*, 198(1-3):7–19, 2001.

[96] F. J. Garcia de Abajo, T. Brixner, and W. Pfeiffer. Nanoscale force manipulation in the vicinity of a metal nanostructure. *Journal of Physics B-Atomic Molecular and Optical Physics*, 40(11):S249–S258, 2007.

[97] J. R. Arias-Gonzalez and M. Nieto-Vesperinas. Optical forces on small particles: attractive and repulsive nature and plasmon-resonance conditions. *Journal of the Optical Society of America a-Optics Image Science and Vision*, 20(7):1201–1209, 2003.

[98] R. Quidant, S. Zelenina, and M. Nieto-Vesperinas. Optical manipulation of plasmonic nanoparticles. *Applied Physics a-Materials Science & Processing*, 89(2): 233–239, 2007.

[99] Vassilios Yannopapas. Optical forces near a plasmonic nanostructure. *Physical Review B*, 78(4), 2008.

[100] Jack Ng, Ross Tang, and C. T. Chan. Electrodynamics study of plasmonic bonding and antibonding forces in a bisphere. *Physical Review B*, 77(19), 2008.

[101] Edward D. Palik. *Handbook of Optical Constants of Solids*. Academic Press, San Diego, 1997.

[102] I. Pirozhenko, A. Lambrecht, and V. B. Svetovoy. Sample dependence of the casimir force. *New Journal of Physics*, 8, 2006.

[103] M. Mansuripur and A. R. Zakharian. Maxwell's macroscopic equations, the energy-momentum postulates, and the lorentz law of force. *Physical Review E*, 79(2), 2009.

[104] L. D. Landau and E. M. Lifshits. *Mechanics*. Course of theoretical physics. Pergamon Press, Oxford ; New York, 3d edition, 1976.

[105] V. L. Ginzburg. *Applications of electrodynamics in theoretical physics and astrophysics*. Gordon and Breach Science Publishers, New York, 2nd rev. english edition, 1989.

[106] S. Lal, S. Link, and N. J. Halas. Nano-optics from sensing to waveguiding. *Nature Photonics*, 1(11):641–648, 2007.

[107] S. A. Maier and H. A. Atwater. Plasmonics: Localization and guiding of electromagnetic energy in metal/dielectric structures. *Journal of Applied Physics*, 98(1), 2005.

[108] H. J. Lezec, J. A. Dionne, and H. A. Atwater. Negative refraction at visible frequencies. *Science*, 316(5823):430–432, 2007.

[109] J. A. Dionne, E. Verhagen, A. Polman, and H. A. Atwater. Are negative index materials achievable with surface plasmon waveguides? a case study of three plasmonic geometries. *Optics Express*, 16(23):19001–19017, 2008.

[110] W. S. Cai, W. Shin, S. H. Fan, and M. L. Brongersma. Elements for plasmonic nanocircuits with three-dimensional slot waveguides. *Advanced Materials*, 22(45): 5120–5124, 2010.

[111] K. F. MacDonald, Z. L. Samson, M. I. Stockman, and N. I. Zheludev. Ultrafast active plasmonics. *Nature Photonics*, 3(1):55–58, 2009.

[112] D. Woolf, M. Loncar, and F. Capasso. The forces from coupled surface plasmon polaritons in planar waveguides. *Optics Express*, 17(22):19996–20011, 2009.

[113] W. A. Murray and W. L. Barnes. Plasmonic materials. *Advanced Materials*, 19 (22):3771–3782, 2007.

[114] C. Rhodes, S. Franzen, J. P. Maria, M. Losego, D. N. Leonard, B. Laughlin, G. Duscher, and S. Weibel. Surface plasmon resonance in conducting metal oxides. *Journal of Applied Physics*, 100(5), 2006.

[115] J. B. Pendry, L. Martin-Moreno, and F. J. Garcia-Vidal. Mimicking surface plasmons with structured surfaces. *Science*, 305(5685):847–848, 2004.

[116] F. J. Garcia-Vidal, L. Martin-Moreno, and J. B. Pendry. Surfaces with holes in them: new plasmonic metamaterials. *Journal of Optics a-Pure and Applied Optics*, 7(2):S97–S101, 2005.

[117] B. W. Wang, Y. Jin, and S. L. He. Design of subwavelength corrugated metal waveguides for slow waves at terahertz frequencies. *Applied Optics*, 47(21):3694–3700, 2008.

[118] N. F. Yu, Q. J. Wang, M. A. Kats, J. A. Fan, S. P. Khanna, L. H. Li, A. G. Davies, E. H. Linfield, and F. Capasso. Designer spoof surface plasmon structures collimate terahertz laser beams. *Nature Materials*, 9(9):730–735, 2010.

[119] J. Zhang, L. K. Cai, W. L. Bai, Y. Xu, and G. F. Song. Slow light at terahertz frequencies in surface plasmon polariton assisted grating waveguide. *Journal of Applied Physics*, 106(10), 2009.

[120] K. Song and P. Mazumder. Active terahertz spoof surface plasmon polariton switch comprising the perfect conductor metamaterial. *Ieee Transactions on Electron Devices*, 56(11):2792–2799, 2009.

[121] M. A. Kats, D. Woolf, R. Blanchard, N. F. Yu, and F. Capasso. Spoof plasmon analogue of metal-insulator-metal waveguides. *Optics Express*, 19(16):14860–14870, 2011.

[122] A. Rusina, M. Durach, and M. I. Stockman. Theory of spoof plasmons in real metals. *Applied Physics a-Materials Science & Processing*, 100(2):375–378, 2010.

[123] X. R. Huang, R. W. Peng, and R. H. Fan. Making metals transparent for white light by spoof surface plasmons. *Physical Review Letters*, 105(24), 2010.

[124] Umran S. Inan and Aziz S. Inan. *Electromagnetic waves*. Prentice Hall, Upper Saddle River, N.J., 2000.

[125] A. Huber, N. Ocelic, D. Kazantsev, and R. Hillenbrand. Near-field imaging of mid-infrared surface phonon polariton propagation. *Applied Physics Letters*, 87 (8), 2005.

[126] M. J. Lockyear, A. P. Hibbins, and J. R. Sambles. Microwave surface-plasmon-like modes on thin metamaterials. *Physical Review Letters*, 102(7), 2009.

[127] N. F. Yu, P. Genevet, M. A. Kats, F. Aieta, J. P. Tetienne, F. Capasso, and Z. Gaburro. Light propagation with phase discontinuities: Generalized laws of reflection and refraction. *Science*, 334(6054):333–337, 2011.

[128] K. Wang, E. Schonbrun, P. Steinvurzel, and K. B. Crozier. Trapping and rotating nanoparticles using a plasmonic nano-tweezer with an integrated heat sink. *Nature Communications*, 2, 2011.

[129] K. Wang, E. Schonbrun, and K. B. Crozier. Propulsion of gold nanoparticles with surface plasmon polaritons: Evidence of enhanced optical force from near-field coupling between gold particle and gold film. *Nano Letters*, 9(7):2623–2629, 2009.

[130] K. T. Gahagan and G. A. Swartzlander. Optical vortex trapping of particles. *Optics Letters*, 21(11):827–829, 1996.

[131] S. Chang, J. T. Kim, J. H. Jo, and S. S. Lee. Optical force on a sphere caused by the evanescent field of a gaussian beam; effects of multiple scattering. *Optics Communications*, 139(4-6):252–261, 1997.

[132] R. L. Rich and D. G. Myszka. Advances in surface plasmon resonance biosensor analysis. *Current Opinion in Biotechnology*, 11(1):54–61, 2000.

[133] K. A. Peterlinz, R. M. Georgiadis, T. M. Herne, and M. J. Tarlov. Observation of hybridization and dehybridization of thiol-tethered dna using two-color surface plasmon resonance spectroscopy. *Journal of the American Chemical Society*, 119 (14):3401–3402, 1997.

[134] K. A. Willets and R. P. Van Duyne. Localized surface plasmon resonance spectroscopy and sensing. *Annual Review of Physical Chemistry*, 58:267–297, 2007.

[135] V. Adrian Parsegian. *Van der Waals forces : a handbook for biologists, chemists, engineers, and physicists.* Cambridge University Press, New York, 2006.

[136] H. B. G. Casimir and D. Polder. The influence of retardation on the london-vanderwaals forces. *Physical Review*, 73(4):360–372, 1948.

[137] E. M. Lifshitz. The theory of molecular attractive forces between solids. *Soviet Physics Jetp-Ussr*, 2(1):73–83, 1956.

[138] I. E. Dzyaloshinskii, E. M. Lifshitz, and L. P. Pitaevskii. The general theory of vanderwaals forces. *Advances in Physics*, 10(38):165–209.

[139] E. Buks and M. L. Roukes. Stiction, adhesion energy, and the casimir effect in micromechanical systems. *Physical Review B*, 63(3):art. no.–033402, 2001.

[140] Andrew N. Cleland. *Foundations of nanomechanics : from solid-state theory to device applications*. Springer, Berlin ; New York, 2003.